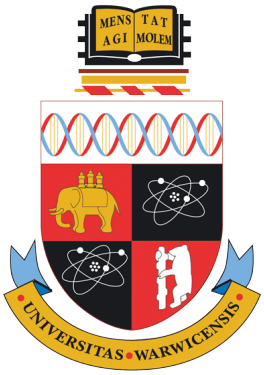

Development and application of path integral methods to study nuclear quantum effects in aqueous systems.

Samuel James Buxton

Thesis submitted to the University of Warwick towards award of the degree of Doctor of Philosophy.

Department of Chemistry

July 2019

Contents

List of Tables

List of Figures

Abbreviations

CMD	Centroid Molecular Dynamics	5
DHFR	*Escherichia coli* dihydrofolate reductase	59
GPR	Gaussian Process Regression	70
KRR	Kernel Ridge Regression	63
LJ	Lennard-Jones	25
MC	Monte Carlo	22
MD	Molecular Dynamics	3
NQE	Nuclear Quantum Effect	2
PBC	Periodic Boundary Conditions	33
PES	Potential Energy Surface	2
PI	Path Integral	3
PIMC	Path Integral Monte Carlo	48
PIMD	Path Integral Molecular Dynamics	5
RDF	Radial Distribution Function	77
RPC	Ring-Polymer Contraction	64
RPI	Ring Polymer Interpolation	63
RPMD	Ring Polymer Molecular Dynamics	8
ZPE	Zero-Point Energy	8

Acknowledgements

Firstly I would like to thank Scott Habershon for his support over the last four years and for giving me the opportunity to work as part of his research group on a variety of interesting and engaging projects. He has been a fantastic mentor and has always been available to offer assistance and advice when needed. Overall he has been responsible for my continued growth and development as a scientist and has ultimately inspired me to pursue my own career in teaching.

I would like to thank the University of Warwick and the Centre for Scientific Computing for the abundance of resources that have been made available to me during my studies. I would also like to thank the EPSRC research council for funding my project and allowing me to carry out my research.

I have been very lucky during my time at Warwick to have had such a wide range of colleagues and friends, including some who I had previously worked with in Birmingham during my undergraduate years. Each and every one of these people have made my experience at Warwick unforgettable and enriched it in one form or another. In no particular order I would like to extend my deepest thanks to Lewis, Max, Gareth, Christopher, Jasmine, Kirsten and Harry. I would like to give a special mention to Iakov, who first sparked my interest in computational chemistry during my masters degree.

There are a number of people who while not at Warwick have continued to be my friends and a key part of my life despite in many cases living far away. Thanks to Craig, Giles, Phil, Daniel and Isabelle.

To Mom and Dad, Thank you for your constant support and encouragement. You have always been there for me and done everything in your power to help me through life and allow me to take any path I wanted. I would not be where I am today without you and words cannot describe how grateful I am or how much I love you both.

To Rachel, thanks for putting up with me for four years and buying me a house because I couldn't be bothered to get a real job!

Declaration

This thesis is submitted to the University of Warwick in support of my application for the degree of Doctor of Philosophy. It has been composed by myself and has not been submitted in any previous application for any degree. The work presented (including data generated and data analysis) was carried out entirely by myself.

Samuel James Buxton, July 2019

Parts of this thesis have been published by the author

- S. Buxton and S.Habershon, *J. Chem. Phys.,* 2017, **147**, 224107

Abstract

Nuclear quantum effects have been shown to play a large role in defining the properties of chemical systems. However including these in computational simulations for example using path integral methods is far more computationally expensive than a classical simulation where these effects are ignored. This is because the number of individual force calculations is greatly increased when using a path integral method. This means that for some systems and system sizes it is difficult to computationally evaluate fully quantum properties. To address this, methods have been developed that can accelerate this simulations with minimal loss of accuracy, however the most popular methods all suffer from drawbacks which limits their application to certain types of system. This work presents a novel method for increasing the speed of path integral simulations that employs Kernel-Ridge Regression to enable fewer individual force calculations during the simulation while maintaining accuracy. The main advantage of this method lies in its ability to be applied to any system of interest with no conditions or prior assumptions about the potential energy surface. Results for this method are very positive when applied to two systems where quantum effects are prevalent, liquid water and para-hydrogen. In addition to this work, an investigation is carried out into the role of nuclear quantum effects in the free energies of hexagonal and cubic ice, as hexagonal is only more stable by ≈ 40 J mol^{-1} and it has not been shown what causes this extra stability, as the two polymorphs have almost identical properties and differ only in their stacking arrangement. Our results show that the inclusion of nuclear quantum effects stabilises hexagonal ice relative to cubic ice, leading to a greater free energy difference more in line with experimental values. Finally we examine how nuclear quantum effects play a role in the surface properties of small water droplets and how ion diffusion is affected, as there is interest in how these droplets may play a role in or catalyse chemical reactions.

Chapter 1

Introduction

This Chapter provides an overview to the field in which the work presented here is set. The various types of water potentials used in molecular simulations are discussed along with an in-depth look at the q-TIP4P/F model used in this work. An overview of work done on free energies of solid aqueous phases is presented along with the discussion of results of prior work which has motivated some of the work done here. A brief examination of water droplets is given and finally a short overview is given detailing the contents and layout of the chapters to follow.

"The Lord is my shepherd, I'll not want.
He makes me down to lie, in pastures green,
he leadeth me, the quiet waters by.
THE WEST BROM!
THE WEST BROM!"

-Psalm 23 (WBA)

During the last 50 years atomistic simulations of chemical systems have been improving at a very fast pace. This has been because of the development of more efficient and increasingly accurate techniques that can describe the quantum mechanical nature of the electron. While this has undoubtedly been successful the main problems plaguing the majority of simulation methods is the requirement for a suitably accurate Potential Energy Surface (PES)[1–4], with the assumption that the nuclei of atoms are classical and as such have no quantum mechanical contribution becoming increasingly relevant.[5] The justification for this assumption has always been due to the complexity of including quantum nuclei and the associated increase in computational cost that accompanies this, however this assumption is now one of the biggest sources of error when using the most modern descriptions of chemical systems. In more recent years this has led to the development of a number of methods that have dramatically reduced the computational cost of including these effects and allowed the investigation of systems where Nuclear Quantum Effects (NQEs) are fully accounted for without the requirement of a large amount of resources, in fact these simulations can now be carried out to a certain degree on standard desktop computers.[6–15] As part of the development of these methods, this work details a novel method that can be used to speed up quantum simulations by up to a factor of 2 with a negligible loss of accuracy, with the added benefit of being able to be applied to any chemical system of interest.[15]

This renaissance of quantum computational methodology has also opened the door for the investigation of systems that have previous been the subject of plentiful examination using purely classical techniques, as the complete inclusion of NQEs[7,16–20] can paint an entirely different picture of the interactions within a system. As part of this we examine one of the most studied systems in computational chemistry, water. We do this in the liquid phase in the implementation of our new method as well as the study of its surface properties in small droplets. We also carry out examination of the solid phase, specifically the free energy difference between hexagonal, cubic and stacking disordered ice.[16,17,20–27] These properties have been examined before using classical methods but there is very little study been done using a fully quantum method. Our work can be differentiated from this by our use of a fully anharmonic water model (q-TIP4P/F), which adds another part of the investigation, as much of the work done on water in the past has been with rigid models that negate the role of anharmonicity. By carrying out the work done here in a manner that completely accounts for quantum effects and uses an anharmonic water potential, this work provides a completely new level of

understanding for the properties being studies and is able to offer new explanations for phenomena that could not be fully explained using a classical system.

The rest of this introduction will first show the potential energy models available to simulate liquid water and some of the classical work carried out on them. Then this introduction will aim to illustrate the importance of NQEs in systems and why their inclusion is of vital importance when investigating aqueous systems. As well as this, an overview of recent methodologies that aim to improve the efficiency of the available Path Integral (PI) quantum mechanical methods is given. A further Section will examine the previous work done with water ice phases and the explanations for the free energy difference between them with a final part looking at work done on the surface properties of small water droplets.

1.1 Simulations of water

Water has been studied since the advent of computational methodology and Molecular Dynamics (MD) simulations using classical Newtonian mechanics have been used extensively to study its properties.[16,17,20–27] In order to perform these simulations a water model is required that can describe the interaction energy and forces of the molecules. There are many models that have been developed that allow for varying degrees of accuracy. A Section describing these models follows, then an overview of some of the previous classical work performed on water.

1.1.1 Water models

In computational chemistry there exists a vast number of water models that can be used in MD simulations. These can be broadly split into three non-exclusive categories: rigid models; flexible models; and polarizable models.

Rigid models have the atom positions fixed to match the known geometry of water and calculate only non-bonded interactions (bonded interactions are implicitly included by the fixed positions). For these models the number of fixed sites can vary, the smallest number being the one-site model developed by Molinero[28] that models water as an intermediate element between carbon and silicon. One of the most common type of model is the three-site model[29] which has fixed sites on each atomic position. Four-, five- and six-site models[30–32] have also been developed which use more fixed points to better describe the system. In a four site model there exists a negative partial charge

	Type	R_{OH}(Å)	$\theta_{HOH}(^o)$	μ(D)	ϵ
SPC	R	1.0	109.47	2.27	65
TIP3P	R	0.95	104.52	2.35	82
TIP4P	R	0.95	104.52	2.18	53
TIP5P	R	0.95	104.52	2.29	82
q-TIP4P/F	F	0.98	104.70	2.34	60
q-SPC/Fw	F	1.01	106.20	2.47	90
TIP4P/FQ	P	0.95	104.52	2.62	79
SPC/FQ	P	1.0	109.47	2.83	115
Expt		0.97	105.1	2.95(298 K)	78

Table 1.1: Table showing water properties calculated for liquid water models compared to experimental values. The models are rigid (R), flexible (F) or polarizable (P). The properties are the O-H bond length, the H-O-H bond angle, the total dipole moment (μ) and the dielectric constant (ϵ). All data was obtained at 25 °C and 1 atm.[21,29–31,33–36]

on a fourth 'dummy' atom (m-site) below the O atom. In a five-site model the partial negative charges sit on the two lone pair sites of the O atom with a pseudo-tetrahedral geometry. The six-site model combines the four- and five-site models to split charges across the lone pair sites and the 'm-site'. The computational cost of using a rigid water model increases with the number of sites, as the number of interatomic distances required to calculate the potential is greater in a model with more sites. The accuracy of these rigid models are shown in Table 1.1, where a comparison of the SPC, TIP3P, TIP4P and TIP5P is shown compared to experimental data. From the data it can be seen that increasing the number of sites in the rigid models leads to an increase in accuracy for the dipole and dielectric constant from TIP3P to TIP5P, with the SPC model falling in the middle. However the SPC model has its own drawbacks in the form of incorrect O-H bond length and H-O-H bond angle.

Flexible water models improve over rigid models by including bond stretching and angle bending and enable the reproduction of the vibrational spectra of water, which can be compared directly to experiment. In these models terms are included to account for intramolecular bonding as well as the standard intermolecular terms. The model used exclusively in this work is the flexible 4-site q-TIP4P/F model.[21] A comparison of this model with another flexible model q-SPC/Fw is shown in Table 1.1.[34] The q-TIP4P/F model is discussed more in the next Section and its equations given in Chapter 2. The q-SPC/Fw is a flexible version of the SPC model that has also been optimised for quantum simulations. From the data it can be seen that the q-TIP4P/F

model is much closer to the bond length and angle than the q-SPC/Fw model however it is not as good at capturing the dipole or dielectric constant, however this is not a large error.

Another type of water model is the polarizable model which includes explicit polarization terms that enhance the ability to reproduce water in different phases. These models were first introduced in the late 1970s by Barnes *et al* and since then have become increasingly developed, with two popular examples being the SPC/FQ and TIP4P/FQ models.[35,36] The SPC/FQ model is a version of the rigid SPC model[33] modified to include fluctuating charge and the TIP4P/FQ model is a variant of the original TIP4P model[30] that has been modified to include fluctuating charges. The properties of these are compared in Table 1.1 and it can be seen that the TIP4P/FQ model is much closer to the experimental values of all properties except the total dipole. As the SPC/FQ model is based on the SPC model, the bond angle is higher than expected, with the dielectric constant much higher than the exact value, however it does a good job of reproducing the dipole.

A final type of model that can be used are ones based upon a many-body expansion of the interaction energy in water models. One popular model of this type is the MB-pol model developed by Paesani *et al.*[37] This model explicitly treats one-, two- and three-body terms and can be viewed as a classical polarizable potential supplemented by short range two- and three-body terms that represent quantum mechanical interactions. In this model, all induced interactions are described through many-body polarization. The model itself does not contain any empirical parameters and has been used to accurately describe the properties of gas-phase clusters. The model has also been used in Path Integral Molecular Dynamics (PIMD) and Centroid Molecular Dynamics (CMD) simulations to describe the liquid phase of water, with results being very favorable when compared to experiment.[37]

The models discussed above and many others have been used over a number of years in MD simulations of water, however it is clear from the data shown and properties that can be calculated that there is no water model that can provide a fully accurate description of all aspects of water. In many cases, models are parameterised to reproduce certain experimental values, with their use outside those properties leading to very inaccurate data. The water model we use exclusively in this work, q-TIP4P/F, also suffers from its own drawbacks however we believe that this model is sufficiently accurate in all relevant areas to the work carried out.

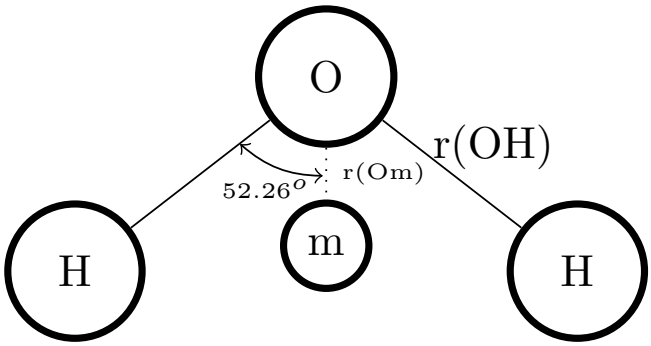

Figure 1.1: Illustration of the q-TIP4P/F water model. This model contains four sites, one on each atom and a fourth so called m-site sitting below the oxygen.[21]

1.1.1.1 q-TIP4P/F

The q-TIP4P/F water model[21] is four-site and is flexible as well as anharmonic in the O-H stretching vibration. This model is based on the TIP4P/2005[38] and parameterised to reproduce liquid structure, diffusion coefficient and infra-red absorbtion frequencies when used in fully quantum simulations. The interaction equations for this model are given in Chapter 2. This model solves the 'double counting' issue seen in other water models, the inclusion of NQEs and the idea of competing NQEs[21,27,39–42] are discussed later in the Chapter. As an example, the diffusion coefficient for this model is $\approx 15\%$ larger than the corresponding classical simulation rather than the much larger 50% seen in other work using rigid or harmonic water models. This difference is due to the observation that there are competing quantum effects in the water model when anharmonicity is included. This is because the quantum effects are different in the inter- and intramolecular parts of the system. In the intermolecular region, the dynamics are sped up due to the disruption to the hydrogen bonding. However, in the intramolecular region, quantum effects result in a larger monomer dipole moment, which increases the strength of intermolecular interactions and slows the molecular motion. This means that the two quantum effects are in direct competition, which is something that is not observed in any other water models.[21] An illustration of this model is shown in Fig 1.1. A property where the size of the quantum effects can be compared directly to experiments is the diffusion coefficient. For the q-TIP4P/F model, the magnitude of the quantum effect can be determined as the ratio of the quantum result with the classical result, in this case it is 1.15, which is much smaller than other water models, which suffer from the

'double counting' problem. This model has been applied to the long-standing issue of attempting to reproduce the water phase diagram. This was done by Habershon and Manolopoulos in 2011[16,43] using a classical method and their results are discussed in a later Section. The parameters used in the q-TIP4P/F model are outlined in Table 1.3. There are nine total parameters for the q-TIP4P/F model, the intermolecular parameters are ϵ, σ, q_M and γ, which take the same values as in the TIP4P/2005 potential on which this model is based. The intramolecular parameters are $D_r, \alpha_r, r_{\text{eq}}, k_\theta$ and θ_{eq} and were optimised in a series of calculations to give good agreement with the experimental structure, self diffusion coefficient and vibrational absorption frequencies of liquid water in quantum simulations. The q-TIP4P/F potential is further outlined in Chapter 2 as an example of how non-bonded and bonded forces are calculated in an MD simulation. Some static and dynamic properties calculated using the q-TIP4P/F model compared to the q-SPC/Fw model[34] are shown in Table 1.2. It is clear from the static results that there is a difference between the average quantum geometries of the two models when investigating room temperature liquid water. As mentioned earlier, the bond length and angle in q-SPC/Fw is greater than in q-TIP4P/F and despite having smaller partial charges, the q-SPC/Fw has a slightly higher average monomer dipole moment, with the densities for both models being close to the experimental value. One of the biggest discrepancies in the data is in the melting point of the two models. q-TIP4P/F has a melting point that is approximately 22 K lower than the experimental value, with the q-SPC/Fw model being around 78 K lower than experiment. For q-TIP4P/F, this better approximation comes from the properties inherited from the underlying four-site TIP4P/2005 model, which classically melts at 252 K. The large error in the q-SPC/Fw model is seen due to it being based the three-site SPC model, which have consistently lower than expected melting points.

Now looking at the dynamics properties of the two models, it can be seen that the q-TIP4P/F model give a very accurate description of the diffusion coefficient, which is not a surprise as the model was initially parameterised to correctly reproduce this value for liquid water. The coefficient ratio between the H_2O and D_2O is also in good agreement with experiment, which is important as the diffusion coefficient provides a method for direct comparison to experimental values. The orientational relaxation are shown however for the q-SPC/Fw model these results were obtained using the CMD method rather than the Ring Polymer Molecular Dynamics (RPMD)[7,17,21,26,44–53] method used for q-TIP4P/F. In this case, both models give good descriptions of the orientational relaxation in quantum simulations compared to the exact exper-

Property	q-TIP4P/F	q-SPC/Fw	Expt
Static Properties			
$\langle r_{\mathrm{OH}} \rangle$(Å)	0.978	1.019	0.97
$\langle \theta_{\mathrm{HOH}} \rangle$(deg)	104.7	106.2	105.1
$\langle \mu \rangle$(D)	2.348	2.465	2.95 (298 K)
ρ_{298} (g cm^{-3})	0.998	1.002	0.997
T_{melt} (K)	251	195	273.15
ϵ_r	60	90	78
Dynamic Properties			
$D_{\mathrm{H_2O}}$ (Å^2 ps^{-1})	0.221	0.24	0.230
$D_{\mathrm{D_2O}}$ (Å^2 ps^{-1})	0.172	...	0.177
$D_{\mathrm{H_2O}}/D_{\mathrm{D_2O}}$	1.28	...	1.30
τ_1^{HH} (ps)	5.40	3.80	...
τ_1^{OH} (ps)	5.10	4.10	...
τ_1^{μ} (ps)	4.64	4.70	...
τ_2^{HH} (ps)	2.22	1.85	1.6-2.5
τ_2^{OH} (ps)	1.90	1.70	1.95
τ_2^{μ} (ps)	1.52	1.60	1.90

Table 1.2: Static and dynamic equilibrium properties of the q-TIP4P/F water model from PIMD and RPMD simulations respectively at 298 K and density of 0.997 g cm^{-3} (1.107 g cm^{-3} for heavy water). Dynamic properties were calculated for q-SPC/Fw using CMD.[21,34]

imental value.

1.2 Nuclear quantum effects

The foundations of computational chemistry are made of approximations that allow easier calculation of properties. One of the most famous is the Born Oppenheimer approximation which allows the separation of the nuclear and electronic wavefunctions when calculating PESs. Another major assumption commonly made in atomistic simulations is that nuclear motions and sampling of the electronic energy surface can be done classically using Newtons laws of motion[54], discussed in Chapter 2. This has some major implications as treating the nuclear motion classically neglects the role of nuclear Zero-Point Energy (ZPE), energy level quantization and quantum tunnelling. This is not a good approximation when examining systems where these effects are preva-

Parameter	q-TIP4P/F
ϵ (kcal mol^{-1})	0.1852
σ (Å)	3.1589
q_M ($\|e\|$)	1.1128
γ	0.73612
D_r (kcal mol^{-1})	116.09
α_r (Å^{-1})	2.287
r_{eq} (Å)	0.9419
k_θ (kcal mol^{-1} rad^{-2})	87.85
θ_{eq} (deg)	107.4

Table 1.3: Parameters in the q-TIP4P/F quantum water model.[21]

lent (low temperature and small atoms) and can lead to significant errors. As an example the ZPE of a chemical bond can exceed the thermal energy scale of its coordinate at room temperature by an entire order of magnitude. Therefore quantum effects can have a large impact on structure and dynamics of a chemical system. One example of this that is studied in this work is the stability of crystal polymorphs, in this work we examine two ice polymorphs, hexagonal ice and cubic ice shown in Fig 1.2 and examined further in Chapter 4. As the stability of phases can change quantum effects can therefore also be responsible for phase diagrams changing. One final example of a consequence of not including NQEs is that equilibrium isotope effects would be predicted as non-existent, despite these effects being a key part of commonly used analytical chemistry methods. To show the importance of NQEs in chemistry, the concept of ZPE and quantum tunnelling will be showcased in more detail in the following sections, followed by a more specific case of how quantum effects can 'compete' against each other within the system of liquid water.

1.2.1 Zero point vibrational energy

ZPE refers to the energy of a chemical system at temperature $T = 0$ K, or another way of describing it is the lowest quantised energy level that a system possesses. The origin of this energy arises in a quantum system due to the Heisenberg uncertainty principle,

$$\sigma_x \sigma_p \geq \frac{\hbar}{2} \tag{1.1}$$

where σ_x and σ_p are the standard deviations of the position and momentum respectively and $\hbar$ is the reduced Planck constant. This principle states that

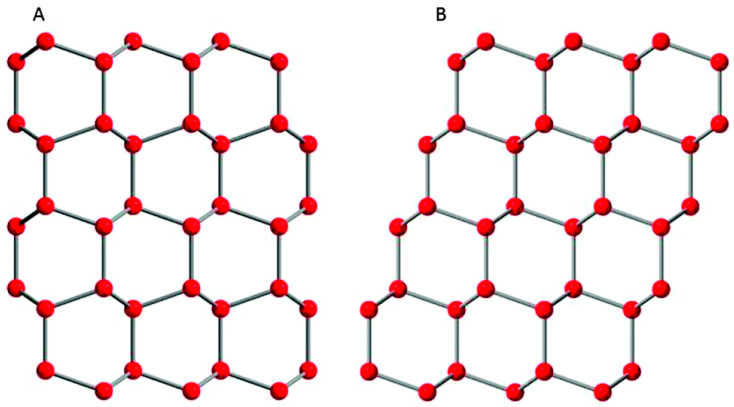

Figure 1.2: Illustration of the two ice-I variants, hexagonal ice (a) and cubic ice (b).[55]

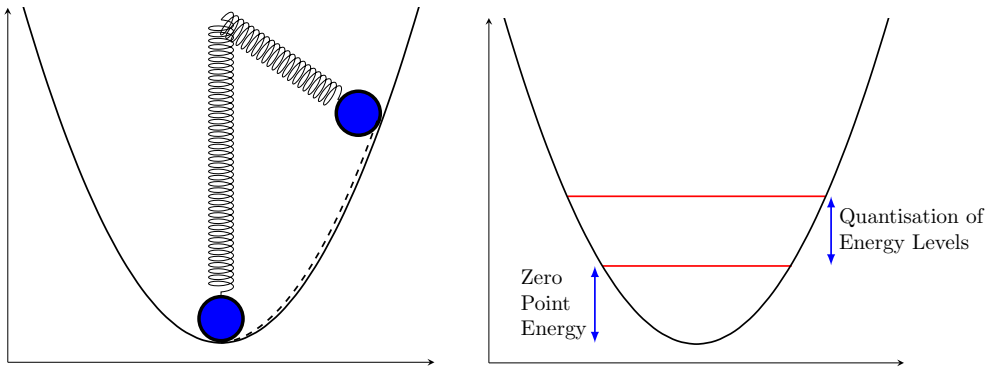

Figure 1.3: Illustration of a classical harmonic oscillator (left) and a quantum harmonic oscillator (right). The classical oscillator can be likened to a mass attached to a spring or pendulum, the mass will come to a stop at zero energy. The quantum oscillator contains a ZPE due to the Heisenberg uncertainty principle and the quantisation of energy levels.

the more precisely the position of a particle is determined, the less precisely its momentum can be determined, and vice versa. The lowest possible amount of uncertainty of the position multiplied by the momentum is specified by Plancks constant. This minimum amount of uncertainty cannot be corrected by methods of measurement but instead arises from the wave like quantum nature of the particle. The behaviour of ZPE can be seen clearly in the case of liquid helium, which does not freeze even as the temperature is lowered to absolute zero due to the ZPE of the system caused by its own atomic motion that cannot be removed. At these temperatures helium also behaves as a Bose-Einstein condensate, where its quantum mechanical properties cause the liquid to climb the sides of any open container it is stored in. It should be noted however that Helium can be made to freeze by significantly increasing the pressure along with the absolute zero temperature.[18,56]

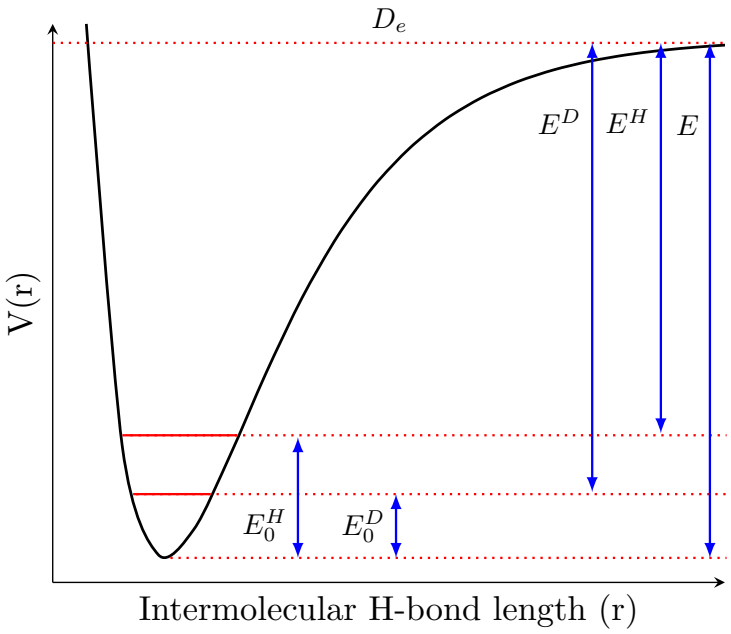

Figure 1.4: Illustration of the intermolecular bond strength of water and heavy water. In this case the dissociation energy is the energy required to break a hydrogen bond between two water molecules. Therefore the point where all hydrogen bonds within an aqueous system are sufficiently separated can define the energy required to melt from the solid phase. It can be seen that the ZPE for water is more than that of heavy water due to it being lighter and smaller. This means that water has a lower melting point than heavy water as more energy is required for it to reach the dissociation energy.

A more simple example that can be demonstrated here is the use of a harmonic oscillator. Classically (mass on a spring), the oscillator can always be brought to rest at zero energy, however a quantum harmonic oscillator does not allow this to happen. The requirements of the uncertainty principle mean that there will always be some residual motion of the system as the position cannot be entirely known to be zero, while also knowing that there is zero momentum. This results in a ZPE, which can be calculated as equal to $\frac{1}{2}$ hw, where w is the frequency of the oscillation. Examples of this are shown in Fig 1.3, where both the classical and quantum oscillators are shown for comparison.

A real world example that highlights the importance of ZPE can be seen in the comparison of the melting points of two different isotopes of water (H_2O and D_2O) and is shown in Fig 1.4. Due to the hydrogen being lighter and smaller than the deuterium, the ZPE for H_2O is greater than that of D_2O. The consequence of this is that D_2O melts at a temperature $\approx$ 4 K higher than H_2O. This is very significant as without this ZPE water as we know it would not melt at 273 K but $\approx$ 277 K instead, which would have had a dras-

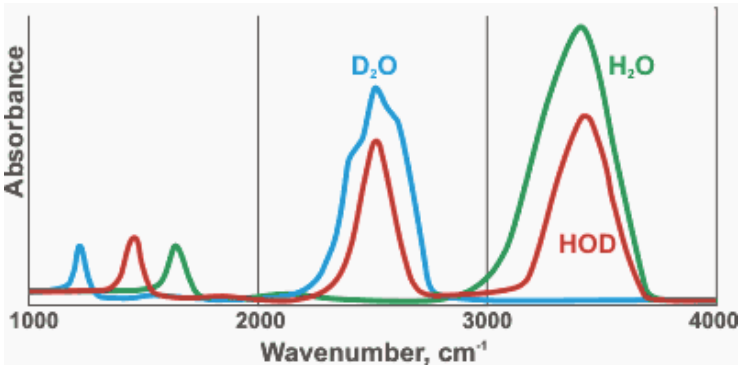

Figure 1.5: Vibrational spectra of water, heavy water and a single deuterated water molecule.[57]

Property	D_2O	HDO	H_2O
Freezing Point (K)	276.97	275.19	273.15
Boiling Point (K)	374.55	373.85	373.15
Density at STP (g/ml)	1.1056	1.054	0.9982
Surface tension at 298 K (N/m)	0.07187	0.07193	0.07198
pH at 298 K	7.44 (pD)	7.266 (pHD)	7.0

Table 1.4: Table of data comparing properties of heavy water, semi-heavy water and normal water.[59]

tic impact on the development of life on Earth over the past millennia.[23,58] Further examination of the difference between the two can be seen in Fig 1.5, which shows the vibrational spectra of water, heavy water and a single deuterated version.[57] All of the bands present in this spectrum are made up from contributions of water molecules in different hydrogen bonding environments, therefore it can be said that lower frequency components are attributed to molecules with stronger hydrogen bonds and higher frequency components having weaker hydrogen bonds. It can be seen for all bands that deuterated water appears at lower frequencies, followed by the single deuterated water, and then normal water. This is in line with the observations of the dissociation energies discussed above that the hydrogen bonds are stronger in heavy water due to the reduction in ZPE. Table 1.4 shows a comparison of a number of properties of the three water analogues to further emphasize the point that the difference in ZPE due to the increased size of heavy water leads to a difference in many properties. In particular the experimental properties clearly show how the ZPE lowers the freezing point and boiling point of normal water compared to heavy water.

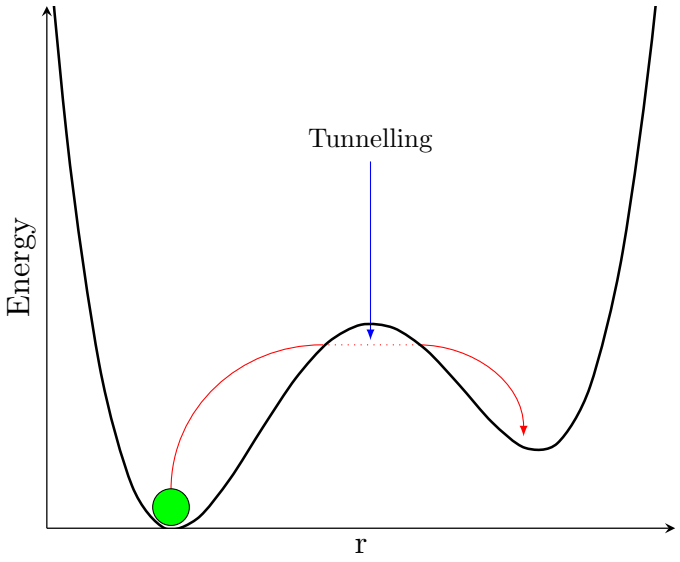

Figure 1.6: Illustration of the quantum tunnelling effect. There always exists a probability for a quantum particle that a barrier can be overcome without having the required energy due to the Heisenberg uncertainty principle. This is not the case for a classical particle, where tunnelling does not occur.

1.2.2 Quantum tunnelling

Quantum tunnelling was first encountered in the late 1920s during a calculation of the ground state of a double well potential and was used soon after to help mathematically explain alpha decay. This phenomena occurs in quantum systems and as such is completely neglected when investigating a system using purely classical methods. The simplest explanation of the difference between the classical and quantum treatment in regards to this effect can be seen when a particle is attempting to overcome a potential energy barrier. In the classical treatment if the particle does not have the required energy then it will not be able to overcome the barrier and move to the other side, meaning it would simply remain where it started and never be able to leave the well without an increase in the supplied energy. However this is not the case when a quantum method is applied, where there is a small probability that the particle can 'tunnel' to the other side of the barrier without the required energy to overcome it. The reason for this difference in classical and quantum treatment again comes from the Heisenberg uncertainty principle and the idea that there is wave particle duality. This in turn means that for the example of a particle overcoming a potential energy barrier there are no quantum solutions with a probability of exactly zero.

An example of tunnelling is shown in Fig 1.6 where a particle in a double

well passes through the energy barrier to the other side. Quantum tunnelling is an important phenomenon in many different areas of chemistry, with its most important application being seen in nuclear fusion in stars. This is due to the pressures and temperatures in the core being insufficient to begin fusion. However due to the quantum tunnelling effect there is a small probability that the barrier can be overcome and due to the vast amount of nuclei present in the core of a star, a fusion reaction is generated that can last for millions of years, allowing for the evolution of life as we know it. Other notable applications can be found in radioactive decay, other types of astrochemistry, analytical techniques such as scanning tunnelling microscopy, proton transfer in proteins and tunnelling in electron transfers.[50,60–63]

1.2.3 Competing quantum effects

In the study of any chemical system, it is important to fully include NQEs[7,16–20] in order to remove error from the properties being calculated. In this work we look at liquid water, which has a vast number of potential models that can be used to describe it, which were discussed earlier in the Chapter. These have improved in accuracy over the years and has resulted in the properties of liquid water being much better understood. The necessity for the inclusion of NQEs in this system has been known for over 30 years due to the classical simulations being unable to match experimental data as discussed earlier. The development of PIMD has played a key role in allowing this to be carried out. However it is still not fully understood how NQEs affect the properties of liquid water. Early studies using PI methods showed that NQEs weaken the hydrogen bonding in liquid water and therefore cause it to be less structured than is predicted using only classical methods.[24,34,64] More recent PI methods have allowed the role of these quantum effects to be studied in the dynamic properties of the liquid. The work done using these methods has found that the rates of translational diffusion and orientational relaxation are 1.5 times faster when NQEs are included.[21] The same effects have been found when using other computational studies that include quantum effects seemingly confirming the decrease in liquid viscosity and an increase in the orientational relaxation and translational diffusion.[23,24,65,66]

Recent studies have shown however that this may not be the case, as most work done on this topic have used empirical potential models that were parameterised using classical simulations. By carrying out a quantum calculation using these models, one runs into the issue of 'double counting' of the quantum effects in both the structural and dynamic properties .[23,24,26] This

Model	Method	$D_{\mathrm{cl}}(\mathrm{\AA}^2\mathrm{ps}^{-1})$	$D_{\mathrm{qm}}(\mathrm{\AA}^2\mathrm{ps}^{-1})$	$D_{\mathrm{qm}}/D_{\mathrm{cl}}$
q-TIP4P/F	RPMD	0.192	0.221	1.15
SPC/E	RPMD	0.242	0.343	1.42
SPC/F	RPMD	0.279	0.400	1.43
SPC/F	CMD	0.300	0.420	1.40
TIP4P	CMD	0.358	0.548	1.53

Table 1.5: Classical vs quantum diffusion coefficients for liquid water models. The ratio of the quantum result to the classical result is also shown. The ratio for the q-TIP4P/F model is significantly lower than the other models used for comparison.[21]

leads to properties being calculated that are much larger than the corresponding experimental value. Another issue is that the majority of empirical water models are rigid bodies in the treatment of the water monomer, while this does make the computational calculations more efficient, it completely ignores the role of flexibility and the role it plays in the structure and dynamics of the liquid. While some water models do include intramolecular flexibility, the majority use simple harmonic potentials to describe it. However the O-H bond has a significant anharmonic vibration which can be seen in the broadening of the stretching band in the IR spectrum, which is ignored in these models.[67–69] This means that the vast majority of water models that have been used in the calculation of quantum properties in liquid water have been entirely unsuitable. In this work, we use a relatively new water potential, the q-TIP4P/F model[21], which addresses these issues to remove the existing errors when including NQEs in simulations of liquid water. An example of this was discussed earlier and is shown in more detail in Table 1.5, which shows the classical and quantum diffusion coefficient for a number of water models and the resulting ratio between the two values. For the q-TIP4P/F model this ratio is 1.15, which is significantly smaller than the other models and is a direct result of the features of the model introduced earlier, where the intra- and intermolecular NQEs directly oppose one another and therefore give a smaller overall quantum effect compared to the classical. Rigid models do not incorporate this and the overall result is one where models 'double count' the NQEs, leading to the larger ratios observed in Table 1.5.

1.2.4 Including quantum effects

Discussed in more detail in Chapter 2, the PI approach provides an effective method of explicitly including NQEs in the simulation of a chemical system. This basis was discovered by Richard Feynman by determining that the minimum action principle of classical mechanics (which simply states that the trajectory taken between two configurations over a time interval is the one that makes it locally stationary) can be extended by considering not just the minimum path, but also paths which deviate from this as well. By doing this and summing over the amplitudes from all available paths between the two configurations, quantum mechanical effects become fully included. However as this would clearly be massively expensive, it is possible to achieve a similar result by only considering paths that deviate from the least action by a small amount. While this is less expensive, it is still computationally prohibitive for any significant system size. This can be further simplified if one is only interested in examining static properties of a system, as there are no longer paths between configurations to evaluate, instead the problem can be mapped onto n replicas of the classical system, with harmonic springs connecting corresponding atoms.[18]

In our work we use the imaginary time PI formalism, which means we use the path integral representation of the matrix elements of the quantum statistical operator or density matrix at thermal equilibrium. This allows the description of quantum statistical physics in terms of a path integral, and as we show in Chapter 2, how this links to classical statistical mechanics allowing the quantum properties of a system to be calculated using classical mechanics, which is only n times more expensive than just the classical simulation. A number of computational methods have been developed based upon this core idea in order to allow the inclusion of NQEs in computational simulations. A few examples of these are quantum transition state theories, CMD[23,70–75] and RPMD[7,17,21,26,44–53] and other variants. However the development of these methods has been somewhat limited by the issue of computational cost and therefore they are not implemented in the majority of commercial quantum chemistry software packages. A typical PI calculation can be of the order of tens to hundreds of times more expensive than that of a classical simulation, mainly due to the reason described above of having a large number of system replicas all connected together and requiring their own independent evaluation of forces. While this number is not necessarily always high, it grows rapidly as the temperature decreases due to quantum effects becoming more prevalent in that regime as well as rapidly increasing when the maximum vibrational

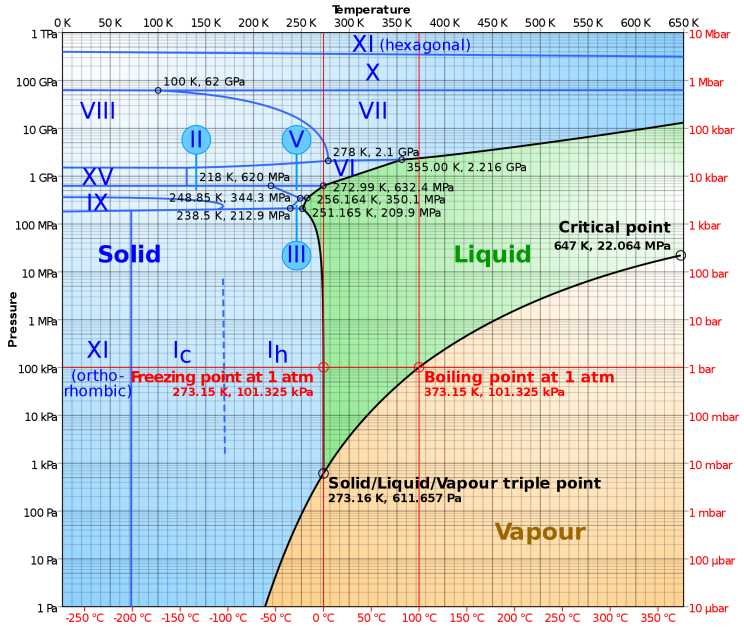

Figure 1.7: Illustration of the phase diagram of water.[85]

frequency of a system increases. In a bid to address this, a large amount of recent work in the field has been aimed at developing new methodologies that can perform a full quantum PI simulation, while significantly reducing the time taken to do so. Examples of these are presented in Chapter 2 with our novel method for accelerating PI simulations in Chapter 3.[15]

1.3 Solid water phases

The phase diagram of water provides an insight of the difficulties in computationally modelling this substance. At present the phase diagram (shown in Fig 1.7) contains 15 separate solid phases which are all structurally different as water can stack in a large variety of ways due to the monomer containing two potential hydrogen bond accepting sites and two hydrogen bond donor sites.[76–81] As an example of this, the hexagonal ice phase (I_h) exhibits a disordered proton arrangement, can be transformed into a proton ordered phase (ice-XI) at low temperatures. Another interesting solid phase is ice-X, which can only be formed at high pressures and is characterised by each proton covalently shared by two neighbouring oxygen atoms. Amorphous water phases also exhibit strange behaviour[82], for example upon supercooling, the liquid can transform into a metastable low-density amorphous (LDA) phase, which can also then transform into a high-density amorphous (HDA) phase when placed under high pressure. The relationships between these and other forms of water are still being investigated using computational methods.[83,84]

The features found in the phase diagram arise from the fact that the interactions between atoms are strongly directional and can have bonding interactions that range from weak hydrogen bonds to much stronger covalent bonds. In addition to this, water has a very large electronic polarizability, meaning that charge distributions can change massively between different phases.[86,87] All of this means that water is computationally very difficult to model. NQEs also play a role in the properties of water and therefore need to be included in order to form an accurate picture, which only serves to increase computational cost further. Previous studies of water using quantum path-integrals have confirmed this importance in static properties such as the heat capacity.[22,88–91] Dynamic properties such as the diffusion coefficient have also been studied and again it has been found that the inclusion of NQEs is essential to obtaining an accurate picture of the properties of liquid water and by extension the phase diagram.

The reproduction of the experimental phase diagram can therefore be considered a robust test for any water model. This has led to many researchers to investigate the phase behaviour of rigid water models (anharmonicity is neglected, discussed in Chapter 2).[38,92–94] These studies have utilised thermodynamic integration to an appropriate reference state, which is also the method we use in our study in Chapter 4. It has generally been found that 3-site models do not perform well when reproducing the water phase diagram, with 4-site models improving by providing some agreement with experiment. The 3-site SPC/E model[95] has been used in many studies of liquid water, however when it is used to predict the phase diagram the ice-III and ice-V phases are completely absent with the I_h and liquid boundary occurring at negative pressures.[93] As a contrast to this, four site models such as TIP4P[29] and TIP4P/2005[38] reproduce all the ice phases with no absences, albeit with the phase boundaries and triple points mostly shifted to lower temperatures and higher pressures than is generally seen in experimental results.

These results have showed what qualities are important in a water model. The SPC/E model fails due to the low quadrupole which is generally typical of all 3-site water models. This is remedied in 4-site water models where the quadrupole moment is higher, this is also accompanied by other improvements such as more accurate melting points.[96] However even with this improvement, these models are still rigid and do not account at all for intramolecular flexibility or the role NQEs play in affecting the phase diagram (particularly at low temperatures where these affects are more prevalent). Until recently these effects had not been investigated to the same extent as had been done with rigid models, however work done by Habershon et al[43] provided an in depth

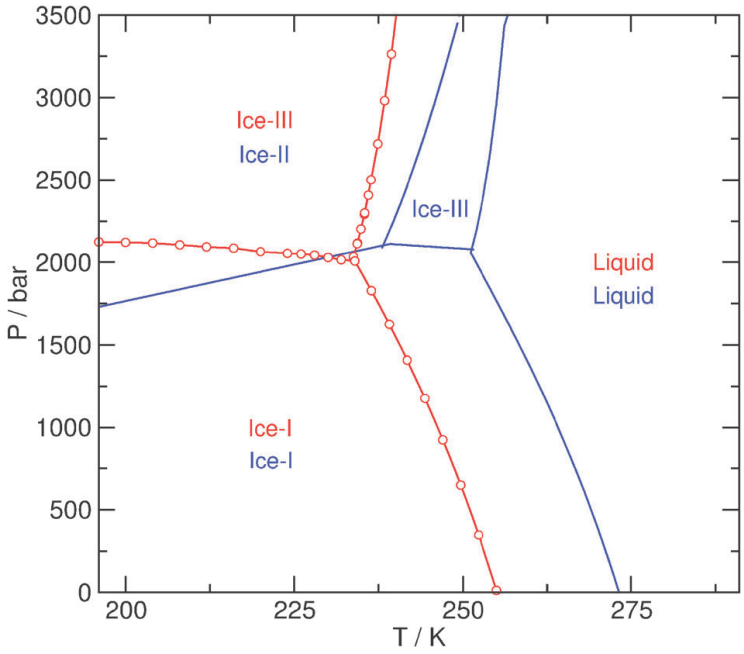

Figure 1.8: Phase diagram of the q-TIP4P/F water model (circles) compared to experimental results.[43,76–78]

investigation of the water phase diagram using the q-TIP4P/F water model[21], which is used exclusively in the work presented hereafter and discussed in the next Chapter.

The results of this study are shown as a comparison between the computational phase diagram and the experimental one in Fig 1.8, however only a range of temperatures from 190 K to 290 K and pressures up to 3500 bar are studied. For the ice-I/liquid phase boundary, this water model is in good agreement with experiments. The negative slope of the melting curve due to the decrease in molar volume during the transition from the solid to the liquid phase. The ice-III/liquid and ice-I/ice-III boundaries also lie within good agreement to experiment, with the ice-I/ice-III/liquid triple point being found at 234 K and at a pressure of 2010 bar. This is close to the experimental triple point of 251 K. The results for this water model are closer to experiment to many other water models. The TIP4P water model has a triple point of 194 K and 3110 bar and the TIP4P/ice model (specifically parameterized to reproduce the ice-I melting point) has its triple point at 232 K and 2955 bar.[97] As mentioned above the work done on these models was classical, however it is unlikely that the inclusion of quantum effects would change this by much.[21]

As mentioned above, using empirical water models with fixed partial charges leads to the melting point of the ice-I phase being lower than the value determined by experiments, this is also observed when using the q-TIP4P/F model. This may be the result of the lack of polarization whose inclusion

Ice phase	Expt.	SPC/E	TIP4P/2005	q-TIP4P/F
I	-0.06	0.682	-0.887	-1.170
II	0.0	0.0	0.0	0.0
III	0.84	2.117	0.444	-0.103

Table 1.6: Potential energies of ice phases relative to ice-II for different water models. All values are given in kJ mol^{-1}.[43,98]

would increase the temperature at which the phase melts by increasing the dipole moment in the ice structure relative to the liquid phase.[86,87]

Another feature of the q-TIP4P/F phase diagram worth noting is the lack of the ice-II phase, which is experimentally seen at temperatures less than 230 K and pressures above 2000 bar. There are no conditions where this phase is predicted to exist instead of the ice-I and ice-III phases. This was investigated further by computing the variations in the free energy of the three ice phases in the phase diagram along an isotherm of 150 K. Experimental results show that the ice-II phase becomes stable at 1500 bar, however it is clear from Fig 1.8 that at no point along the isotherm does ice-II become the state with the lowest free energy. Investigations of other isotherms led to the same conclusions. The reason for this can be found by examining the potential energies of water models at 0 K, These are shown in Table 1.6 and compare 3 different water models.[43,98] The SPC/E model predicts that ice-II is the most stable at 0 K, with the ice-III phase being significantly higher in energy, therefore predicting it to be absent in the phase diagram. In contrast, the TIP4P/2005 model is closer to the experimental results, predicting ice-I being more stable than ice-II with the ice-III phase higher in energy.[93,94] All three of these phases are seen in a low pressure phase diagram in the correct regions. The q-TIP4P/F model studied in this work favours ice-I over ice-III by a large amount with the ice-II phase being even higher in energy, this leads to a low pressure phase diagram where ice-I is seen in the correct region however the ice-III phase exists where it is experimentally predicted that the ice-II phase should appear.

Further understanding of this model was enabled by examining the contributions to the free energies of the ice phases. These contributions are shown in Fig 1.9 and cover the region where ice-II is predicted to prevail as the most stable state in the phase diagram. Also present in this figure are the minimized potential energy, the harmonic vibrational contribution, the PV term and residual entropy. In these results the PV term is consistently greater in

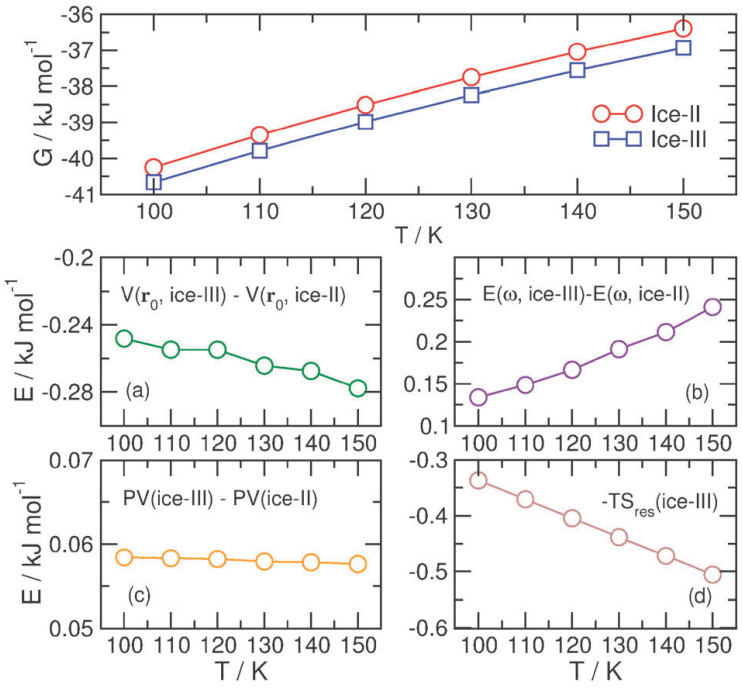

Figure 1.9: Free energy contributions to the ice-II and ice-III phases. The upper panel contains the full free energy, (a) shows the reference potential energy, (b) shows the harmonic eigenvalue contributions, (c) is the PV term, (d) is the residual entropy.[43]

the ice-III phase over the ice-II phase, therefore can be ruled out as a cause of why the ice-III phase is more stable. In terms of the reference potential energies, ice-III is lower than that of ice-II, which agrees with the results discussed in Table 1.6. The increased stability of the ice-III from this is cancelled in part by the harmonic vibrational energy. Therefore it was concluded that the residual energy contribution is a major factor in the stability of the ice-III phase. From these results the conclusion could be made that the ice-III phase is more stable than the ice-II phase due to the potential energy of the ice-III phase being consistently lower than that of ice-II, coupled with the higher residual entropy of ice-III, which is not seen in the ice-II phase, which lowers the free energy of the ice-III phase at all possible conditions, resulting in the metastability of ice-II. In other water models this residual energy term is offset by the differences in the potential energy values meaning that the ordering of the phases is unaffected. The final question answered is why the ice-III potential energy is lower than that of ice-II. This is answered by looking at the coupling between the intramolecular and intermolecular interactions. This is not a feature seen in rigid water models as there is no intramolecular stretching motions. This also gives rise to the competing quantum effects in the model discussed above.[21] The upshot of this flexibility is that the molecules

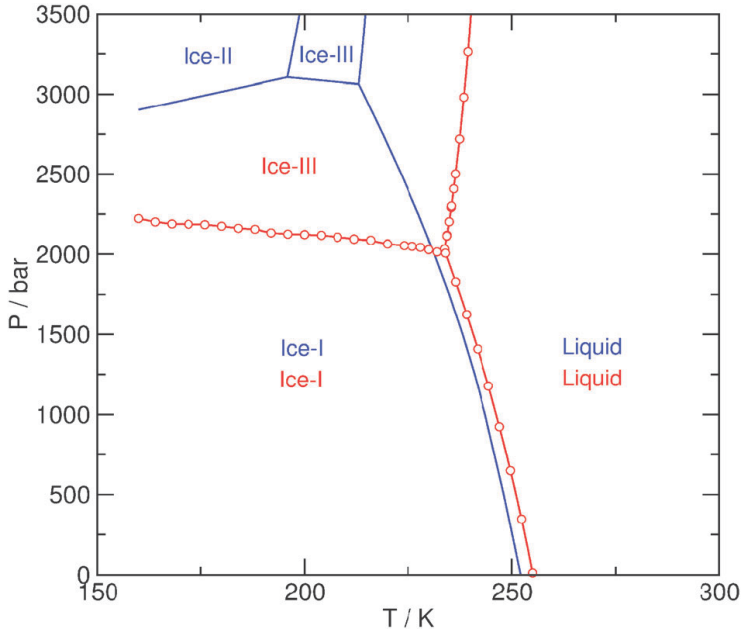

Figure 1.10: Phase diagram of the q-TIP4P/F model compared to the TIP4P/2005 model. The two models have the same intermolecular parameters, therefore this figure highlights the effect of intramolecular flexibility.[21,38,43]

can deviate from equilibrium geometries and the potential energy is increased due to the added intramolecular interactions. However the intramolecular energy results obtained suggest that the q-TIP4P/F model has intramolecular interactions that are too weak in the ice-II phase or the overall intramolecular forces are too strong.

The q-TIP4P/F phase diagram was compared to the TIP4P/2005 model as both have the same intermolecular interactions (even though the flexibility in q-TIP4P/F results in a slightly different geometry). These results are shown in Fig 1.10.[21,38,43] The introduction of this flexibility results in a shift in the ice-I/ice-III phase boundary to lower pressures, which agrees better with experimental data shown above. This is due to larger pressures required to destabilise the ice-I phase in the TIP4P/2005 model as a result of the lower potential energy difference for the model using the data from Table 1.6. While both rigid and flexible water models can be considered quite similar when treated using standard conditions, the outer regions of the water phase diagram are strongly affected by the introduction of flexibility.

Overall the work done on the q-TIP4P/F water model has shown in terms of ice phase free energies, that a reasonable description of the phase diagram can be obtained that is in good agreement with the ice-I/ice-III/liquid triple point as well as being able to provide accurate static and dynamic properties. This work leads us to the work presented in this thesis, where we introduce

NQEs to determine how the stability of the ice-I phase is affected in terms of the two possible polymorphs, I_h and I_c.

The two ice polymorphs of the ice-I phase I_h and I_c are separated by a very small free energy difference, with I_h being the dominant form in nature, and I_c rarely seen at all, in fact it has been suggested that 'pure' cubic ice is never observed and any rare occurrence contains many stacking faults.[55] Stacking faulted variants of ice can be very complex and have properties that depend on the free energy difference between the two pure polymorphs. As the free energies of these two types are so similar, computational methods have been unable to explain why I_h is more stable than I_c. Some studies using density functional theory and Monte Carlo (MC) methods have found that the two ice types are practically degenerate when nuclear motion is neglected, with other work showing that the zero-point vibrational energies are also almost identical when computed harmonically. In general a large amount of computational work has been done on aqueous phases using MD as well as path-integral methods that include NQEs. This has led to the understanding of many properties of water such as isotope effects, reproduction of anomalous thermal expansion and the heat capacity of water.[99–104] Work done on understanding the free energy difference between I_h and I_c have mostly been done using empirical water models such as TIP4P and are usually always done without any description of anharmonicity. TIP4P has been shown to be unsuitable for this investigation as it produces incorrect proton ordering energies as well as an incorrect static lattice energy between the two phases. Recent work has attempted to gain a clearer picture by using a fully anharmonic DFT study using the PBE functional.[99] This work suggested that the origin of the difference between I_h and I_c could be found due to the anharmonicity, specifically in the librational region of the vibrational spectrum. However the PBE functional may not be the best for treating ice phases due to the known overbinding of hydrogen bonds when it is employed.[105] This leads to the conclusion that these results may not provide the complete picture, with the inclusion of NQEs as well as anharmonicity in this work, giving a more complete investigation of the free energy difference.

Chapter 2

Theory

This Chapter sets out the key theoretical elements of the work presented in later chapters. As the vast majority of work performed here uses either classical MD or quantum PIMD. This Chapter begins with a description of the MD approach to computer simulations using the q-TIP4P/F water as an example system. This is followed by the introduction of PI methods for including NQEs. The final part of this Chapter is devoted to the examination of the exact PI methods used in this work as well as showcasing other popular approaches.

"Come with me and you'll be
in a world of pure imagination."

-Willy Wonka

Standard MD simulations use Newton's laws in order to classically evolve a system of interest and calculate static and dynamic properties.[54,106–109] However NQEs can be explicitly included using the classical method by utilising a PI method, albeit at a greater computational cost. The use of MD also requires a method of calculating the potential energy for the system and there are many different methods of doing this. For our work we study solid and liquid phases of water, where there are many different potential models that have been used to study various properties discussed in the previous Chapter.[21,30–32,38]

This Chapter will be split into a number of sections. Firstly a Section will be devoted to discussing classical MD, along with the various ensembles and thermostats used in these simulations. A Section will then be presented on PIMD explaining how the method can be used to completely account for NQEs in classical MD simulations.

2.1 Molecular dynamics

MD simulations have been used extensively since their development in the late 1950s to aid in understanding the properties of molecular systems. These simulations serve as a complement to regular experiments and can also be used to investigate systems that may not be easily studied using conventional methods, such as those in extreme temperature or pressure. MD is also able to determine properties of a system that may not be easily accomplished by experiment alone, such as a velocity autocorrelation functions. MD simulations in general can be as accurate or as general as one prefers, usually this depends on the computational budget available; however it can also depend on the system under investigation. For example when looking at a system with a small number of atoms or molecules or one that has a direct experimental counterpart, a good interaction model is needed to produce accurate results, whereas in some instances the high level of accuracy is simply not required and a cheaper alternative is just as viable.

2.1.1 Molecular interactions

MD simulations utilise Newton's equations of motion to evolve the system through a time step. This begins with Newton's famous second law of motion

$$\mathbf{F} = m\mathbf{a}, \tag{2.1}$$

where $\mathbf{F}$ is the net force acting on the atom, m is the particle mass and $\mathbf{a}$ is the acceleration. The net force $\mathbf{F}$ can be calculated in a number of ways, in this work we use the q-TIP4P/F model, which uses a pairwise potential that is calculated by the summation of all the individual force pairs in the system:

$$\mathbf{F}_i = \sum_{\substack{j=1 \\ (j \neq i)}}^{N_a} F_{ij}, \tag{2.2}$$

$$\mathbf{F}_i = -\frac{\partial V}{\partial \mathbf{r}_i}, \tag{2.3}$$

where f is the force, r is the atom position, N_a is the number of atoms and $V(\mathbf{r})$ is the potential energy. Note that the summation does not include an atoms interaction with itself and atom pairs only need to be examined once as $f_{ji} = -f_{ij}$. The calculation of the individual forces can be derived from the potential energy $V(\mathbf{r})$, where $\mathbf{r} = (\mathbf{r}_1, \mathbf{r}_2, \ldots \mathbf{r}_N)$ is the complete set of $3N$ atomic coordinates.

2.1.1.1 Non-bonded interactions

Here we look at an example of how molecular interactions can be calculated for a system of interest. There are a variety of ways in which one can do this, however here we only examine the method used for q-TIP4P/F [21], which uses a Lennard-Jones (LJ) pair potential to approximate the non-bonded dispersion interactions between only the oxygen atoms of the water molecules. This is combined with a Coulomb term that accounts for interactions between all atoms (excluding intramolecular interactions), resulting in the total intermolecular energy of the system. The LJ potential [110] can be defined as

$$v^{LJ}(r) = 4\epsilon \left[\left(\frac{\sigma}{r}\right)^{12} - \left(\frac{\sigma}{r}\right)^{6} \right]. \tag{2.4}$$

Here ϵ is the depth of the potential well, r is the interatomic separation and σ is the distance at which the inter-particle potential is zero. This is illustrated in Fig 2.1, as well as the repulsive and attractive terms to show how the overall potential takes shape. The LJ potential is useful for dealing with short range interatomic interactions such as Van der Waals forces, however it is not appropriate for interactions over a larger range of interatomic separation. To account for this we use a Coulombic term,

$$v^{Coulomb}(r) = \frac{Q_1 Q_2}{4\pi\epsilon_0 r}, \tag{2.5}$$

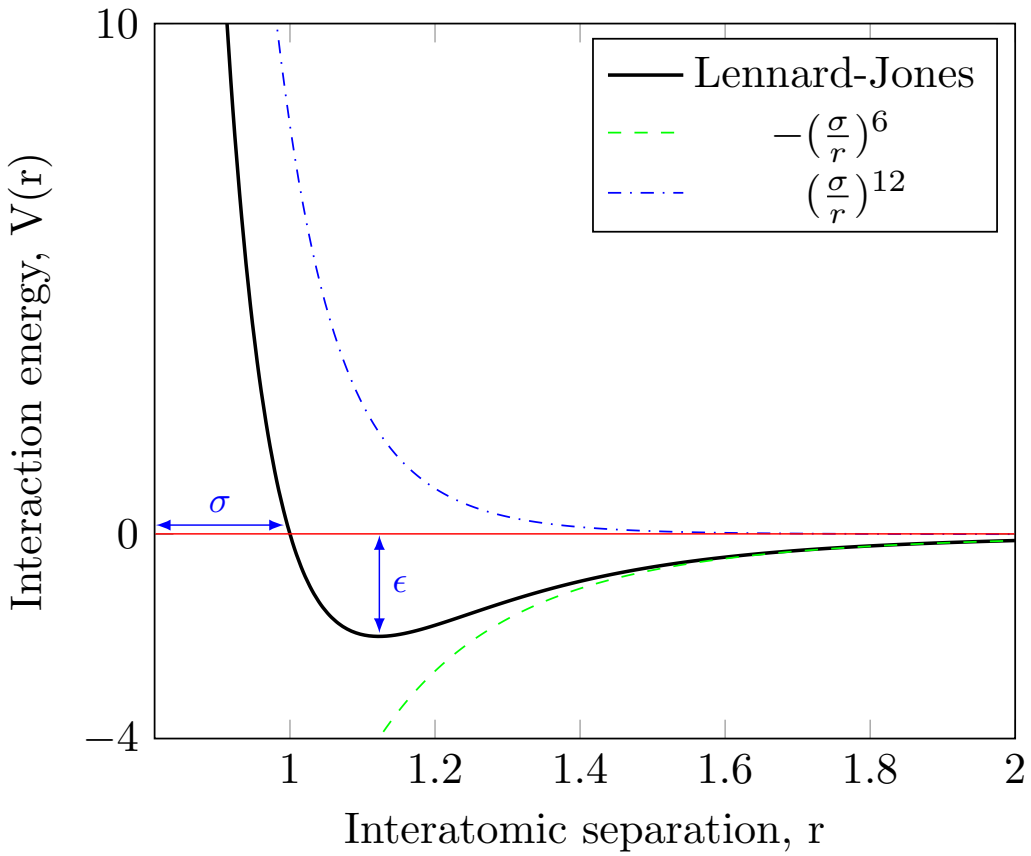

Figure 2.1: Plot of the LJ pair potential (Eq. (2.4)) along with the individual repulsive and attractive terms. Representations of ϵ and σ are shown for clarity.

where Q_1 and Q_2 are the partial charges chosen to account for the electronic distribution in the molecule and ϵ_0 is the permittivity of vacuum. The charges on this model are placed with two positive charges of $Q_m/2$ on the hydrogen atoms and a negative charge of $-Q_m$ is placed at a point $\mathbf{r}_m$ a fraction γ along the vector that connects the oxygen atom to the center of mass of the hydrogen atoms.

$$\mathbf{r}_m = \gamma \mathbf{r}_{\mathrm{O}} + (1-\gamma)(\mathbf{r}_{\mathrm{H}_1} + \mathbf{r}_{\mathrm{H}_2})/2. \tag{2.6}$$

The q-TIP4P/F water model uses a combination of the LJ and Coulomb terms in order to describe the intermolecular interactions in the system,

$$V_{\text{inter}} = \sum_i \sum_{j>i} \left\{ 4\epsilon \left[\left(\frac{\sigma}{r_{ij}} \right)^{12} - \left(\frac{\sigma}{r_{ij}} \right)^{6} \right] + \sum_{m \in i} \sum_{n \in j} \frac{Q_m Q_n}{r_{mn}} \right\}. \tag{2.7}$$

where r_{ij} is the distance between oxygen atoms and r_{mn} is the distance between partial charge sites in molecules i and j. The summation for the LJ is over the number of oxygen pairs in the system, with the Coulomb term being over all atoms pairs in the system that are not part of the same molecule This gives a complete description of the intermolecular interactions that can be used in an MD simulation.

2.1.1.2 Bonding interactions

There are multiple different approaches to describing the bonding interactions within a chemical system. An example of this can involve different descriptions of the bonds, bend angles, torsion angles that are usually taken to be harmonic. Many simulation packages have force fields available that involve more terms and parameters to describe the system with many being developed to deal with specific system sizes and some for specific systems. Here we look at one example of how bonding interactions are calculated for the q-TIP4P/F water model. The q-TIP4P/F model is flexible and anharmonic in the O-H stretching mode.

The intramolecular component of this potential is calculated by using a quartic expansion of a Morse potential (shown in Fig 2.2) to describe the stretching of the O-H bonds and a simple harmonic potential for the bond angle,

$$V_{\text{intra}} = \sum_i \left[V_{\text{OH}}(r_{i1}) + V_{\text{OH}}(r_{i2}) + \frac{1}{2} k_\theta (\theta_i - \theta_{eq})^2 \right], \tag{2.8}$$

where

$$V_{\text{OH}}(r) = D_r \left[\alpha_r^2 (r - r_{eq})^2 - \alpha_r^3 (r - r_{eq})^3 + \frac{7}{12} \alpha_r^4 (r - r_{eq})^4 \right]. \tag{2.9}$$

In this potential, r_{i1} and r_{i2} are the two O-H distances and θ is the H-O-H bond angle in the i^{th} water molecule. Eq. (2.9) is different to the standard full Morse potential,

$$V_{\text{OH}}(r) = D_r \left[1 - e^{-\alpha_r (r - r_{eq})} \right]^2, \tag{2.10}$$

as it eliminates dissociation events, which would not be described correctly for this model anyway. The advantage to using a flexible water model is that the anharmonic description of the O-H bonds allow the single broad absorption band seen in the liquid water IR spectrum to be recovered.[21] A contrasting example to this can be seen when examining the q-SPC/Fw[34] water model.

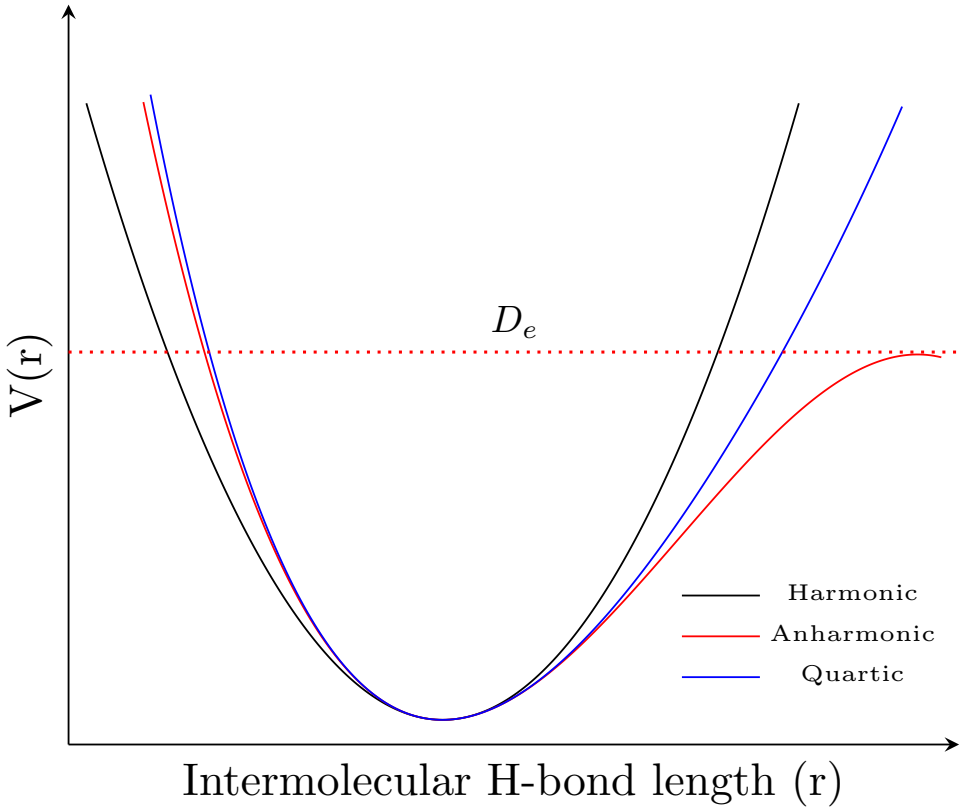

Figure 2.2: Illustration of the individual terms that combine to form the bonding terms in the q-TIP4P/F water model, which is truncated at the quartic term.

This uses a harmonic description of the stretching and bending modes,

$$V_{\mathrm{OH}}(r) = \frac{1}{2} k_r (r - r_{eq})^2. \tag{2.11}$$

which does not give a very good description of the O-H stretching band in the IR spectrum.

The q-TIP4P/F contains nine parameters in total (detailed in Chapter 1) where the intermolecular parameters are fixed to the same corresponding values in a different water potential (TIP4P/2005[38]), and the intramolecular parameters were optimized to give good agreement with experimental structure, diffusion coefficient and vibrational absorption frequencies of the liquid phase in PI simulations.

2.1.2 Time evolution

Now that we have an equation describing the interactions in the system, a full set of forces can be computed for any individual state of the system. We

need a method that can use these forces to evolve the system through a time step Δt, this forms the fundamental basis of an MD simulation. In order for this evolution to take place, equations of motion are required to describe how this takes place. While it is possible to use Newton's equations of motion for a system described by Cartesian coordinates, if one is using any other description of atom positions (e.g. spherical coordinates),these equations of motion are not appropriate. Therefore it is more common to use equations of motion that can be applied to any coordinate system. There are multiple methods of doing this however for this Section we will only focus on one of these, the Hamiltonian formulation.

2.1.2.1 Hamiltonian formulation

We begin with our complete set of $3N$ Cartesian atomic coordinates and conjugate momenta

$$\mathbf{r}^N = (x_1, y_1, z_1, \ldots, x_N, y_N, z_N), \tag{2.12}$$

$$\mathbf{p}^N = (p_{x,1}, p_{y,1}, p_{z,1}, \ldots, p_{x,N}, p_{y,N}, p_{z,N}). \tag{2.13}$$

In terms of Cartesian coordinates the kinetic energy component of the Hamiltonian is given by

$$K = \sum_{i=1}^{N} \frac{\mathbf{p}_i^2}{2m_i}, \tag{2.14}$$

the overall Hamiltonian, defined as the sum $K + V$ is given by

$$H(\mathbf{r}^N, \mathbf{p}^N) = K + V = \sum_{i=1}^{N} \frac{\mathbf{p}_i^2}{2m_i} + V(\mathbf{q}^N). \tag{2.15}$$

The Hamiltonian returns the total energy of the system. In general coordinates we can express the equations of motion as:

$$\frac{\partial \mathbf{p}_i}{\partial t} = -\frac{\partial H}{\partial \mathbf{q}_i} \tag{2.16}$$

$$\frac{\partial \mathbf{q}_i}{\partial t} = \frac{\partial H}{\partial \mathbf{p}_i} \tag{2.17}$$

When using Cartesian coordinates, $\mathbf{q}^N = \mathbf{r}^N$ and it follows that:

$$\frac{\partial \mathbf{p}_i}{\partial t} = -\frac{\partial V}{\partial \mathbf{r}_i}, \tag{2.18}$$

$$\frac{\partial \mathbf{r}_i}{\partial t} = \frac{\partial K}{\partial \mathbf{p}_i}, \tag{2.19}$$

$$\frac{\partial \mathbf{p}_i}{\partial t} = +\mathbf{f}_i, \tag{2.20}$$

$$\frac{\partial \mathbf{r}_i}{\partial t} = \frac{\mathbf{p}_i}{m_i}. \tag{2.21}$$

This gives us the equations of motion that allow us to evolve the system through a time step. The Hamiltonian equations of motion can also be shown to conserve the total Hamiltonian.

$$H(\mathbf{r}(t), \mathbf{p}(t)) = H(\mathbf{r}(0), \mathbf{p}(0)) = E \tag{2.22}$$

$$\begin{aligned} \frac{dH}{dt} &= \sum_{i=1}^{N} \left(\frac{\partial H}{\partial \mathbf{r}_i} \dot{\mathbf{r}}_i + \frac{\partial H}{\partial \mathbf{p}_i} \dot{\mathbf{p}}_i \right) \\ &= \sum_{i=1}^{N} \left(\frac{\partial H}{\partial \mathbf{r}_i} \frac{\partial H}{\partial \mathbf{p}_i} - \frac{\partial H}{\partial \mathbf{p}_i} \frac{\partial H}{\partial \mathbf{r}_i} \right) = 0. \end{aligned} \tag{2.23}$$

2.1.2.2 Velocity-Verlet algorithm

In order to evolve the equations of motion to generate an MD trajectory, a finite difference method is used. This breaks the integration down into smaller steps separated in time by a fixed time step δt. If we know the forces for each atom in the system, we can determine their accelerations, which when combined with the positions and velocities at time t gives the positions and velocities at time $t + \delta t$. During this time step, the forces are assumed to be constant. When the particles are in their new position, the forces can be recalculated, which can then be used to calculate new positions and velocities at time $t+2\delta t$. This can continue for as many time steps as necessary. Multiple algorithms exist that use finite difference methods to integrate the equations of motion, all of these make the assumption that the positions and dynamic properties (acceleration, velocity etc.) can be approximated as an expansion of a Taylor series,

$$\mathbf{r}(t + \delta t) = \mathbf{r}(t) + \delta t \mathbf{p}(t) + \frac{1}{2}\delta t^2 \mathbf{a}(t) + \frac{1}{6}\delta t^3 \mathbf{b}(t) + \frac{1}{24}\delta t^4 \mathbf{c}(t) + \ldots. \tag{2.24}$$

Here $\mathbf{p}$ is the momentum, $\mathbf{a}$ is the acceleration, $\mathbf{b}$ is the third derivative of the position with respect to time and so on. The most widely used algorithm for integrating the equations of motion for a system is the Verlet algorithm.[111,112] This uses the positions and accelerations at the current system time t, as well

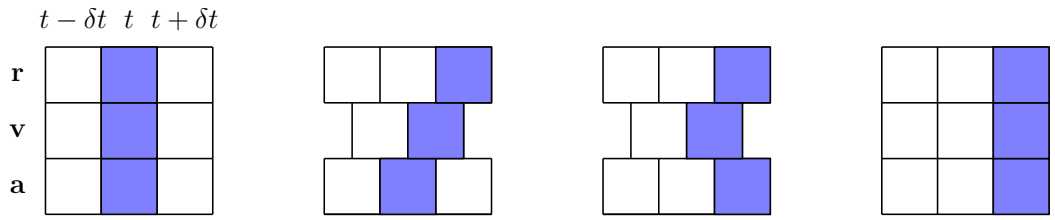

Figure 2.3: Illustration of the three stages of the velocity-Verlet algorithm. Step 1 evolves position to $t+\delta t$ and momentum to $t+\frac{1}{2}\delta t$. Step 2 evolves the acceleration to $t+\delta t$ and step 3 evolves the momentum through another half time step to $t+\delta t$

as the positions from the step preceding it $\mathbf{r}(t-\delta t)$ in order to calculate $\mathbf{r}(t+\delta t)$. The forward step and reverse step can be related to the velocities and positions at time t,

$$\mathbf{r}(t+\delta t) = \mathbf{r}(t) + \delta t\mathbf{p}(t) + \frac{1}{2}\delta t^2\mathbf{a}(t) + \ldots, \tag{2.25}$$

$$\mathbf{r}(t+\delta t) = \mathbf{r}(t) - \delta t\mathbf{p}(t) + \frac{1}{2}\delta t^2\mathbf{a}(t) - \ldots. \tag{2.26}$$

These two equations can be combined giving

$$\mathbf{r}(t+\delta t) = 2\mathbf{r}(t) - \mathbf{r}(t-\delta t) + \delta t^2\mathbf{a}(t). \tag{2.27}$$

The Verlet algorithm does not include velocities however they can be determined by finite difference:

$$\mathbf{p}(t) = \frac{[\mathbf{r}(t+\delta t) - \mathbf{r}(t-\delta t)]}{2\delta t}. \tag{2.28}$$

The requirements for the implementation of the Verlet algorithm are simply two sets of positions $\mathbf{r}(t)$ and $\mathbf{r}(t-\delta t)$ and the acceleration $\mathbf{a}(t)$. The steps of this algorithm are detailed in Fig 2.3. A drawback however is that the positions at $\mathbf{r}(t+\delta t)$ are calculated by adding the term $\delta t^2\mathbf{a}(t)$ to the difference in the larger terms $2\mathbf{r}(t)$ and $\mathbf{r}(t-\delta t)$, which can lead to a loss in precision. Another drawback of the method is because the momenta are not included, they can be difficult to calculate and they are not available until the positions have been computed at the next time step. The method itself is also not able to self start, meaning that because the computation of positions at $t+\delta t$ requires the positions at the current time step as well as the previous time step. Therefore at $t=0$ there is only a single set of positions available and therefore another method is needed in order to obtain the positions at $t-\delta t$ so that the propagation can begin. One method is to use the Taylor series from Eq. (2.24) truncated after the first term, giving $\mathbf{r}(-\delta t) = \mathbf{r}(0) - \delta t\mathbf{p}(0) - \delta t\mathbf{p}(0)$.

These issues can be resolved by using an improved version of the Verlet algorithm, the velocity-Verlet algorithm. This gives the positions, accelerations and momenta at every time step without any loss in precision.

$$\mathbf{r}(t+\delta t) = \mathbf{r}(t) + \delta t \mathbf{p}(t) + \tfrac{1}{2}\delta t^2 \mathbf{a}(t), \tag{2.29}$$

$$\mathbf{p}(t+\delta t) = \mathbf{p}(t) + \tfrac{1}{2}\delta t[\mathbf{a}(t) + \mathbf{a}(t+\delta t)]. \tag{2.30}$$

This algorithm is implemented in three stages because, in order to calculate the new momenta, the accelerations at the current time step t and the next time step $t+\delta t$. In the first step of the algorithm, the positions are calculated at $t+\delta t$ from Eq. (2.29) using the momenta and acceleration at time t. The momenta at time $t+\frac{1}{2}\delta t$ are then computed using:

$$\mathbf{p}(t+\tfrac{1}{2}\delta t) = \mathbf{p}(t) + \tfrac{1}{2}\delta t \mathbf{a}(t). \tag{2.31}$$

The new positions are then used to calculate new forces, which gives the acceleration at $t+\delta t$. In the final step, the new momenta at $t+\delta t$ are calculated by,

$$\mathbf{p}(t+\delta t) = \mathbf{p}(t+\tfrac{1}{2}\delta t) + \tfrac{1}{2}\delta t^2 \mathbf{a}(t+\delta t). \tag{2.32}$$

This total transformation is illustrated in Fig 2.3. Overall the velocity-Verlet algorithm provides a precise way of integrating the equations of motion for a classical system.

2.1.3 Periodic boundary conditions

MD requires boundaries in the simulation of liquids and gases in order to keep the system of interest within interaction range. If not boundaries were present, high temperature simulations of gases would lead to molecules drifting apart and ceasing to interact. As well as this, some simulations may wish to focus on the calculation of 'macroscopic' properties of a system, where boundary conditions and the effects they have on the system are of paramount importance. To expand on this point, consider a standard simulation of water using the q-TIP4P/F model discussed earlier. Due to computational expense it is only feasible to simulate a few thousand water molecules before the cost becomes prohibitive. Therefore we must make the assumption that this number will accurately reflect the bulk properties of the system. However if we consider a real life cube of water with a 1 litre volume, simple maths would tell us there are approximately 3.3×10^{25} molecules present. Based on the diameter

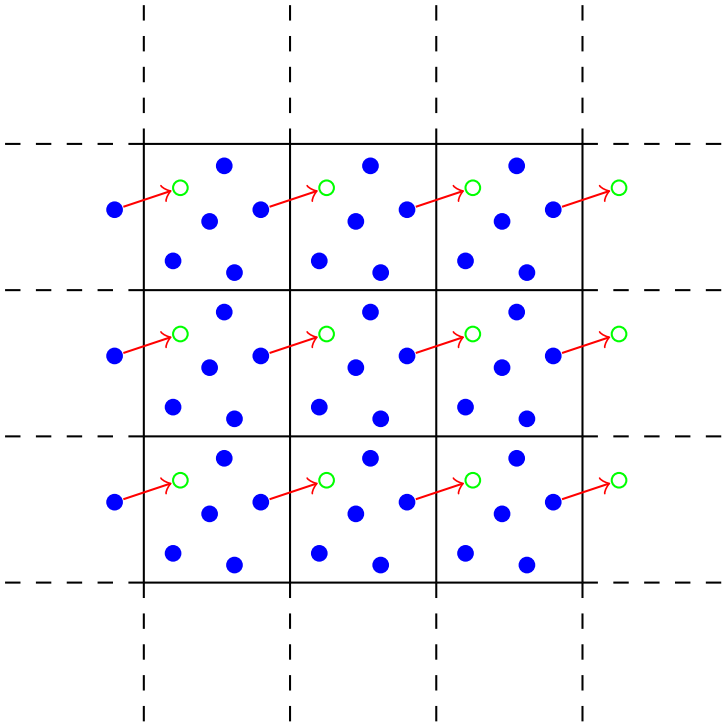

Figure 2.4: Illustration of PBCs in a 2-dimensional grid. A particle is shown leaving the box and entering from the other side to maintain the total number.

of a water molecule and the general approximation that interactions with a boundary extend to 10 molecules into the bulk liquid, the number interacting with the walls in some way is 2×10^{19}. This is roughly 1 molecule for every 1.5 million present in the container. Now consider our simulation of ≈ 2000 water molecules, in this case the vast majority will be influenced by the boundary in some way so would therefore not give a good representation of the 'bulk' properties of water. If one were to remove the boundary altogether there would be no issue with these interactions, however by doing this a majority of molecules would lie on the surface and once again this is not a good way to describe the 'bulk' of the system. We must therefore use a method that can replicate the bulk properties of the system without requiring an infeasible amount of molecules. To do this we use Periodic Boundary Conditionss (PBCs).[54,107–109]

While it is possible to use different shaped containers for periodic boundaries, and indeed this is the case for some of the work carried out in Chapter 4, we only consider the cubic box here. PBCs replicate the cubic box throughout space, so during the course of a simulation, as molecules move though the original box, they move in the same way through the other replicated boxes. Therefore if a molecule should leave the original box, one of the replicas will enter from the opposite site, preserving the total number, this is shown in Fig

2.4. It is not necessary to store the coordinates of all the molecules in the replica boxes, just store the coordinates for the central box, meaning there is no computational cost for introducing these conditions. As molecules are free to move over boundaries, there are no boundary interactions to worry about. The only other concern is to ensure that the length of the simulation box is greater than the cutoff length for the long range interactions of the potential, otherwise the molecules in the box might interact with their replicas in the periodic boxes. By using these conditions the 'bulk' properties of a system can be accurately calculated by only using a few hundred molecules.

2.1.3.1 Ewald sum

When using PBCs in MD simulations, the Ewald sum[54,107–109] is used where a particle interacts with all other particles in the simulation cell as well as all its corresponding images in other periodic cells. The charge-charge contribution for all pairs of charges in the central simulation box can be given as,

$$V(r) = \frac{1}{2}\sum_{i=1}^{N}\sum_{j=1}^{N}\frac{q_i q_j}{4\pi\epsilon_0 r_{ij}}, \tag{2.33}$$

where r_{ij} is the minimum distance between the charges i and j. Directly surrounding the central simulation box there are 6 other boxes at a distance of L from the central box. For a box positioned at a cubic lattice point $\mathbf{n} = (n_x L, n_y L, n_z L)$ with n_x, n_y, n_z being integers,

$$V(r) = \frac{1}{2}\sum_{\mathbf{n}}\sum_{i=1}^{N}\sum_{j=1}^{N}\frac{q_i q_j}{4\pi\epsilon_0|\mathbf{r}_{ij}+\mathbf{n}|}. \tag{2.34}$$

$|\mathbf{n}|$ takes on the values 1, $\sqrt{2}$,... . This can also be written as an expression to include the central box ($—\mathbf{n}— = 0$)

$$V(r) = \frac{1}{2}\sum_{|\mathbf{n}|=0}^{'}\sum_{i=1}^{N}\sum_{j=1}^{N}\frac{q_i q_j}{4\pi\epsilon_0|\mathbf{r}_{ij}+\mathbf{n}|}. \tag{2.35}$$

The prime included on the first summation shows that the interaction $i = j$ for $\mathbf{n} = 0$ is not included. The total contribution is therefore from the central box as well as the interactions between the central box and the surrounding images. The problem with this is that the overall summation in Eq. (2.35) is extremely slow to converge, and also suffers from the problem of conditional convergence, where there are a mix of positive and negative terms present that taken alone form a divergent series (one that does not have a finite sum) and therefore the sum of the series is dependent on the order that the terms

are considered. An additional problem arises with the Coulomb interaction, which has the potential to vary rapidly at short distances.

In order to overcome these issues, the Ewald sum converts the summation into two series which converge more quickly. This can be explained using the identity:

$$\frac{1}{r} = \frac{f(r)}{r} + \frac{1 - f(r)}{r}. \tag{2.36}$$

The choice of $f(r)$ therefore needs to be appropriate to deal with the rapid variation of $1/r$ at short r and the slow decay at long r. The Ewald method considers each charge being surrounded by a neutralising charge distribution of equivalent magnitude but with the opposite sign. A commonly use charge distribution used is Gaussian with the form,

$$p_i(\mathbf{r}) = \frac{q_i \alpha^3}{\pi^{3/2}} exp(-\alpha^2 r^2). \tag{2.37}$$

The sum over the charges has now been converted to a sum of the interactions between the charges with the added neutralising charge distribution. The dual summation of this can be shown as,

$$V(r) = \frac{1}{2} \sum_{i=1}^{N} \sum_{j=1}^{N} \sum_{|\mathbf{n}|=0}{}' \frac{q_i q_j}{4\pi\epsilon_0} \frac{\mathrm{erfc}(\alpha|\mathbf{r}_{ij} + \mathbf{n}|)}{|\mathbf{r}_{ij} + \mathbf{n}|}, \tag{2.38}$$

where erfc is the associated error function,

$$\mathrm{erfc}(x) = \frac{2}{\sqrt{\pi}} \int_x^\infty exp(-t^2) dt. \tag{2.39}$$

In the Ewald sum, the error function (erfc) is used as the function $f(r)$ in Eq. (2.36). This new method of summation converges rapidly and beyond some cutoff distance its value can be considered negligible. How quickly this convergence is achieved depends upon the width of the cancelling Gaussian distributions α. This parameter should be chosen so that the only terms that are part of the series in Eq. (2.38) are those for which $|\mathbf{n}| = 0$, meaning that only pairwise interactions involving the charges in the central box are present, unless a cutoff is used in which case α is chosen so that only interactions with other charges within the cutoff are included. A second charge distribution is now added which completely counteracts the first neutralising distribution, the contribution from this is,

$$V(r) = \frac{1}{2}\sum_{k\neq 0}\sum_{i=1}^{N}\sum_{j=1}^{N}\frac{1}{\pi L^3}\frac{q_i q_j}{4\pi\epsilon_0}\frac{4\pi^2}{k^2}exp\left(-\frac{k^2}{4\alpha^2}\right)\cos(\mathbf{k}\cdot\mathbf{r}_{ij}) \tag{2.40}$$

This second summation is performed in reciprocal space, with the vectors $\mathbf{k}$ being reciprocal given by $\mathbf{k} = 2\pi\mathbf{n}/L$. Just like the summation above, this reciprocal sum also converges much more rapidly than the standard point-charge sum. However the drawback is that the number of terms that must be included increases with α. A balance is therefore needed between the two summations to determine the value of α as the first 'real-space' summation converges quickly for large widths and the second 'reciprocal-space' summation converges quickly with small widths. The reciprocal space summation corresponds to the second term in Eq. (2.36) with the requirement for the term being that it is a slowly varying function for all values of r. The Fourier transform of this can be represented as a small number of reciprocal vectors. As the sum of Gaussian functions in the real space summation includes a self interaction, this must be subtracted at the end of the Ewald sum so that the energy value is not artificially inflated by this effect.

$$V(r) = -\frac{\alpha}{\sqrt{\pi}}\sum_{k=1}^{N}\frac{q_k^2}{4\pi\epsilon_0} \tag{2.41}$$

A final correction term could also be required depending on what surrounds the simulation boxes. In the case where the surroundings have an infinite relative permittivity, then no correction is needed. However if the surroundings are a vacuum, a correction term is required to be added to the energy.

$$V(r)_{\text{corr}} = \frac{2\pi}{3L^3}\left|\sum_{i=1}^{N}\frac{q_i}{4\pi\epsilon_0}\mathbf{r}_i\right|^2 \tag{2.42}$$

The final Ewald summation term can therefore by expressed as

$$V(r) = \frac{1}{2}\sum_{i=1}^{N}\sum_{j=1}^{N}\begin{cases}\sum_{|\mathbf{n}|=0}^{\infty}{}' \frac{q_i q_j}{4\pi\epsilon_0}\frac{\text{erfc}(\alpha|\mathbf{r}_{ij}+\mathbf{n}|)}{|\mathbf{r}_{ij}+\mathbf{n}|} \\ +\sum_{k\neq 0}\frac{1}{\pi L^3}\frac{q_i q_j}{4\pi\epsilon_0}\frac{4\pi^2}{k^2}\exp\left(-\frac{k^2}{4\alpha^2}\right)\cos(\mathbf{k}\cdot\mathbf{r}_{ij}) \\ -\frac{\alpha}{\sqrt{\pi}}\sum_{k=1}^{N}\frac{q_k^2}{4\pi\epsilon_0}+\frac{2\pi}{3L^3}\left|\sum_{i=1}^{N}\frac{q_i}{4\pi\epsilon_0}r_k\right|^2\end{cases} . \tag{2.43}$$

The Ewald sum allows an accurate method of including all the effects of long-

range forces in a computer simulation and has been used in many different applications where electrostatic effects are important including systems with high charge, lipid bilayers and DNA. The Ewald summation does have some drawbacks as it can reinforce issues that arise from the use of PBCs. As an example, the method results in charge-charge interactions being minimised at a distance of half the box length, with instantaneous fluctuations being replicated throughout the entirety of the infinite system instead of being damped out. The Ewald sum is also expensive to implement computationally, the use of a constant α results in scaling of the square of the number of particles in the central cell, a varying α can result in scaling of $N^{3/2}$, however the variation of α may result in the range of the Coulomb potential being incompatible with the range of the van der Waals interactions. One method that can be used to improve the scaling is the use of fast Fourier transform method on the reciprocal space computation, which results in scaling of $N\ln N$ for that part of the summation. In cases where a large value of α is chosen such that the interatomic interaction is negligible for r_{ij} greater than a cutoff value, the real space part of the summation is reduced to order N and therefore the whole Ewald summation can be made to scale as $N\ln N$.

2.1.4 Time-dependent properties

MD simulations evolve through time and as such, time-dependent properties can be computed from the system configurations generated during the simulation. One common time-dependent property calculated is the diffusion coefficient, this is simply the integral of the velocity auto-correlation.[107,109] A general (time independent) correlation function can be defined as

$$C_{xy} = \frac{1}{N}\sum_{i=1}^{N} x_i y_i \equiv \langle x_i y_i \rangle. \tag{2.44}$$

Here there are N values in the data sets x and y. This can then be normalised to give a value between -1 and +1:

$$C_{xy} = \frac{\frac{1}{N}\sum_{i=1}^{N} x_i y_i}{\sqrt{\left(\frac{1}{N}\sum_{i=1}^{N} x_i^2\right)\left(\frac{1}{N}\sum_{i=1}^{N} y_i^2\right)}} = \frac{\langle x_i y_i \rangle}{\sqrt{\langle x_i^2 \rangle \langle y_i^2 \rangle}}. \tag{2.45}$$

This normalisation returns a value of 0 if there is no correlation and a value of positive or negative 1 represents high correlation. A more useful form of

the correlation function can be written

$$C_{xy} = \frac{\sum_{i=1}^{N} x_i y_i - \frac{1}{N}\left(\sum_{i=1}^{N} x_i\right)\left(\sum_{i=1}^{N} y_i\right)}{\sqrt{\left[\sum_{i=1}^{N} x_i^2 - \frac{1}{N}\left(\sum_{i=1}^{N} x_i\right)^2\right]\left[\sum_{i=1}^{N} y_i^2 - \frac{1}{N}\left(\sum_{i=1}^{N} y_i\right)^2\right]}}. \tag{2.46}$$

The form in Eq. 2.46 does not require any mean values of the variables $\langle x \rangle$ and $\langle y \rangle$ to be computed before the correlation function is evaluated. This means the function can be accumulated as the simulation is carried out. An MD simulation can output the x and y variables at each time step, therefore a property at time 0 can be correlated with another at time t, where t is is a time increment over multiple steps. The result of this gives time correlation coefficients. The overall function can then be written as

$$C_{xy}(t) = \langle x(t)y(0) \rangle, \tag{2.47}$$

with the following two relations being useful

$$\lim_{t \to 0} C_{xy}(0) = \langle xy \rangle, \tag{2.48}$$

$$\lim_{t \to \infty} C_{xy}(t) = \langle x \rangle \langle y \rangle. \tag{2.49}$$

There are two instances to consider in these functions, when x and y are the same property and they are different. When the two are different, it is referred to as a cross-correlation function. When the two are the same it is known as an autocorrelation function. Autocorrelation functions are more commonly used and are exclusively used in the work presented hereafter. This type of function describes how well a system retains a 'memory' of its previous state and can show how quickly a system loses its 'memory' of a previous state. An example of this type of function is the velocity autocorrelation function. This shows how velocity at time t is correlated with velocity at time 0. In a system with more than one particle or molecule the function is averaged over the total number in the system, however some correlation functions exist that are a property of the system as a whole (e.g. dipole). The velocity autocorrelation function can be written as

$$C_{vv}(t) = \frac{1}{N} \sum_{i=1}^{N} \mathbf{v}_i(t) \cdot \mathbf{v}_i(0). \tag{2.50}$$

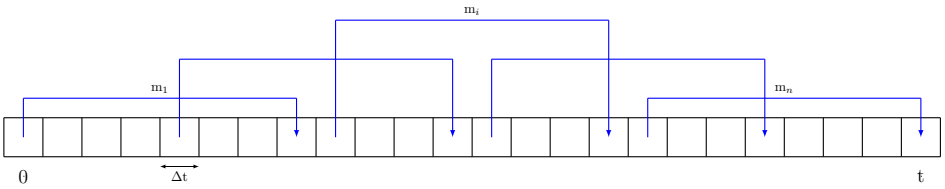

Figure 2.5: Illustration of the calculation of the autocorrelation function using different time origins. Using multiple time origins increases accuracy

We need to normalise the function again as before to provide a scale free measure of the statistical dependence, this can be done by

$$C_{vv}(t) = \frac{1}{N}\sum_{i=1}^{N}\frac{\langle \mathbf{v}_i(t)\cdot\mathbf{v}_i(0)\rangle}{\langle \mathbf{v}_i(0)\cdot\mathbf{v}_i(0)\rangle}. \tag{2.51}$$

For a general system, this function returns a value of 1 at short time and 0 at long times. The time take between the two is generally referred to as the relaxation time. The majority of simulations are run over timescales that are significantly longer than the relaxation time, therefore this function can be sampled multiple times and averaged in order to reduce the error. As an example a simulation with a relaxation time of r and total time t would have $t - r$ non overlapping trajectories over which this function can be calculated. This is illustrated in Fig 2.5. If we use a number of starting points M for these trajectories then we can write,

$$C_{vv}(t) = \frac{1}{MN}\sum_{j=1}^{M}\sum_{i=1}^{N}\mathbf{v}_i(t_j)\cdot\mathbf{v}_i(t_j+t). \tag{2.52}$$

The more trajectories M that can be run, the more accurate the result will be. This number is usually governed by the length of the simulation and the number that can be generated before it becomes cost prohibitive. This means that systems with a shorter relaxation can generally have the correlation function calculated more precisely. The normalised velocity autocorrelation function for liquid water is shown in Fig 2.6, and it can be seen that the relaxation time (i.e when the system has no memory of its state at time $t = 0$ is approximately 1 ps.

While this property is calculated over the particles and number of trajectories, an example of a time dependent property that is calculated over the entire system is the net dipole. This is comprised of the vector sum of the individual dipoles of all the molecules in the system. Naturally this can only

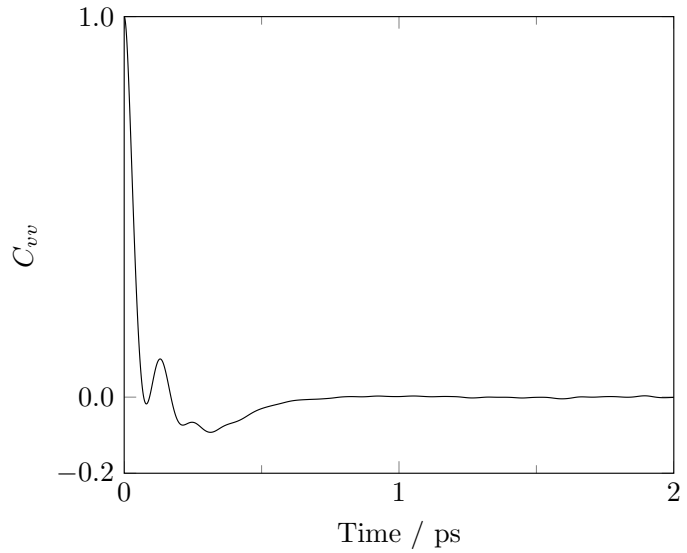

Figure 2.6: Normalised velocity autocorrelation function for liquid water using 50 trajectories of 2 ps. The relaxation time can be seen as approximately 1 ps, where the system no longer retains any correlation with the configuration at time $t = 0$.

be calculated assuming that the molecules in the system have a dipole that is not equal to 0, otherwise there would be no dipole. The magnitude and orientation of the net dipole changes over time and can be calculated by,

$$\boldsymbol{\mu}_{\text{tot}}(t) = \sum_{i=1}^{N} \boldsymbol{\mu}_i(t), \tag{2.53}$$

where $\boldsymbol{\mu}_i(t)$ is the dipole moment of the i^{th} molecule at time t. Each individual contribution to the net dipole is given by,

$$\boldsymbol{\mu}_i = \sum_i q_i \cdot \mathbf{r}_i \tag{2.54}$$

where q_i is the magnitude of the i^{th} charge and $\mathbf{r}_i$ is the vector representing the position of the i^{th} charge. The total correlation function can then be written as

$$C_{\text{dipole}}(t) = \frac{\langle \boldsymbol{\mu}_{\text{tot}}(t) \times \boldsymbol{\mu}_{\text{tot}}(0) \rangle}{\langle \boldsymbol{\mu}_{\text{tot}}(0) \times \boldsymbol{\mu}_{\text{tot}}(0) \rangle}. \tag{2.55}$$

Using this allows the net dipole of any system to be calculated. This can be especially useful as the IR spectrum can be computed using this correlation function. An example of this is shown in Fig 2.7 for the q-TIP4P/F model of liquid water for both anharmonic and harmonic versions. As discussed earlier,

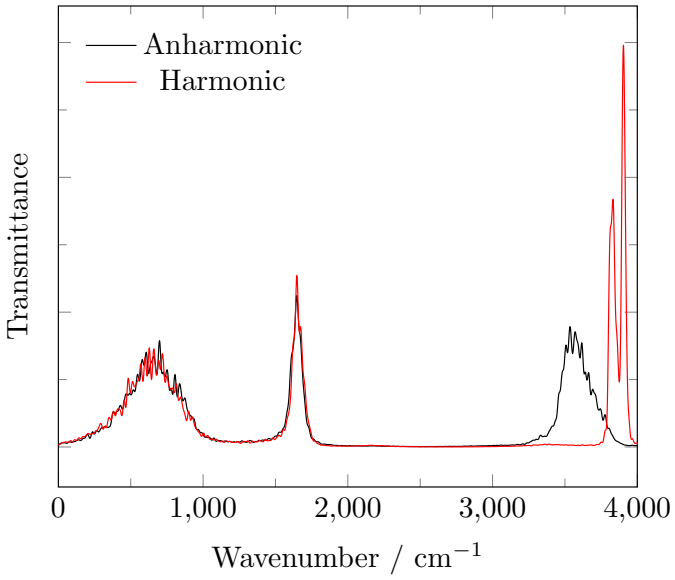

Figure 2.7: Classical anharmonic and harmonic IR spectra of liquid water at 298 K calculated using MD. The broad peak at 3500 cm^{-1} representing the O-H stretching motion is recovered for the anharmonic model, but not the modified harmonic model.

the broad peak at 3500 cm^{-1} is recovered using the standard anharmonic version whereas it is not recovered using the harmonic version, instead the peak is split and shifted to a higher wavenumber.

2.1.5 Ensembles

Running an MD simulation using the potential energy V(**r**), along with PBCs leads us to what is known as a microcanonical ensemble. In this ensemble the system is isolated from changes to the number of moles (N), the volume (V) and energy (E), it is more commonly known as constant-NVE ensemble. As the Hamiltonian conserves energy and there is no outside acting force, there is no way for the energy of the system to change. This ensemble however is not well suited to replicating real-life experiments, where temperature and pressure play a factor. Different ensembles are required to deal with this, two examples of these are the canonical ensemble (constant-NVT), where moles (N), volume (V) and temperature are kept constant (T), and the isothermal-isobaric ensemble (constant-NPT), where number of particles (N), pressure (P) and temperature (T) are kept constant.[54,107–109]

2.1.5.1 Canonical ensemble

The difference between the microcanonical ensemble and the canonical ensemble is the introduction of a target temperature. This is done by allowing the heat exchange processes in the system to be controlled by a thermostat. There are a variety of different methods available to add or remove temperature from the system. Two examples used in our work are the Andersen thermostat[113] and the Parrinello thermostat.[114,115]

The simpler of the two is the Andersen thermostat, where the system is thermally coupled to a fictitious 'heat bath' set at a constant temperature. This is connected through stochastic forces that affect the kinetic energy of molecules within the system. In this thermostat the time between collisions is decided randomly, usually by checking if a random number is above a set threshold value. Between these collisions the system evolves at constant energy. When a collision event occurs, new momenta are sampled from a Boltzmann distribution at the desired temperature for all molecules.

The local Parrinello thermostat[115] contains a correctional Langevin added on to the standard Hamiltonian equation. This correction begins with the correction force used in a Langevin thermostat[108],

$$g_i(t)dt = -\gamma p_i(t)dt + \sqrt{\frac{2m_i\gamma}{\beta}}dW_i(t), \tag{2.56}$$

where β is the inverse temperature, γ is the friction coefficient and $dW_i(t)$ is a vector of the random Brownian motion for each degree of freedom. This is normalised as,

$$\langle \frac{dW_i(t)}{dt}\frac{dW_j(t')}{dt}\rangle = \delta(t-t')\delta_{ij}. \tag{2.57}$$

The speed of thermalization is quantified using the time derivative of the total energy H and can be simplified by taking the kinetic energy component and defining an average kinetic energy $\bar{K} = N_f(2\beta)^{-1}$ and a relaxation time $\tau = (2\gamma)^{-1}$. Exploiting the fact that different degrees of freedom are completely independent of each other we can write,

$$dH(t) = \frac{K(t)-\bar{K}}{\tau}dt + 2\sqrt{\frac{\bar{K}K(t)}{N_f\tau}}dW_i(t). \tag{2.58}$$

This has now reduced the number of noise terms to one, rather than a separate noise term for each degree of freedom. A new correction force is now derived that gives the same thermal properties of the Langevin thermostat but improves by minimizing the disturbance on the trajectory. The procedure

to generate the Parrinello thermostat is the same as the Berendsen thermostat, with a minor difference being a stochastic term being present. Since the correction force acts solely on the momenta, when a value for H is set, the same value must also be set for K. The disturbance to the trajectory is $\sum_i m_i^{-1}(\tilde{g}_i(t)dt)^2$. The minimal disturbance to this for a fixed K increment can be obtained using the correctional force $\tilde{g}_i(t)$, which is proportional to the momentum $p_i(t)$. Therefore $\tilde{g}_i(t) = \lambda(t)p_i(t)$ where $\lambda(t)$ is selected to enforce a set variation of the total energy. This term includes a stochastic part and with the variation of the total energy depending on the momenta, which is only altered through K, the new correction term can be defined as,

$$\tilde{g}_i(t)dt = p_i(t)[A(K(t))dt + B(K(t))dW_i(t)], \tag{2.59}$$

where A and B are functions of the kinetic energy giving a change in the total energy as

$$dH = 2A(K)Kdt + 2B(K)KdW_i + B^2(K)Kdt. \tag{2.60}$$

A and B can be defined by equalizing Eqs (2.47 and 2.49) to give the correction force for the Parrinello thermostat,

$$\tilde{g}_i dt = \frac{1}{2\tau}\left[\left(1 - \frac{1}{N_f}\right)\frac{\bar{K}}{K} - 1\right]p_i dt + \sqrt{\frac{\bar{K}}{N_f K\tau}}p_i dW_i. \tag{2.61}$$

This is a stochastic equation with different noise terms used on all particles. The combination of Eq. (2.61) with the equations of motion exactly samples the canonical ensemble and gives the Parrinello local thermostat that makes improvements over the Langevin form and is significantly better than the Andersen thermostat for sampling the canonical ensemble.

2.1.5.2 Isothermal-isobaric ensemble

The isothermal-isobaric ensemble uses a thermostat just like the canonical ensemble, however a barostat is also introduced in order to maintain a constant pressure. In our work we use a Berendsen barostat[33], this adds an additional term to the equations of motion,

$$\frac{dP}{dt} = \frac{(P_{\text{ext}} - P)}{\tau_P}, \tag{2.62}$$

where P_{ext} is the external pressure, P is the instantaneous pressure and τ_P is a time constant. In this barostat, the sides of the simulation box and the coordinates are rescaled at every step. Assuming an isotropic system the

scaling factor is given by

$$\mu = 1 - \frac{k_T \Delta t}{3\tau_P}(P_{\text{ext}} - P), \tag{2.63}$$

where k_T is the isothermal compressibility. This allows for accurate sampling of the isothermal-isobaric ensemble when coupled with a thermostat. In our work we couple this barostat with the Andersen thermostat or the Parrinello thermostat discussed above.

2.2 Path integral methods

Building upon classical MD, this Section will focus on the imaginary time PI formulation of quantum mechanics. This method allows for exact time-independent properties to be calculated that completely account for NQEs. This is done by exploiting the exact isomorphism between the partition function of a quantum particle and a classical ring polymer.

2.2.1 Imaginary time path integrals

We begin with a one dimensional system containing one particle of mass m. The Hamiltonian operator, $\hat{H}$, for this can be written as,

$$\hat{H} = \frac{\hat{p}^2}{2m} + V(\hat{x}) = \hat{T}(\hat{p}) + \hat{V}(\hat{x}), \tag{2.64}$$

where $\hat{x}$ is the position operator, $\hat{p}$ is the momentum operator and T and V are the respective kinetic and potential energies. While we are only looking at a one dimensional system in this derivation, it can be extended to multiple dimensions.[116] The classical partition function, Z, for a system can be defined as,

$$Z = h^{-1} \int dx \int dp\, e^{-\beta(\frac{p^2}{2m} + V(x))} \tag{2.65}$$

Classically the momentum integral can be performed analytically,

$$Z = h^{-1} \int dx\, e^{-\beta V(x)} \int dp\, e^{-\beta \frac{p^2}{2m}} = \left(\frac{2\pi m}{\beta h^2}\right)^{1/2} \int dx\, e^{-\beta V(x)}. \tag{2.66}$$

The quantum partition function of this system can be defined as the trace over the Boltzmann operator,

$$Z = \mathrm{tr}\left[e^{-\beta\hat{H}}\right], \tag{2.67}$$

with the thermal expectation value of a property of the system using an operator $\hat{A}$ calculated using,

$$\langle A\rangle = \frac{1}{Z}\mathrm{tr}\left[e^{-\beta\hat{H}}\hat{A}\right], \tag{2.68}$$

where 'tr' is a trace and $\beta = 1/k_B t$ where k_B is the Boltzmann constant, and T is the temperature.

When $\hat{A}$ is an operator that depends solely on position, position eigenstates can be introduced as a basis to evaluate the trace,

$$\langle A\rangle = \frac{1}{Z}\int dx_1 \langle x_1|(e^{-\beta_n\hat{H}})^n|x_1\rangle A(x_1), \tag{2.69}$$

where n has been introduced in order to split the matrix element into n imaginary time slices, with $\beta_n = \beta/n$. We can now use the identity operator in order to introduce $(n-1)$ full sets of position eigenstates between each of the newly introduced n terms,

$$\hat{1} = \int dx_i |x_i\rangle\langle x_i|, \tag{2.70}$$

$$\langle A\rangle = \frac{1}{Z}\int dx_1 \ldots \int dx_n \langle x_1|e^{-\beta_n\hat{H}}|x_2\rangle \ldots \langle x_n|e^{-\beta_n\hat{H}}|x_1\rangle A(x_1). \tag{2.71}$$

We can continue this evaluation by using a symmetric Trotter splitting[117],

$$e^{-\beta_n\hat{H}} = e^{-\beta_n[T(\hat{p})+V(\hat{x})]} \simeq e^{-\beta_n V(\hat{x})/2}e^{-\beta_n T(\hat{p})}e^{-\beta_n V(\hat{x})/2} + O(\beta_n^3), \tag{2.72}$$

which can be seen to introduce an error term $O(\beta_n^3)$. This error highlights the importance of splitting the matrix element into n imaginary time slices. If we had continued without doing this, the error term would destroy the quantum result and lead back to the classical partition function as the potential energy and kinetic energy operators do not commute. However with the introduction of n imaginary time slices, the method becomes exact as $n \to \infty$, and for a finite n this error decreases as $1/n^3$. The result of the Trotter splitting allows the matrix elements in Eq. (2.71) to be evaluated, leading to,

$$\langle x|e^{-\beta_n V(\hat{x})/2}e^{-\beta_n T(\hat{p})}e^{-\beta_n V(\hat{x})/2}|x'\rangle = e^{-\beta_n[V(x)+V(x')]/2}\langle x|e^{-\beta_n T(\hat{p})}|x'\rangle. \tag{2.73}$$

From this, the thermal expectation value of an operator that is only position dependent ($\hat{A}$) can be shown as,

$$\langle A\rangle = \frac{1}{Z}\lim_{n\to\infty}\int dx_1 \ldots \int dx_n\, e^{-\beta_n \sum_{k=1}^{n} v(x_k)}\langle x_1|e^{-\beta_n T(\hat{p})}|x_2\rangle \ldots \langle x_n|e^{-\beta_n T(\hat{p})}|x_1\rangle A(x_1). \tag{2.74}$$

Now that we have finished introducing position in order to solve the potential energy matrix elements, we need to solve the kinetic energy matrix elements. This can be done by inserting a complete set of momentum states,

$$\langle x|e^{-\beta_n T(\hat{p})}|x'\rangle = \int dp \langle x|e^{-\beta_n T(\hat{p})}|p\rangle\langle p|x'\rangle = \int dp \langle x|p\rangle e^{-\beta_n p^2/2m}\langle p|x'\rangle. \tag{2.75}$$

The integral can now be evaluated in the momentum representation starting from a momentum eigenstate

$$\hat{p}|p\rangle = p|p\rangle, \tag{2.76}$$

as we also have position, we need to evaluate the overlap between the position and momentum. We begin by multiplying both sides by $\langle x|$ to give a first order differential equation

$$\langle x|\hat{p}|p\rangle = -i\hbar\frac{\partial\langle x|p\rangle}{\partial x} = p\langle x|p\rangle, \tag{2.77}$$

solving for the overlap gives,

$$\langle x|p\rangle = Ne^{ipx/\hbar}, \tag{2.78}$$

where N is a normalisation constant that can be determined by using the delta function normalisation condition[117]

$$\langle p|p'\rangle = \delta(p-p') = \int dx \langle p|x\rangle\langle x|p'\rangle, \tag{2.79}$$

which gives,

$$\langle x|p\rangle = \sqrt{\frac{1}{2\pi\hbar}}\, e^{-ipx/\hbar}. \tag{2.80}$$

Now that the overlap has been solved it can be inserted directly into Eq. (2.75),

$$\langle x|e^{-\beta_n T(\hat{p})}|x'\rangle = \frac{1}{2\pi\hbar}\int dp\, e^{-\beta_n p^2/2m} e^{+ip(x-x')/\hbar}. \tag{2.81}$$

This is a Gaussian integral which can easily be performed to give,

$$\langle x|e^{-\beta_n T(\hat{p})}|x'\rangle = \left(\frac{m}{2\pi\beta_n\hbar^2}\right)^{1/2} e^{-\beta_n m w_n^2 (x-x')^2/2}, \tag{2.82}$$

where $w_n = 1/\beta_n\hbar$. We can now take this result and insert it into the thermal expectation expression in Eq. (2.74),

$$\langle A\rangle = \frac{1}{Z}\lim_{n\to\infty}\left(\frac{m}{2\pi\beta_n\hbar^2}\right)^{n/2}\int dx_1\ldots\int dx_n\, e^{-\beta_n\sum_{k=1}^{n}[mw_n^2(x_k-x_{k+1})^2/2+V(x_k)]}A(x_1). \tag{2.83}$$

This is an expression allowing the thermal expectation value of an observable A to be calculated. This derivation has only taken into account one dimension however it can be expanded to any classical problem in an n dimensional phase space. At this point it would appear that there is one major computational drawback to this method, as the $n\to\infty$ term is difficult to evaluate. However when implementing this method, only a finite number of n imaginary time slices are required in order to achieve convergence of observables to within an acceptable margin of error. What remains is to identify what number of n time slices are required in order to converge different observables, this will be briefly discussed in a later Section.

It can be seen from the trace in the above derivation (Eq. (2.68)) that when we have n time slices, the path begins and ends on the same slice (x_1) and therefore $x_{n+1}\equiv x_1$. From this it is apparent that the imaginary path is circular and isomorphic to a classical ring polymer consisting of n beads that are linked by harmonic springs. Only adjacent beads are connected in this representation and there are no other connections between beads, as illustrated in Fig 2.8. These harmonic springs have a force constant mw_n^2 and each bead has a temperature n times higher than the physical temperature of the system as it evolves in the external potential $V(x_k)$.

$$\beta_n = 1/k_B T_{bead}, \tag{2.84}$$

where

$$T_{bead} = nT, \tag{2.85}$$

is the temperature of each bead. This means that each bead can access parts of space that would otherwise be inaccessible to classical particles, with the result of this being that NQEs such as ZPE and tunnelling are exactly accounted for.

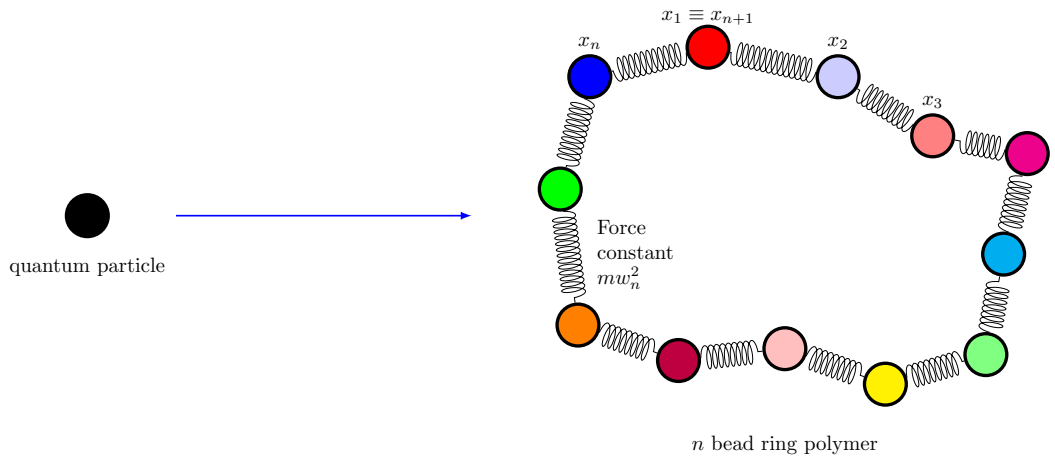

Figure 2.8: Illustration of the isomorphism between a quantum particle and a classical ring polymer. Each bead is connected to adjacent beads using harmonic springs with a force constant mw_n^2.

Another thing to note about the circular nature of the PI approach is that the result obtained is invariant to relabelling the beads. Therefore any property of interest can be acquired by averaging over the n beads. Eq. (2.74) can be rewritten as,

$$\langle A \rangle = \frac{1}{Z} \lim_{n\to\infty} \left(\frac{m}{2\pi\beta_n\hbar^2} \right)^{n/2} \int d^n\mathbf{x}\, e^{-\beta_n \sum_{k=1}^{n} [mw_n^2 (x_k - x_{k+1})^2/2 + V(x_k)]} A_n(\mathbf{x}), \tag{2.86}$$

where we have introduced a new notation $\mathbf{x} = (x_1, \ldots, x_n)^T$ and are now averaging our observable over all n beads of the ring polymer

$$A_n = \frac{1}{n} \sum_{k=1}^{n} A(x_k). \tag{2.87}$$

This same procedure can be applied to the partition function Z to obtain a PI expression containing n beads,

$$Z = \lim_{n\to\infty} Z_n, \tag{2.88}$$

where

$$Z_n = \left(\frac{m}{2\pi\beta_n\hbar^2} \right)^{n/2} \int d^n\mathbf{x}\, e^{-\beta_n \sum_{k=1}^{n} [mw_n^2 (x_k - x_{k+1})^2/2 + V(x_k)]}. \tag{2.89}$$

Eqs. (2.86) and (2.89) can now be sampled using a method such as MC[54], which is known as the Path Integral Monte Carlo (PIMC) method.[118]

One might make an argument that were the beads in the ring polymer independent, the efficiency of the method would significantly increase as the standard error would decrease by a factor of $\sqrt{n}$. However this is not observed due to the spring terms between beads keeping the spatial separation small. When there is no potential acting on the ring polymer, neighbouring beads in the ring polymer are arranged by

$$e^{-\beta_n m w_n^2 (x_k - x_{k+1})^2/2}, \tag{2.90}$$

from this the root mean square distance between adjacent beads is,

$$\langle (x_k - x_{k+1})^2 \rangle^{1/2} = \sqrt{\frac{1}{\beta_n m w_n^2}} = \sqrt{\frac{\beta \hbar^2}{nm}}. \tag{2.91}$$

From this it can be seen that the distance between beads decreases as the number of beads, the particle mass or the temperature is increased. Therefore the properties that are calculated on adjacent beads are highly correlated. The correlation in the forces and energy are key to our new approach to accelerate PI simulations discussed in Chapter 3.

The radius of gyration is another scale that can be quantified within the ring polymer, it describes the spread of the beads from the centre of mass. Here the squared radius of gyration in one dimension is,

$$x_G^2 = \frac{1}{n} \sum_{k=1}^{n} |x_k - x_c|^2, \tag{2.92}$$

where x_c is the position of the centroid,

$$x_c = \frac{1}{n} \sum_{k=1}^{n} x_k. \tag{2.93}$$

The thermally averaged squared radius of gyration can be calculated exactly by,

$$\langle x_G^2 \rangle = \frac{1}{n} \sum_{k=1}^{n} \langle (x_k - x_c)^2 \rangle = \frac{1}{n} \sum_{k=1}^{n} (\langle x_k^2 \rangle - \langle x_c^2 \rangle), \tag{2.94}$$

where the angular brackets define the thermal average from Eqs. (2.86) and (2.89),

$$\langle \ldots \rangle = \frac{\int d^n \mathbf{x}\, e^{-\beta_n \sum_{k=1}^{n} [m w_n^2 (x_k - x_{k+1})^2/2]} (\ldots)}{\int d^n \mathbf{x}\, e^{-\beta_n \sum_{k=1}^{n} [m w_n^2 (x_k - x_{k+1})^2/2]}}. \tag{2.95}$$

The integrals in Eq. (2.95) can be analytically performed using a transforma-

tion to normal mode coordinates. The result of this gives the squared radius of gyration in one dimension as[119]

$$\langle x_G^2 \rangle = \frac{\beta\hbar^2}{12m}\left(1 - \frac{1}{n^2}\right), \tag{2.96}$$

with three dimensions given as

$$\langle r_G^2 \rangle = \langle x_G^2 + y_G^2 + z_G^2 \rangle = 3\langle x_G^2 \rangle = \frac{\beta\hbar^2}{4m}\left(1 - \frac{1}{n^2}\right). \tag{2.97}$$

This derivation is for a free ring polymer however the value obtained is similar to values from condensed phase simulations. The root mean square distance between adjacent beads tends to zero as $n \to \infty$. Despite this, the radius of gyration converges at a finite value.

2.2.2 Path integrals at the classical limit

When a ring polymer reaches the classical limit ($\beta \to 0$), all the beads contract to the centroid and the radius of gyration tends to zero. Once all the beads are located at the centroid, a potential evaluation can be done on the centroid alone,

$$\lim_{\beta\to 0}\left(\sum_{k=1}^{n} V(x_k)\right) = nV(x_c). \tag{2.98}$$

We can now insert this into Eq. (2.89) and transform to a normal mode representation,

$$\lim_{\beta\to 0} Z_n = \left(\frac{m}{2\pi\beta_n\hbar^2}\right)^{n/2}\left[\prod_{l=1}^{n-1}\int d\tilde{x}_l e^{-\beta_n m\Omega_l^2\tilde{x}_l^2/2}\right]\int d\tilde{x}_n\, e^{-\beta V(\tilde{x}_n/\sqrt{n})}. \tag{2.99}$$

As we now have a potential that is only evaluated at the centroid, we can uncouple high frequency normal modes from the external potential,

$$\lim_{\beta\to 0} Z_n = \left(\frac{m}{2\pi\beta_n\hbar^2}\right)^{n/2}\left[\prod_{l=1}^{n-1}\left(\frac{2\pi}{\beta_n m\Omega_l^2}\right)^{1/2}\right]\int d\tilde{x}_n\, e^{-\beta V(\tilde{x}_n/\sqrt{n})}. \tag{2.100}$$

We can rearrange and use an identity,

$$\prod_{l=1}^{n-1}\frac{1}{2\sin(l\pi/n)} \equiv \frac{1}{n}, \tag{2.101}$$

which gives,

$$\lim_{\beta\to 0} Z_n = \left(\frac{m}{2\pi\beta_n\hbar^2}\right)^{1/2} \int d\tilde{x}_n \, e^{-\beta V(\tilde{x}_n/\sqrt{n})}. \tag{2.102}$$

Now we transform back to Cartesian coordinates to give the classical limit of Eq. (2.89),

$$\lim_{\beta\to 0} Z_n = \left(\frac{m}{2\pi\beta_n\hbar^2}\right)^{1/2} \int dx_c \, e^{-\beta V(x_c)}, \tag{2.103}$$

which is the same as the classical partition function for a particle with mass m in a potential $V(x)$[120],

$$Z_{cl} = \left(\frac{m}{2\pi\beta_n\hbar^2}\right)^{1/2} \int dx \, e^{-\beta V(x)}. \tag{2.104}$$

This leads us to the conclusion that the centroid can be considered as the "classical" coordinate of the ring polymer. This forms the basis of the CMD method and relies on the evolution of the ring polymer centroid. The classical partition function in Eq. (2.104) is also recovered when $n = 1$ in Eq. (2.89) at any value of β. This means that a standard classical simulation is the same as performing a PI simulation using only one bead. When more than one bead is used in a PI calculation one can imagine it is the same as the corresponding classical simulation in an extended n bead phase space. This means that all the advances that have been made to improve classical simulations can be applied directly to the PI method.[54,108] Additionally the size of the extended phase space can be used as a very good indicator of the complexity of the quantum PI calculation. The PI simulation is typically around n times more computationally expensive than the corresponding classical simulation where n is the number of ring polymer beads.

The number of ring polymer beads required for convergence is generally accepted to be,

$$n > \beta\hbar\omega_{max}, \tag{2.105}$$

where ω_{max} is the highest frequency in the system. This ensures that the thermal energy available to the ring polymer beads from T_{bead} (the effective temperature from Eq. 2.85) is larger than the energy level spacings.

$$k_B T_{bead} > \hbar\omega_{max}. \tag{2.106}$$

In the case of liquid water the typical number of ring polymer beads required

to converge properties is $n = 32$ at 298 K, although some (like heat capacity) require more. For certain systems the number of beads required can become prohibitive as the computational expense increases. This problem is addressed in Chapter 3 where a new method is introduced that allows a smaller number of beads to be used while still obtaining complete convergence.

2.2.3 Path integral molecular dynamics

If one wishes to look at any dynamic properties such as diffusion a method is required that includes dynamics. This can be done by introducing a set of momenta for the beads and forms the basis of PIMD method.[121] We introduce momenta by using the identity.

$$1 = \left(\frac{\beta_n}{2\pi}\right)^{n/2} \left(\frac{1}{\det[\mathbf{M}]}\right)^{1/2} \int d^n\mathbf{p}\, e^{-\beta_n \frac{1}{2}\mathbf{p}^T\mathbf{M}\mathbf{p}}, \tag{2.107}$$

where 'det' is the determinant of the mass matrix ($\mathbf{M}$), which is assumed to be real symmetric and positive definite so the above integral is well defined.[122] $\mathbf{p}$ contains the bead momenta identical to to the vector notation introduced earlier $\mathbf{p} = (p_1, \ldots, p_n)^T$.

Inserting the identity into Eq. (2.86) gives a new expectation value,

$$\langle A \rangle = \frac{1}{Z} \lim_{n\to\infty} \frac{1}{(2\pi\hbar)^n} \left(\frac{m^n}{\det[\mathbf{M}]}\right)^{1/2} \int d^n\mathbf{p} \int d^n\mathbf{x}\, e^{-\beta_n H_n(\mathbf{p},\mathbf{x})} A_n(\mathbf{x}), \tag{2.108}$$

with

$$H_n(\mathbf{p},\mathbf{x}) = \frac{1}{2}\mathbf{p}^T\mathbf{M}^{-1}\mathbf{p} + \sum_{k=1}^{n} \left(\frac{m\omega_n^2}{2}(x_k - x_{k+1})^2 + V(x_k)\right). \tag{2.109}$$

An equivalent vector notation can be shown as,

$$H_n(\mathbf{p},\mathbf{x}) = \frac{1}{2}\mathbf{p}^T\mathbf{M}^{-1}\mathbf{p} + \frac{1}{2}\mathbf{x}^T\mathbf{K}\mathbf{x} + \sum_{k=1}^{n} V(x_k), \tag{2.110}$$

where $\mathbf{K}$ is the force constant matrix with elements[122],

$$K_{kk'} = m\omega_n^2(2\delta_{k,k'} - \delta_{k,k'-1} - \delta_{k,k'+1} - \delta_{k,1}\delta_{k',n} - \delta_{k,n}\delta_{k',1}). \tag{2.111}$$

Using this in Eq. (2.89), the partition function can be written as,

$$Z = \lim_{n\to\infty} Z_n, \tag{2.112}$$

with,

$$Z_n = \frac{1}{(2\pi\hbar)^n}\left(\frac{m^n}{\det[\mathbf{M}]}\right)^{1/2}\int d^n\mathbf{p}\int d^n\mathbf{x}\, e^{-\beta_n H_n(\mathbf{p},\mathbf{x})}. \tag{2.113}$$

Both Eqs (2.108) and (2.113) will give the exact classical result when $n = 1$ as long as the mass matrix is chosen such that $\det[\mathbf{M}] = m^n$. The ring polymer can be evolved using the classical equations of motion generated from Eq. (2.110),

$$\frac{d\mathbf{p}}{dt} = -\frac{\partial H_n(\mathbf{p},\mathbf{x})}{\partial \mathbf{x}} = -\mathbf{K}\mathbf{x} - \mathbf{b}(\mathbf{x}), \tag{2.114}$$

$$\frac{d\mathbf{x}}{dt} = -\frac{\partial H_n(\mathbf{p},\mathbf{x})}{\partial \mathbf{p}} = +\mathbf{M}^{-1}\mathbf{p}, \tag{2.115}$$

where the vector $\mathbf{b}(\mathbf{x})$ is comprised of the gradients of the external potential,

$$b_k = \frac{\partial V(x_k)}{\partial x_k}. \tag{2.116}$$

Observables can now be calculated by averaging over the time evolved coordinates generated by these equations as the dynamics from Eqs. (2.114) and (2.115) conserve the ring polymer Hamiltonian and the phase space volume.[121] In this form, the trajectories are NVE (constant particle number, volume and energy), however in practical terms experiments are performed at a constant temperature, so an NVT (constant particle number, volume and temperature) ensemble is preferred. As discussed earlier, a thermostat is needed to redistribute energy between the different modes of the system, with a variety of thermostats available.[123]

2.2.4 Ring polymer molecular dynamics

The use of PIMD to evaluate Eq. (2.86) with a suitable amount of reference beads allows the exact calculation of static time independent properties such as thermally averaged potential energy in the $n \to \infty$ limit. However there are properties that require knowledge of the dynamics of the system such as diffusion coefficient and infra-red absorption spectra.[120,124] Linear response theory allows non-equilibrium properties like this to be related to equilibrium time-correlation functions. An example of this, discussed in a later Chapter, is the calculation of the diffusion coefficient, which can be calculated from the velocity autocorrelation function.

The time correlation function for a quantum system with operators $\hat{A}$ and $\hat{B}$ is given by,

$$c_{AB}(t) = \frac{1}{Z}\mathrm{tr}\left[e^{-\beta\hat{H}}\hat{A}e^{+i\hat{H}t/\hbar}\hat{B}e^{-i\hat{H}t/\hbar}\right] = \langle A(0)B(t)\rangle, \tag{2.117}$$

where the angular brackets represent a thermal average. An exact expression can be derived using PI methods which can then be used to evaluate Eq. (2.117)

$$\beta \to it/\hbar. \tag{2.118}$$

However there is a drawback associated with this as the resulting integrands are highly oscillatory. This means that methods like MC have an error that grows exponentially over time if attempting direct evolution. The inability to exactly obtain long time dynamics for systems with many degrees of freedom has led to the developments of methods that can provide approximations to the time correlation functions to give the time-dependent quantum properties. One type of method that accomplishes this is based on evolving the ring polymers using classical mechanics. The RPMD method accomplishes this and is centred on the evolution of the individual ring polymer beads. This is shown in Fig 2.9.

RPMD expands on the existing method of PIMD and assumes that the ring polymers can be evolved classically using Eqs. (2.114) and (2.115) and the resulting trajectories used to give an approximation to time correlation functions.

Within RPMD, a time correlation function can be defined as

$$c_{AB}^{PIMD}(t) \simeq \frac{1}{Z_n}\frac{1}{(2\pi\hbar)^n}\left(\frac{m^n}{\det[\mathbf{M}]}\right)^{1/2}\int d^n\mathbf{p}\int d^n\mathbf{x}e^{-\beta_n H_n(\mathbf{p},\mathbf{x})}A_n(\mathbf{x})B_n(\mathbf{x}_t), \tag{2.119}$$

where $\mathbf{x}_t$ and $\mathbf{p}_t$ are time evolved coordinates and momenta respectively. These are obtained from the classical evolution of the ring polymer from Eqs. (2.114) and (2.115). A_n and B_n are defined in Eq. (2.87). The correlation function in Eq. (2.117) is one of a series of correlation functions,

$$c_{AB}^{\lambda}(t) = \frac{1}{\beta Z}\mathrm{tr}\left[e^{-(\beta-\lambda)\hat{H}}\hat{A}e^{-\lambda\hat{H}}e^{+i\hat{H}t/\hbar}\hat{B}e^{-i\hat{H}t/\hbar}\right], \tag{2.120}$$

with $0 \leq \lambda \leq \beta$, which all reduce to an identical function when treated classically. RPMD provides an approximation to the canonical correlation function (shown in Fig 2.9), also known as Kubo transformed,

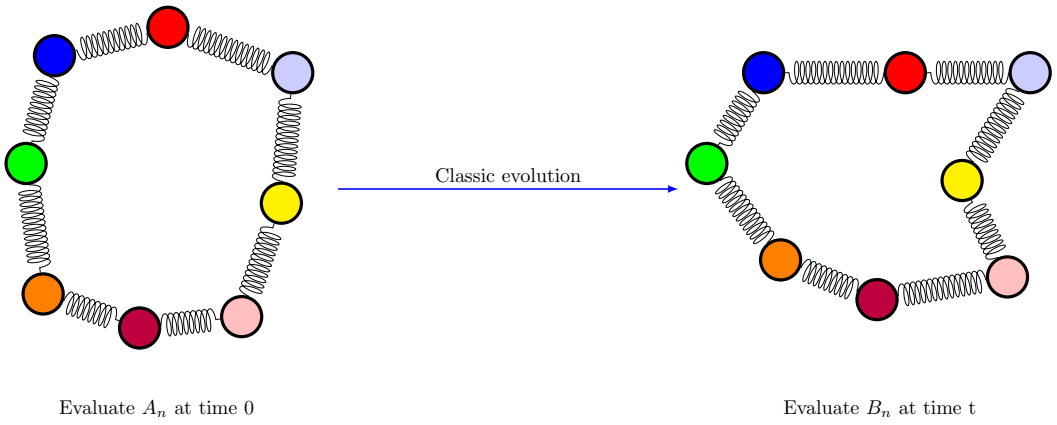

Figure 2.9: Illustration of the approximation of the canonical quantum time correlation function in RPMD.

$$\tilde{c}_{AB}(t) = \frac{1}{\beta Z}\int_0^\beta d\lambda \,\mathrm{tr}\left[e^{-(\beta-\lambda)\hat{H}}\hat{A}e^{-\lambda\hat{H}}e^{+i\hat{H}t/\hbar}\hat{B}e^{-i\hat{H}t/\hbar}\right] = \frac{1}{\beta}\int_0^\beta d\lambda\langle A(-i\lambda\hbar)B(t)\rangle, \tag{2.121}$$

which averages over the $c^{\lambda}_{AB}(t)$ correlation functions. The choice of the canonical function is that it shares the same symmetries as its classical counterpart. Therefore by evolving the ring polymer classically, this symmetry is shared by the approximation to the exact function in Eq. (2.119). Assuming that $\hat{A}$ and $\hat{B}$ are both Hermitian operators, the symmetries of $\tilde{c}_{AB}(t)$ can be shown as

$$\tilde{c}_{AB}(t) = \tilde{c}_{BA}(-t), \tag{2.122}$$

$$\tilde{c}_{AB}(t) = \tilde{c}_{AB}(t)^*, \tag{2.123}$$

$$\tilde{c}_{AB}(t) = \tilde{c}_{AB}(-t)^*, \tag{2.124}$$

showing that it is a real and even function of time.[125] The classical dynamics generated using the equations of motion in Eqs. (2.114) and (2.115) also share this symmetry. The symmetry in Eq. (2.122) results from the use of the Liouville theorem and the use of classical dynamics, Eq. (2.123) follows from the fact that the approximate correlation function in Eq. (2.119) is simply a classical correlation function in extended phase space. The third symmetry Eq. (2.124) is simply due to the fact that classical mechanics is time reversible.[125] As long as a mass matrix is chosen so that the momentum integrals are well defined, these symmetries will be accurately obtained. This also ensures that the correlation function in Eq. (2.119) gives the exact quantum correlation function Eq. (2.121) when $t = 0$,

$$c_{AB}^{PIMD}(0) = \tilde{c}_{AB}(0) = \frac{1}{z_n}\frac{1}{(2\pi\hbar)^n}\left(\frac{m^n}{\det[\mathbf{M}]}\right)^{1/2}\int d^n\mathbf{p}\int d^n\mathbf{x}e^{-\beta_n H_n(\mathbf{p},\mathbf{x})}A_n(\mathbf{x})B_n(\mathbf{x}). \tag{2.125}$$

This then simplifies to that of a static property which is accounted for exactly by PIMD. The standard quantum mechanical correlation function from Eq. (2.117) can be calculated exactly as long as the exact canonical correlation function is known (Eq. (2.121)). This is accomplished by using the Fourier transforms of each function[125],

$$g_{AB}(\omega) = \frac{\beta\hbar\omega}{(1-e^{-\beta\hbar\omega})}\tilde{g}_{AB}(\omega), \tag{2.126}$$

where $\tilde{g}_{AB}(\omega)$ is the Fourier transform of the canonical correlation function,

$$\tilde{g}_{AB}(\omega) = \int_{-\infty}^{+\infty} dt\, e^{-i\omega t}\tilde{c}_{AB}(t), \tag{2.127}$$

and $g_{AB}(\omega)$ is the standard correlation function.

All that remains is the choice of a suitable mass matrix. There exist multiple approximations that comply with the symmetry requirements of Eqs. (2.122, 2.123 and 2.124) as well as being exact as $t \to 0$. However this changes when the restriction is applied that states that the correlation function in Eq. (2.119) should be exact in the classical limit. This choice of matrix is one where the physical mass of the particle m is equivalent to the centroid mass. This forms the basis of the CMD method discussed later, however this is not the only choice of matrix that can be made. RPMD assumes that by looking at the short time expansion of the exact canonical correlation function, one can choose a mass matrix that obtains the best short time accuracy in Eq. (2.119)[122],

$$\mathbf{M} = m\mathbf{I}, \tag{2.128}$$

where $\mathbf{I}$ is the identity matrix and m is the mass of the particle. This forms the basis of the RPMD approach and and is defined by combining Eq. (2.119) with the mass matrix choice in Eq. (2.128), giving a leading order error in the approximation of the correlation function of $O(t^8)$.

From this derivation it can be seen that the trajectories produced by the RPMD method can be used to approximate the canonical time correlation function to a good level of accuracy. However this does not mean it can be directly applied to velocity dependent operators such as the velocity auto-correlation function, which can be used to obtain diffusion coefficients. This

requires taking the second derivative of the correlation function and using a time evolution of the position operator in the Heisenberg form,

$$\frac{d\hat{x}}{dt} = \frac{i}{\hbar}\left[\hat{H}, \hat{x}\right]. \tag{2.129}$$

From this the velocity auto-correlation function can be written as[47],

$$\tilde{c}_{vv}(t) = -\frac{d^2\tilde{c}_{xx}(t)}{dt^2}. \tag{2.130}$$

The RPMD expression for $\tilde{c}_{vv}(t)$ can be obtained like before, by taking the RPMD approximation to $\tilde{c}_{xx}(t)$,

$$c_{xx}^{RPMD}(t) = \frac{1}{Z_n}\frac{1}{(2\pi\hbar)^n}\int d^n\mathbf{p}\int d^n\mathbf{x}e^{-\beta_n H_n(\mathbf{p},\mathbf{x})}\left(\frac{1}{n}\sum_{k=1}^{n}x_k(0)\right)\left(\frac{1}{n}\sum_{k=1}^{n}x_k(t)\right). \tag{2.131}$$

Taking the negative of the second derivative with respect to time gives[47],

$$c_{vv}^{RPMD}(t) = \frac{1}{Z_n}\frac{1}{(2\pi\hbar)^n}\int d^n\mathbf{p}\int d^n\mathbf{x}e^{-\beta_n H_n(\mathbf{p},\mathbf{x})}\left(\frac{1}{n}\sum_{k=1}^{n}\frac{p_k(0)}{m}\right)\left(\frac{1}{n}\sum_{k=1}^{n}\frac{p_k(t)}{m}\right), \tag{2.132}$$

where $p_k(t)$ is the momentum of bead k at time t obtained from the equations of motion. The velocity autocorrelation function requires the second derivative of the position and therefore the error in RPMD is reduced to $O(t^6)$ in this case.

So far the derivation of RPMD has been limited to one dimension. However it can easily be applied to a system containing many dimensions. In a multi dimensional system containing N particles there are three dimensional vectors for position $\mathbf{r}_i = (x_i, y_i, z_i)^T$ and momentum $\mathbf{p}_i = (px_i, py_i, pz_i)^T$, with $V(\mathbf{r}_1, ..., \mathbf{r}_N)$ as the potential energy. The RPMD approximation to the correlation function for the position dependent operators $A(\mathbf{r})$ and $B(\mathbf{r})$ for the Hamiltonian can be shown as[44,47],

$$\tilde{c}_{AB}(t) \simeq \frac{1}{(2\pi\hbar)^{3Nn}Z_n}\int d^{3Nn}\mathbf{p}\int d^{3Nn}\mathbf{r}\, e^{-\beta_n H_n(\mathbf{p},\mathbf{r})}A_n(\mathbf{r})B_n(\mathbf{r}_t), \tag{2.133}$$

where

$$Z_n = \frac{1}{(2\pi\hbar)^{3Nn}}\int d^{3Nn}\mathbf{p}\int d^{3Nn}\mathbf{r}\, e^{-\beta_n H_n(\mathbf{p},\mathbf{r})}, \tag{2.134}$$

and $\beta_n = \beta/n$. $H_n(\mathbf{p},\mathbf{r})$ is the classic Hamiltonian of the N particle n bead ring polymer acting on each bead.[126]

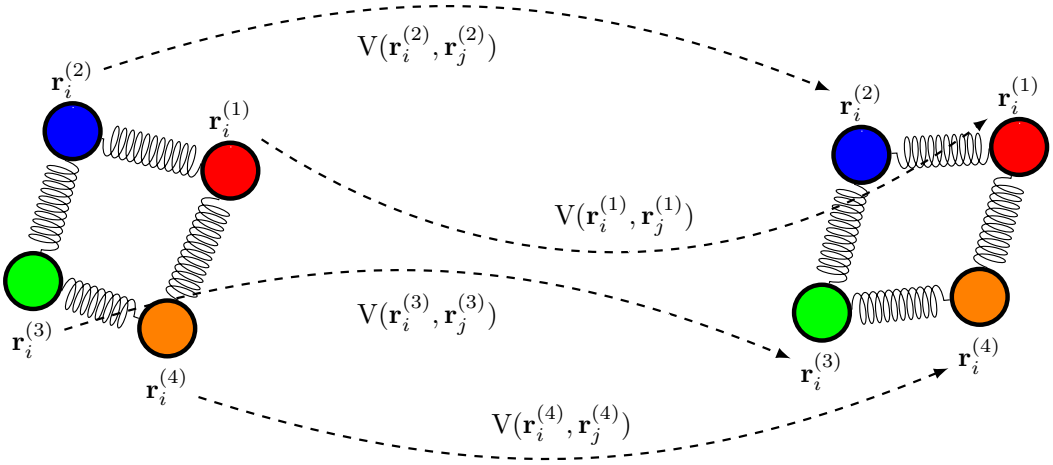

Figure 2.10: Illustration of the interaction of ring polymers in a multidimensional system. Beads on each ring polymer only interact with their corresponding bead on the other ring polymers. This leads to a computational expense that scales with the number of beads n

$$H_n(\mathbf{p},\mathbf{r}) = \sum_{i=1}^{N}\sum_{k=1}^{n}\left(\frac{(\mathbf{p}_i^{(k)})}{2m_i} + \frac{1}{2}m_i\omega_n^2(\mathbf{r}_i^{(k)} - \mathbf{r}_i^{(k+1)})^2\right) + \sum_{k=1}^{n} V(\mathbf{r}_1^{(k)}, ..., \mathbf{r}_N^{(k)}), \tag{2.135}$$

where $\omega_n = 1/\beta\hbar$ and the cyclic nature of the ring polymer ($\mathbf{r}_i^{(n+1)} \equiv \mathbf{r}_i^{(1)}$) is applied. When the external potential is applied it is important to note that each bead of the ring polymer of an atom only interacts with its corresponding bead on other atoms and therefore computational cost scales linearly with the number of beads (n). This is demonstrated in Fig 2.10. We use the same classical equations of motion from the one dimensional system updated to include the added dimensions.

$$\frac{d\mathbf{p}_i^{(k)}}{dt} = -\frac{\partial H_n(\mathbf{p},\mathbf{r})}{\partial \mathbf{r}_i^{(k)}}, \tag{2.136}$$

$$\frac{d\mathbf{r}_i^{(k)}}{dt} = -\frac{\partial H_n(\mathbf{p},\mathbf{r})}{\partial \mathbf{p}_i^{(k)}}. \tag{2.137}$$

The two operators $A_n(\mathbf{r})$ and $B_n(\mathbf{r}_t)$ are computed by averaging over the ring polymer beads at times 0 and t respectively.[44]

$$A_n(\mathbf{r}) = \frac{1}{n}\sum_{k=1}^{n} A(\mathbf{r}_1^{(k)}, ..., \mathbf{r}_N^{(k)}), \tag{2.138}$$

$$B_n(\mathbf{r}) = \frac{1}{n}\sum_{k=1}^{n} B(\mathbf{r}_1^{(k)}, ..., \mathbf{r}_N^{(k)}). \tag{2.139}$$

RPMD has been used to study a range of properties in different systems, such as chemical reaction rates, and more relevant to this work, the quantum diffusion constant and inelastic neutron scattering from liquid para hydrogen and the translational and orientational diffusions in liquid water. The results for the quantum diffusion coefficient of para hydrogen obtained by Miller and Manolopoulos are shown in Table 2.1 along with a comparison to experimental values and the CMD method described in the next Section.[46,47,125,127] These results show that both methods are very close to the experimental value with RPMD being almost perfect for a system at 25 K. These results demonstrate the ability of the two methods in recovering fully quantum properties for a system where classical MD completely fails. The same group also showed that the quantum diffusion coefficient could be recovered very close to the experimental value using the SPC/E model mentioned in Chapter 1[46], since then improvements in water models have led to even close values to experiment, an example being the q-TIP4P/F model that avoids issues with 'double counting' NQEs.[21]

RPMD can also be used to describe kinetic isotope effects, which can provide a useful tool in characterising reactive processes in chemical systems. In general, these effects manifest when the transition state in a reaction is less confined than the original reactant, resulting in a decrease in ZPE in the transition state species and therefore resulting in a faster reaction rate when NQEs are included. A demonstration of RPMD describing these effects was first shown for diffusion controlled reactions of hydrogen isotopes in water.[52] Where RPMD described the diffusion rate of muonium (an isotope of hydrogen of one-ninth the mass) compared to hydrogen and deuterium, to be in good agreement with experimental values where muonium diffuses at a similar rate, whereas classical simulations predicts that muonium diffuses much quicker due to having a higher Maxwellian root-mean-square velocity.[52] The quantum effect in this case can be described as an inverse isotope effect (i.e. when a transition state is more confined that the original reactant, NQEs inhibit the rate). When NQEs are included, the ring-polymer of a lighter atom is more swollen compared to that of a heavier atom, meaning motion through a more confined space is inhibited, therefore this inverse isotope effect leads to similar diffusion constants, something that the RPMD method can accurately account for, where classical MD fails.[52] Another application of the RPMD method is in the calculation of chemical reaction rates and

Method	25 K	14 K
CMD	1.52(8)	0.35(5)
RMPD	1.59(1)	0.33(1)
Expt.	1.6	0.4

Table 2.1: Table showing a comparison of the quantum diffusion coefficient of liquid para hydrogen for identical system sizes at two temperatures. The error for each value is given in brackets. Data taken from Miller and Manolopoulos. All values are reported in $\text{Å}^2\text{ps}^{-1}$.[47]

mechanisms of reactions that involve tunnelling processes. One of the first applications of RPMD in this area was the Eckart barrier and linearly coupled system-bath model benchmarks, which served the purpose of demonstrating the advantages of the method when dealing with both shallow and deep tunnelling systems.[46,47] In terms of reaction rates RPMD has been used to study the H + H_2 reaction, where classical MD at 200 K predicts a reaction rate that is over three orders of magnitude lower that the exact result.[127] However upon using the RPMD method, a reaction rate is obtained that is only 21% lower than the exact result. This lies within the expectation that the RPMD method underestimates rates for deep tunnelling systems across a symmetric barrier.[128] This increased accuracy over the MD method holds true when the temperature of the system is increased by 25 K. This allows for a largely increased range of feasible systems that can be studied. An example being the quantum rate calculation for the H + CH_4 system above temperatures of 400 K, a system of interest in combustion chemistry. The RPMD method converges for the quantum rate at temperatures ranging from 200 K to 2000 K, something that had not been possible before.[129]

Finally, an example of a large scale application of the RPMD method can be seen in the investigation of the hydride transfer in *Escherichia coli* dihydrofolate reductase (DHFR).[50] For this system the full ensemble of reactive trajectories were generated using the RPMD in combination with transition path sampling methods.[130] These results were able to distinguish between the effects of statistical and dynamical correlations on the transfer mechanism. Allowing a conclusive demonstration that while the hydride transfer is statistically correlated with the protein motion over a nanometer scale, the dynamic correlation decays over a much shorter time-frame. The RPMD method was also able to show that in this system, quantum tunnelling drastically increases the transfer rate. This further demonstrates the accuracy and

versatility of the RPMD method, highlighting its importance in a variety of chemical fields of interest, including combustion, hydrogen transfer, electron transfer, proton-coupled electron transfer and for any system where kinetic isotope effects are important.[131–133]

2.2.4.1 Limitations

While the RPMD method has been undoubtedly successful is a wide range of applications, there are also some drawbacks that can limit its applicability. Two of these, the spurious frequencies problem and the non linear operator problem will be briefly discussed here, highlighting circumstances where the RPMD method is not reliable

The spurious frequency problem manifests as the presence of unphysical frequencies in calculated spectra. The normal mode transformed Hamiltonian for a one dimensional harmonic oscillator can be written as[10,134,135],

$$H_n(\tilde{\mathbf{p}}, \tilde{\mathbf{r}}) = \sum_{k=0}^{n-1} \left[\frac{\tilde{p}_k^2}{2m} + \frac{1}{2} m \omega_k^2 \tilde{r}_k^2 \right], \tag{2.140}$$

where

$$\omega_k = \sqrt{\omega^2 + (2n/\beta\hbar)^2 \sin^2(k\pi/n)}. \tag{2.141}$$

For the RPMD method, the centroid mode ($k = 0$) oscillates at the harmonic frequency (ω), with the other modes oscillating at higher frequencies based on the number of beads. These oscillations are not related to the dynamics of the physical system and are purely artificial that arise from the structure of the extended phase space. However this is not usually a limitation, as for many systems the high-frequency oscillations are not important and are separate from the dynamics. An example of this being the diffusion coefficient, which are the zero-frequency components of velocity autocorrelation spectra. However the RPMD method runs into problems when attempting to calculate the absorption spectra of liquid water at room temperature, as the system contains high frequency physical vibrations, in this case the O-H stretching region of the spectrum.[134,136] In the calculated spectrum the high frequency region contained a number of spurious peaks arising from the internal modes of the ring-polymer.[134] This can be combated by decreasing the masses of the internal modes such that the spurious peaks are pushed above the range of interest, which can be done in the CMD method discussed in the next Section.[137] Overall it has been shown that spectra produced by RPMD are unreliable once the frequency is above that of the first ring-polymer excitation frequency.

A second issue that limits the applicability of RPMD is when calculating correlation functions for non-linear operators. As an example, while RPMD gives the exact quantum mechanical result for a harmonic oscillator when one of the correlated operators is a linear function of position or momentum.[44] However in the case of a non-linear operator, this is no longer the case and the method suffers in a similar way as described above, whereby additional spurious components are introduced that affect the time signal and lead to an inaccurate result. An example of this can be seen when studying the system of liquid para-hydrogen.[125] When computing incoherent dynamic structure factors using the non linear operators $e^{\pm i\mathbf{k}\cdot\hat{\mathbf{q}}_i}$ it was found that at low values of momentum transfer when the operators are approximately linear, RPMD gives a good agreement when compared to experimental data. However when this value of momentum transfer increases, the operators become more non-linear and as such RPMD becomes contaminated by internal modes and the results becomes increasingly inaccurate.

2.2.5 Centroid molecular dynamics

There also exist other methods that can be used to explicitly include NQEs other than RPMD. While these methods are not used in this work, it is worth mentioning an example for comparison. The method we examine here is the CMD[23,70–75] mentioned earlier, which is performed by evolving the centroid of the imaginary time PI classically, however this method suffers from being generally more computationally expensive than RPMD. The most commonly implemented version of CMD is the partially adiabatic version, which in contrast to RPMD uses a mass matrix that is diagonal in the normal mode coordinates $\tilde{\mathbf{x}}$ and momenta $\tilde{\mathbf{p}}$. The Hamiltonian for the CMD method expressed in these coordinates is

$$H_n(\tilde{\mathbf{p}},\tilde{\mathbf{x}}) = \frac{1}{2}\tilde{\mathbf{p}}^T\tilde{\mathbf{M}}^{-1}\tilde{\mathbf{p}} + \frac{1}{2}\tilde{\mathbf{x}}^T\tilde{\mathbf{K}}\tilde{\mathbf{x}} + V(\tilde{\mathbf{x}}) \tag{2.142}$$

where $\tilde{\mathbf{M}}$ is a diagonal matrix consisting of elements[134]

$$\tilde{M}_l = m\left(\frac{\Omega_l}{\Omega}\right)^2 \tag{2.143}$$

for $1 \leq l \leq n-1$, where Ω is the angular frequency. This moves all the non centroid normal modes to the same angular frequency. The centroid mass is set as the same mass of the physical particle to ensure that the correlation function remains correct in the classical limit. The angular frequency is chosen so that it is high enough to shift the non centroid modes outside the range

of frequencies present in the physical system so that the bead fluctuations are separated adiabatically from the motion of the centroid.[74] A consequence of this of shifting modes to high frequencies is that small timesteps must be used to ensure the correct integration of the equations of motion, leading to this implementation of CMD to be much more expensive than RPMD. CMD uses a different operator than RPMD, with CMD operators being evaluated at the centroid rather than averaging over the individual beads.

$$A_n = A(x_c) \tag{2.144}$$

where x_c is the centroid position. For linear operators both the CMD and RPMD methods give the same result for any given ring polymer configuration however in the case of non linear operators only the RPMD method gives the correct $t = 0$ value of the canonical correlation function. This is because the use of centroid operators means that the method does not reduce to PIMD as $t \to 0$ for non linear operators. However for many systems that are mildly quantum such as liquid water these two methods perform to a similar standard. We use the RPMD method in preference to the CMD approach in this work.

Chapter 3

Ring Polymer Interpolation

This Chapter introduces a new method for accelerating PI simulations, Ring Polymer Interpolation (RPI), which allows for significant computational time saving when compared to standard PIMD with minimal loss of accuracy. This method calculates the exact forces on a smaller number of ring polymer beads, then interpolates the forces on the unknown beads by using Kernel Ridge Regression (KRR). This Chapter begins with a brief introduction followed by the theory and implementation of RPI (including parameter optimisation). Finally, this method is applied to liquid water and liquid para hydrogen, and compared to other methods that accelerate PI simulations.

"One Ring to rule them all, One Ring to find them,
One Ring to bring them all, and in the darkness bind them,
In the Land of Mordor where the shadows lie."

-J.R.R Tolkien

The contents of this Chapter have, in part, been published:
S. Buxton and S.Habershon, *J. Chem. Phys.,* 2017, **147**, 224107

3.1 Introduction

As discussed in Chapter 2, imaginary time PI simulations allows for the exact calculation of time-independent quantum properties in molecular systems.[10,13,16,18–21,135,138–146] These simulations can be particularly appealing due to the multiple advances in improving the efficiency of classic MD simulations, from improved thermostats to the introduction of multiple time step methods. As PI simulations are based upon classical MD simulations, all these advances and improvements can be easily implemented into a quantum PI simulation. This has led to an increase in their use and they have been utilised in investigating a range of systems from different water phases.[16,17,20–27] to enzyme catalysed proton transfers[50,60–62] Methods have also been developed to enable quantum time-dependent properties to be calculated, these include RPMD[7,17,21,26,44–53] and CMD.[23,70–75]

As shown in the previous Chapter, PI simulations are exact in the $n \to \infty$ limit, however the value of n is typically far less than this. While the typical number for this is < 100, the computational expense is still n times more than the corresponding classical simulation, which can still be problematic depending on the method used to describe the PES of the system. While a simple empirical forcefield on a small system would not present any problem for a PI simulation, an increase in the system size or the use of a more complex or *ab initio* potential such as DFT can be prohibitive. Due to these problems, new methods have been developed that aim to allow these quantum PI simulations, one of the most significant is the Ring-Polymer Contraction (RPC)[10,11] discussed below. By separating the PES into 'high' and 'low' frequencies, a different number of beads can be used to evaluate each part with the high frequency forces calculated exactly and the low frequency forces using a contracted ring polymer containing fewer beads, which generally do not vary rapidly and also take a longer amount of time to evaluate compared to the high frequency contribution. This allows for a significant time saving while maintaining the accuracy of the quantum result. However it is evident that this approach breaks down if the PES is more complex and cannot be separated, such as if one were using an *ab initio* method such as DFT. A solution to this saw the development of an RPC-like method that relies upon the availability of a reference PES that is similar to the PES being investigated, but far less expensive to evaluate. This method evaluates the full PES using the reference potential and uses a contracted ring polymer for the more complex potential.[147,148] This does however make the assumption that the reference PES accurately represents the high frequency aspects of the system.

This has seen some success in obtaining values close to the full PI result when using density functional tight binding (DFTB) as the reference potential and standard DFT for the regular PES, giving a factor of 5 saving in terms of computational expense. This method has even been shown to work when using only 1 bead on the contracted ring polymer giving a reasonable result for the quantum properties. Another method proposed circumvents the cost of using a full *ab initio* PIMD method by using a model which is derived by using a force matching approach.[148] This matches the interatomic forces to those from an accurate electronic structure calculation without relying on an other parameters or input.

While these schemes are successful and give computational time saving while maintaining accuracy, they do have a major drawback in that they rely on the availability of a reasonable reference potential that is inexpensive to calculate. Therefore there is room for improvement when it comes to accelerating PI simulations. This work has developed a new method, RPI, that circumvents the requirement for a reference potential or the requirement of the PES being separated into distinct parts for 'high' and 'low' frequencies. Therefore this method can be applied to any generic PES and allows for significant computational time saving while still maintaining the accuracy of the full PIMD result. The method employs KRR[149–151] to evaluate the forces and potential energy on the n-bead ring polymer by using only a smaller number of PES evaluations on n' beads of the ring polymer at each time step. This method is trivial to implement and converges fully towards the exact PIMD result while making no prior assumptions about the PES.

The remainder of this Chapter is organised as follows. The theory RPI method is introduced and examined in detail, following this the RPI method is applied to two test cases, liquid water[21] and para-hydrogen[47], with the convergence of properties for each case examined and compared to that of other PI acceleration methods. Finally the Chapter concludes with an overview of how the RPI method can be improved further and possible future avenues to be explored.

3.2 Implementation of RPI

3.2.1 Bead correlation

The implementation of RPI requires no assumption about the underlying PES or the availability of a reference. The only assumption that is made is that adjacent beads display some level of correlation so that the full set of forces can

be calculated using only a smaller number of calculations. This correlation can be shown by the calculation of the imaginary time autocorrelation function defined as

$$C_{1j}^{\text{im}} = \langle V_1 V_j \rangle - \langle V_1 V_{1+\frac{n}{2}} \rangle, \tag{3.1}$$

where

$$\langle V_1 V_j \rangle = \lim_{n\to\infty} \frac{1}{(2\pi\hbar)^f} \int d^f\mathbf{r} d^f\mathbf{p} e^{-\beta_n H_n(\mathbf{r},\mathbf{p})} V(\mathbf{r}^{(1)}) V(\mathbf{r}^{(j)}). \tag{3.2}$$

Here $V(\mathbf{r}^{(j)})$ is the PES value calculated at bead j, f is the total number of beads used. As the autocorrelation function is a static property, it can be evaluated exactly in PIMD simulations. C_{1j}^{im} represents the average correlation in the PES values as single steps around the ring polymer, this approaches zero as the steps reach the bead diametrically opposite to the chosen reference bead. This correlation function is shown in Fig 3.1.[19,51,152] The main observation of this function is that there is a significant amount of correlation as one steps around the ring polymer. For example at $j = 5$, the function is still non-zero, indicating that that at this point there is still some correlation to the reference bead ($j = 1$). This confirms that it is not necessary to calculate the full force on every single bead, but instead the correlation can be exploited in order to reduce the number of full force evaluations and approximate the rest. This is the basis of the RPI approach.

3.2.2 Kernel-Ridge regression

The new RPI approach developed here employs interpolation to approximate the PES sampled during PIMD simulations. In a system containing an n-bead ring polymer in $3N$ dimensions, each ring polymer bead can be given a consecutive integer label from $1 \leq j \leq n$, with any bead being able to be labelled as $i = 1$ due to the fact that the ring polymer is cyclical. From this, a smaller number of beads ($n' < n$) can be chosen and a full PES calculation is made on these n' beads. The forces on the $(n - n')$ remaining beads can be evaluated using an interpolation based of the known PES values on the n' beads. From Fig 3.1, we can see that the interpolation can be performed in one dimensional space defined by the integer bead indices. In principle, any type of interpolation can be used to recover the forces on the unknown beads, however for this work we choose to use KRR[149–151], which is mainly due its simplicity and flexibility. KRR is also popular and well known within the wider community over a range of applications, with recent work

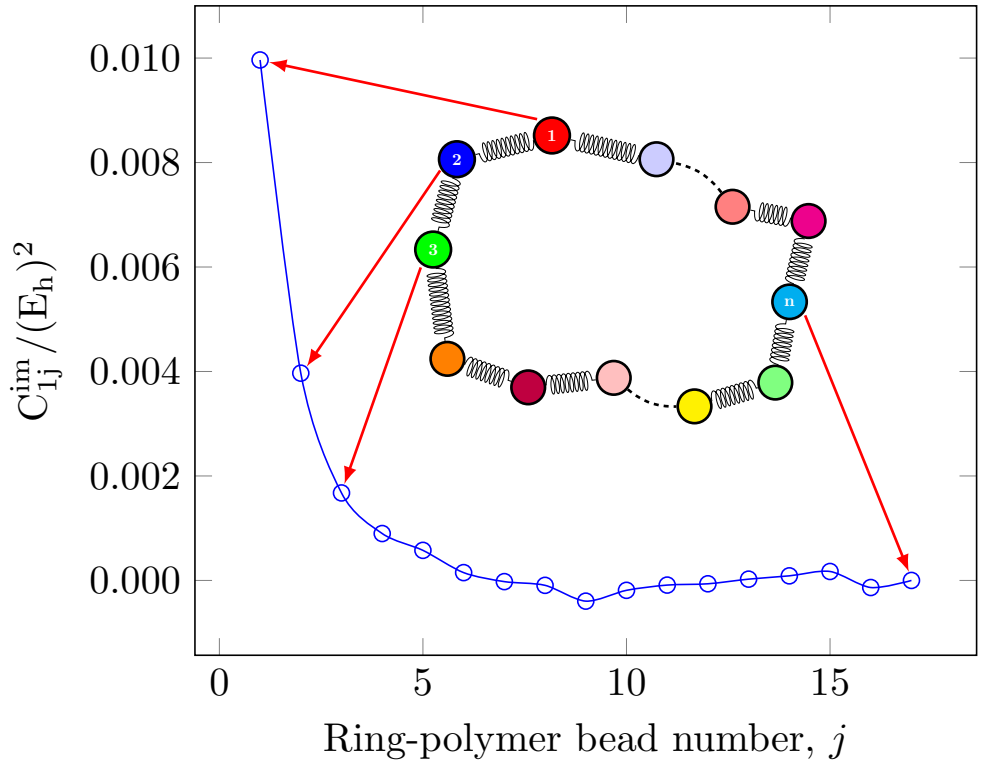

Figure 3.1: Potential energy imaginary-time correlation function for liquid water at 298 K using n = 32 beads. Starting from any reference bead (labelled 1 in this case), the correlation is shown to decrease as one steps around the ring-polymer. Correlation is observed for up to bead number five. A final note is that the ring-polymer is cyclical in nature so correlation increases as one returns closer to the reference

applying KRR to obtain accurate approximations to density functionals.[149] This is in addition to work carried out that uses KRR in order to accelerate the popular direct quantum dynamics method Monte Carlo Time Dependant Hartree (MCTDH).

Assuming that the PES has been evaluated at n' ring polymer beads, the PES at any bead k can be approximated using these values using KRR as

$$V(\mathbf{r}^{(k)}) \simeq \sum_{i=1}^{n'} w_i e^{-\alpha(k-\lambda_i)^2}, \tag{3.3}$$

where λ_i labels the indices on the n' beads of the ring polymer and α is a width parameter. The expansion weights w_i can be determined under the requirement that the PES values are recovered at the n' beads. This requires the solution of an $n' \times n'$ linear equation,

$$\mathbf{A}\mathbf{w} = \mathbf{g}, \tag{3.4}$$

where

$$A_{ij} = \delta_{ij}\sigma^2 + e^{-\alpha(\lambda_i - \lambda_j)^2}, \tag{3.5}$$

and

$$g_i = V(\mathbf{r}^{(i)}). \tag{3.6}$$

Here, σ^2 is a regularisation parameter, equally it can be viewed as representing the error in the PES evaluations at the n' beads. The vector $\mathbf{g}$ contains the n' PES values. Solution of Eq. (3.4) is straightforward using standard linear algebra packages.[153] The set of weights w_i can be computed by the inversion of $\mathbf{A}$,

$$w_i = \sum_{m=1}^{n'} A_{im}^{-1} V(\mathbf{r}^{\lambda_m}). \tag{3.7}$$

From Eq. (3.3) we now have

$$\begin{aligned} V(\mathbf{r}^{(k)}) &\simeq \sum_{i=1}^{n'}\sum_{m=1}^{n'} A_{im}^{-1} V(\mathbf{r}^{\lambda_m}) e^{-\alpha(k-\lambda_i)^2} \\ &\simeq \sum_{m=1}^{n'} \bar{\omega}_{km} V(\mathbf{r}^{\lambda_m}), \end{aligned} \tag{3.8}$$

where

$$\bar{\omega}_{km} = \sum_{i=1}^{n'} A_{im}^{-1} e^{-\alpha(k-\lambda_i)^2}. \tag{3.9}$$

The total potential energy of the full n bead ring polymer can now be computed using Eqs. (3.8 and 3.9),

$$V_n(\mathbf{r}) = \sum_{k=1}^{n} V(\mathbf{r}^{(k)}) \simeq \sum_{k=1}^{n}\sum_{m=1}^{n'} \bar{\omega}_{km} V(\mathbf{r}^{\lambda_m}). \tag{3.10}$$

The forces on each ring polymer bead can be obtained using the KRR interpolation in Eqs. (3.8 and 3.10) using the chain rule

$$\begin{aligned} \frac{\partial V_n}{\partial r^{(j)}} &= \sum_{m=1}^{n'} \frac{\partial V_n}{\partial \mathbf{r}^{\lambda_m}} \frac{\partial \mathbf{r}^{\lambda_m}}{\partial \mathbf{r}^{(j)}}, \\ &= \sum_{m=1}^{n'} \left(\sum_{k=1}^{n} \bar{\omega}_{km} \frac{\partial V(\mathbf{r}^{\lambda_m})}{\partial \mathbf{r}^{\lambda_m}} \right) \frac{\partial \mathbf{r}^{\lambda_m}}{\partial \mathbf{r}^{(j)}}, \\ &= \sum_{m=1}^{n'} W_m \frac{\partial V(\mathbf{r}^{\lambda_m})}{\partial \mathbf{r}^{\lambda_m}} \frac{\partial \mathbf{r}^{\lambda_m}}{\partial \mathbf{r}^{(j)}} \end{aligned} \tag{3.11}$$

where

$$W_m = \sum_{k=1}^{n} \bar{\omega}_{km} \tag{3.12}$$

The only thing left to do in order to obtain the forces is to determine the derivative of the positions of the n' beads with respect to the original n beads required by Eq. (3.11). This can also be solved using KRR, as the position of each n' reference bead can be expressed as an interpolation of the positions of the original ring polymer. The only new thing to note is that a separate interpolation is required for each degree of freedom in the system.

$$r_\eta^{\lambda_m} = \sum_{j=1}^{n} y_{\eta j} e^{-\gamma(\lambda_m - j)^2} \tag{3.13}$$

Where η is the position component of the KRR bead λ_m, $y_{\eta j}$ is the associated weight function and γ is a width parameter. The weights can be written in terms of the positions in the same way as in Eq. (3.7).

$$y_{\eta j} = \sum_{i=1}^{n} C_{ji}^{-1} r_\eta^{(i)} \tag{3.14}$$

Where the matrix C is of the same form as Eq. (3.5), however it has different associated parameters,

$$C_{ij} = \delta_{ij}\sigma_r^2 + e^{-\gamma(i-j)^2}, \tag{3.15}$$

where σ_r is the error parameter for the interpolation of positions. Combining Eqs. (3.13 and 3.14) gives

$$r_\eta^{\lambda_m} = \sum_{k=1}^{n} B_{mk} r_\eta^{(k)}, \tag{3.16}$$

where

$$B_{mk} = \sum_{j=1}^{n} C_{jk}^{-1} e^{-\gamma(\lambda_m - j)^2} \tag{3.17}$$

As a result of this second interpolation, the required derivative of the KRR bead positions with respect to the full n bead ring polymer is

$$\frac{\partial r_\eta^{\lambda_m}}{\partial r^{(j)}} = B_{mk} \tag{3.18}$$

By combining Eqs. (3.11 and 3.17), the forces on the full ring polymer can be determined from the KRR interpolation PES.

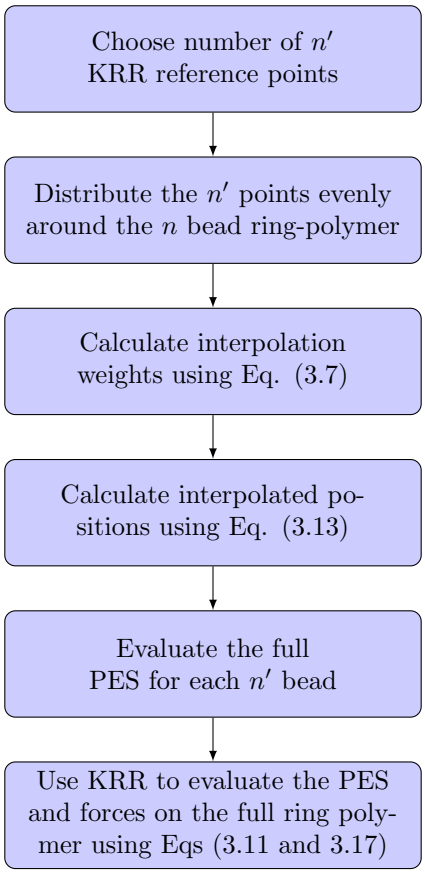

Figure 3.2: Illustration of the steps taken at each time-step of an MD simulation to implement the KRR approximation of the PES and forces.

In summary the RPI approach proceeds at each time step of a PIMD simulation and follows the same series of steps. First the indices of the n' KRR reference points are chosen, this is simply done by evenly distributing the n' reference points around the n bead ring polymer. After this, the required KRR interpolation weights are calculated using Eq. (3.14) and the interpolated positions using Eq. (3.13) for each degree of freedom. The full PES is then evaluated for each of the n' KRR reference points. KRR is then used to evaluate the total PES on the full ring polymer using Eq. (3.10) and the forces on the full ring polymer using Eqs. (3.11 and 3.17). This is shown in a flowchart for each time-step in Fig 3.2.

This completes the description of the RPI approach. It is clear that RPI requires n' evaluations of the full PES at every timestep of the simulation, compared to n evaluations when using the full PIMD method. Therefore it can be expected that the computational expense of this new approach should be roughly n'/n compared to that of the full PIMD method. The RPI method does require the solution of multiple matrix equations in order to determine

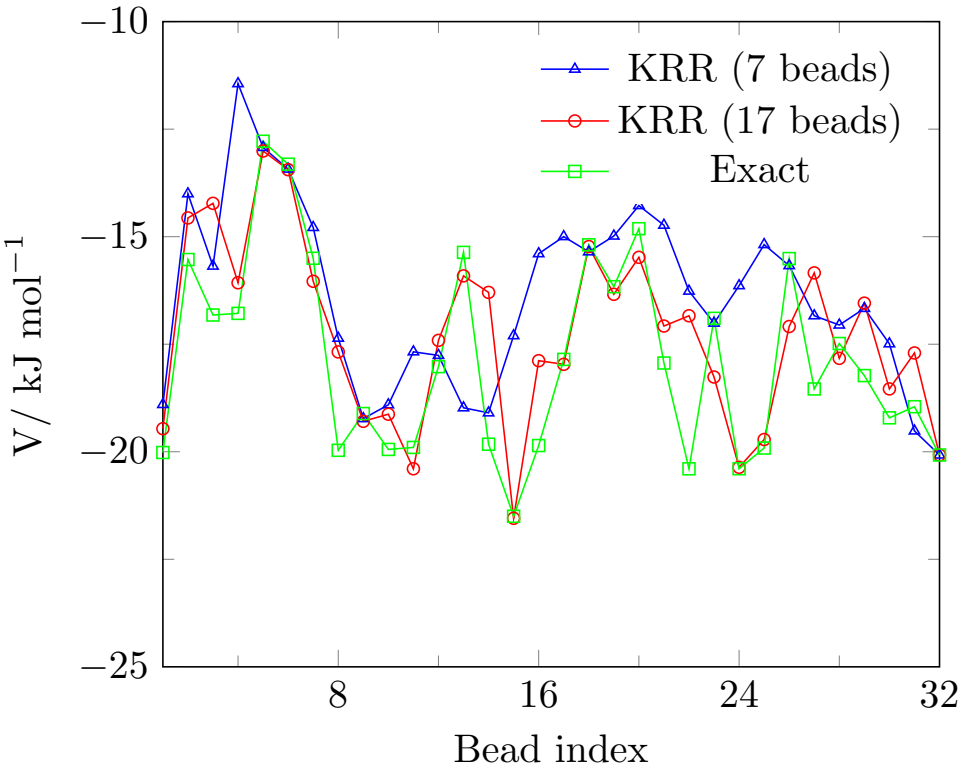

Figure 3.3: Interpolated PES values determined by KRR for one configuration of liquid water. The full PIMD result for each bead is shown, along with the KRR interpolated result using 7 and 17 reference beads

the weights for the position and PES interpolation. However in typical PIMD simulations the size of these matrices is a few tens or less, so the additional cost is mostly negligible. It is also worth emphasising that in contrast to methods like RPC, the RPI approach makes no prior assumptions about the PES of the system (besides the usual smoothness assumption). This means that RPI can be applied to any PES, including *ab initio* PESs and standard empirical force fields. The use of an interpolation based on KRR is similar to methods such as Gaussian Process Regression (GPR)[151] which has been used in approximating PES values for systems such as silicon or liquid water.[154,155] While the evaluation of the weights and expectation values in both methods are similar[154], the choice of kernel hyper parameters is more complicated in the GPR method as it uses marginal likelihood maximization, which must be performed at every time step and can be computationally expensive. In contrast to this, the KRR method that is used in RPI is motivated by practicality and simplicity, specifically it avoids the hyper parameter optimisation. The RPI approach could also be applied in *real time* PI simulations, although that is not something done in this work. In a standard coordinate representation,

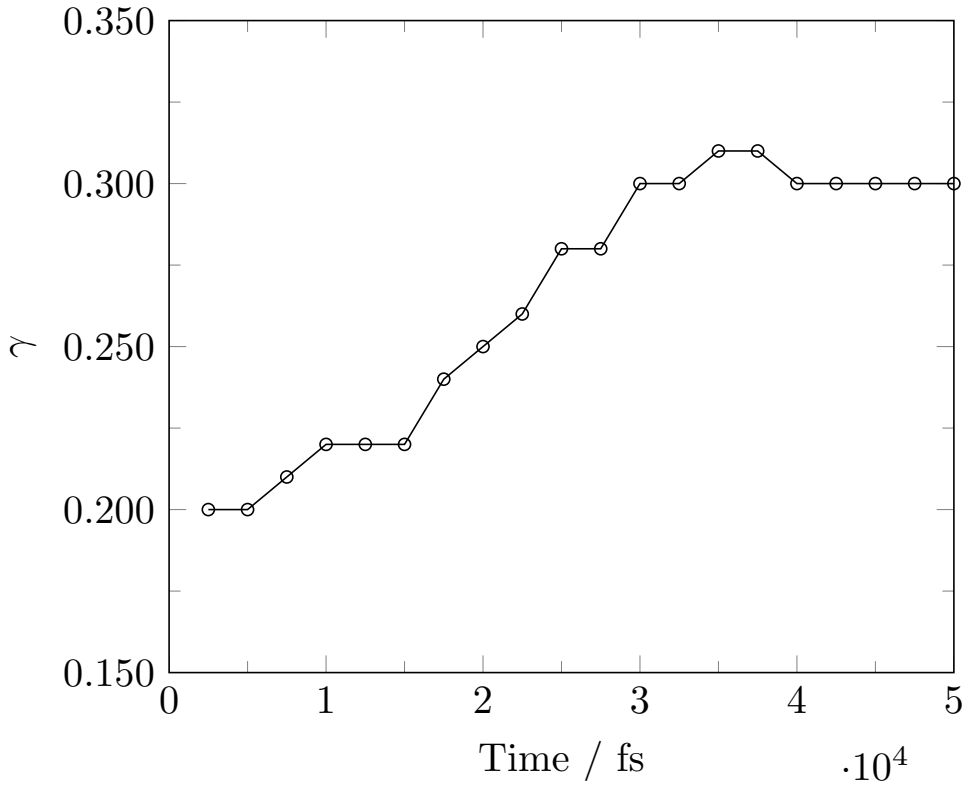

Figure 3.4: Illustration of the optimisation of the γ parameter over the course of a 50 ps equilibration using 9 KRR beads. The parameter steadily increases before levelling off and converging as the system fully equilibrates.

the calculation would involve a sum of potential energy values along a chain of configurations, making RPI perfectly appropriate for interpolating the PES values. An example of this is shown in Fig 3.3, where it can be seen how the KRR method works at each time step of a simulation. This shows the exact potential energy as well as the energy calculated when a smaller number of KRR reference beads are used in the RPI method. As expected, the exact PES values fluctuate somewhat as one steps around the ring polymer. It can also be seen that even when using only $n' = 7$ reference beads, the broad trends of the potential are captured. Increasing to $n' = 17$ beads yields a very good approximation to the exact result. This carries through to other properties that are calculated for a system, as shown below.

3.2.3 Parameter optimisation

In the KRR interpolation discussed above, there are two width parameters that require values. One for the position interpolation and one for the PES interpolation (α and γ). These width parameters determine the influence of

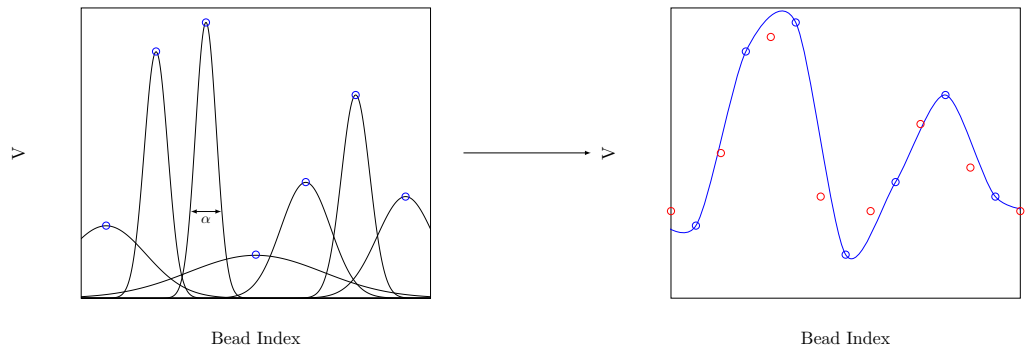

Figure 3.5: Illustration of how the Gaussians are placed on each reference point with the width parameter α determining their influence on neighbouring beads. This interpolation leads to the approximated unknown beads (red points) in the second panel. Note that the reference points are always exactly correct after the KRR interpolation

each reference point over its neighbouring space, an example of this is shown in Fig. 3.5. As discussed earlier, this method is motivated by simplicity and computational speed, therefore the method of optimisation is simplified as much as possible. The first simplification made is that $\alpha = \gamma$, this means that an optimisation of only one variable is required, this may not be the best choice in terms of complete accuracy, however for the purposes of a practical time saving scheme, complex optimisation or multiple parameters should not be required. In order to determine the best value of α, a simple approach of minimising the root mean square error between the PES values given by RPI and the exact PES values on the full set of ring polymer beads.

$$\varepsilon_{\mathrm{RMS}} = \sqrt{\frac{1}{n}\sum_{i=1}^{n}(\mathbf{V}_i^{\mathrm{RPI}} - \mathbf{V}_i^{\mathrm{FULL}})} \tag{3.19}$$

The overall error can be computed using any property of the system, for this work we use the potential energy. This can be run as an independent simulation over a short time scale in order to determine the best value for the parameters before full production runs are carried out. This parameter varies based on the number of n' beads being used. While determining the parameters before the full run is one approach, it relies on the assumption that the optimal value does not change over the course of the simulation. However this is not necessarily true, as a system equilibrates its properties change until convergence is reached, this change in the system can affect the optimal value for the width parameter. As an example, for an RPI simulation containing 9 beads, a simulation was run to determine the optimal parameter

value at the beginning and the end of the simulation, these numbers were not the same. This means that a single determination of the parameter values is not an appropriate method for obtaining the most accurate result. In order to obtain the most accurate value, the parameter value is changed on the fly during the simulation to continually provide the most accurate data. This is done by using a periodic check of the error at certain timestep intervals and re optimising the parameter if the error is higher than a user defined threshold value. This re optimisation only takes place over a few hundred timesteps and therefore does not add any significant computational expense. Furthermore this re optimisation typically only takes place 2 or 3 times over the course of a full run, further reducing the impact on expense. An example of this is shown in Fig 3.4, which shows how the γ value changes over the course of a simulation using re-optimisation every 2500 steps. This optimisation clearly shows how the γ parameter as the system equilibrates and the necessity for an on-the-fly re-optimisation to ensure the highest level of accuracy.

3.2.4 Ring-polymer contraction

The additional cost of PIMD compared to standard classical MD simulations should be emphasised as it highlights the need for more efficient methods. As shown previously, the PIMD approach requires n evaluations of the PES at each time-step for the determination of the forces acting on each of the n ring-polymer beads representing the quantum particles. In most cases, the evaluation of the PES is the most time-consuming part of the simulation, this means that PIMD simulations are $\sim n$ times more computationally expensive than the corresponding classical MD simulation. While this can be mitigated by use of parallel computing, an alternative is to develop new algorithms which can exploit the underlying features of the system in order to reduce the number of force evaluations at each time-step. RPC is one method that has been developed in order to address the issue of cost.

The major assumption of this approach is that the PES can be split into separate parts associated with 'high' and 'low' frequency motion:

$$V(\mathbf{r}) = V_{\mathrm{l}}(\mathbf{r}) + V_{\mathrm{h}}(\mathbf{r}). \tag{3.20}$$

It follows that the PES sampled by the ring-polymer in PIMD can be shown as

$$\sum_{i=1}^{n} V(\mathbf{r}^{(i)}) = \sum_{i=1}^{n} V_l(\mathbf{r}^{(i)}) + \sum_{i=1}^{n} V_h(\mathbf{r}^{(i)}). \tag{3.21}$$

As an example of this, $V_l(\mathbf{r})$ could correspond to the intermolecular component of an empirical force-field containing LJ and Coulomb (point-charge) interactions, whereas $V_h(\mathbf{r})$ could represent the intramolecular PES, which could contain bond-stretching and bond-angle bending contributions. This has been exploited in simulations of the SPC/F and q-TIP4P/F models.[10,21] As stated above, the characteristic vibrational frequency of the system provides a guide as to the required number of ring-polymer beads for obtaining converged properties ($\beta\hbar\omega/n \ll 1$). This suggests that the low-frequency contribution to the PES ($V_l(\mathbf{r})$) requires fewer ring-polymer beads for converged evaluation than that of the high frequency contribution ($V_h(\mathbf{r})$). RPC exploits this by evaluating $V_l(\mathbf{r})$ on a 'contracted' ring polymer containing n' beads as opposed to the full complement of n beads. This contraction is performed by initially transforming the ring-polymer into a representation of the normal modes of the free ring-polymer. Following this, the $n - n'$ highest frequency normal modes are removed and the inverse Fourier transformation back to real-space is performed, giving a n'-bead ring-polymer. The overall transformation is

$$\mathbf{r}_j^{(i)} = \sum_{i=1}^{n} T_{i'i}\mathbf{r}_j^{(i')}, \tag{3.22}$$

where $\mathbf{r}_j^{(i')}$ is the position of particle j in replica i' in the contracted ring-polymer, with the elements $T_{i'i}$ being functions that arise from the normal mode transformation of the Hamiltonian.[10] Following the contraction of the ring-polymer, the coordinates generated are used to evaluate the contribution of the 'low' frequency forces to the potential energy ($V_l(\mathbf{r})$) and is approximated as

$$\sum_{i=1}^{n} V_l(\mathbf{r}) \simeq \frac{n}{n'} \sum_{i'=1}^{n'} V_l(\mathbf{r}^{(i')}), \tag{3.23}$$

the forces on the full ring-polymer are evaluated from the contracted ring-polymer by using the 'chain rule'. As the long range intermolecular interaction terms are usually computationally expensive to calculate, evaluating $V_l(\mathbf{r})$ on a contracted ring-polymer gives an instant improvement in computational efficiency. It has been shown that this method offers simulations that are a factor of $\frac{n}{n'}$ faster than the corresponding full compliment PIMD simulation, as well as this, the convergence of the RPC method with respect to n' has been clearly established. This was done in terms of analysing quantum kinetic energies, potential energies and structural properties in the case of liquid

water.[10]

RPC can be further improved and refined in systems that contain dipolar electrostatic or point-charge interactions.[9,11] In this, the electrostatics are 'range-separated', with the short-range contributions calculated on a contracted number of beads and the long-range contribution evaluated once at the centroid. This strategy has been shown for the SPC/F empirical force-field, containing point-charge Coulombic interactions[11], it has also been shown to work for the TTM3-F model[9], possessing additional Thole-type polarisability. Overall the electrostatic RPC approach allows for PIMD simulations that are approximately a factor of 10 times faster than the standard PIMD simulation.

3.2.5 Ring-polymer contraction with a reference potential

While the RPC scheme has been very successful in allowing for much faster PIMD simulations, there is one main disadvantage with the method. This lies in the assumption that the full PES $V(\mathbf{r})$ can be separated into different contributions corresponding to 'low' and 'high' frequency forces. For empirical forcefields such as the SPC/F, TTM3-F and q-TIP4P/F water models, this separation of forces is simple; however when one is using a PES derived from *ab initio* simulations such as DFT or DFTB, an easy separation of the PES is not possible.

A new scheme was proposed that utilises a reference PES. In this method, the potential energy contribution to the ring-polymer Hamiltonian is rewritten as

$$\begin{aligned}\sum_{i=1}^{n} V(\mathbf{r}^{(i)}) &= \sum_{i=1}^{n} \left[V(\mathbf{r}^{(i)}) + V_{ref}(\mathbf{r}^{(i)}) - V_{ref}(\mathbf{r}^{(i)})\right] \\ &= \sum_{i=1}^{n} V_{ref}(\mathbf{r}^{(i)}) + \sum_{i=1}^{n} \left[V(\mathbf{r}^{(i)}) - V_{ref}(\mathbf{r}^{(i)})\right] \\ &\approx \sum_{i=1}^{n} V_{ref}(\mathbf{r}^{(i)}) + \frac{n}{n'} \sum_{i'=1}^{n'} \left[V(\mathbf{r}^{(i')}) - V_{ref}(\mathbf{r}^{(i')})\right]\end{aligned} \tag{3.24}$$

The third line of Eq.(3.24) shows the key approximation made by the reference-PES-based RPC scheme. The reference is evaluated on the full n-bead ring polymer however the difference term is calculated on a n'-bead ring-polymer, using coordinates that have been obtained in the same way as the original RPC approach shown above.

The major assumption which underpins this reference RPC (rRPC) scheme is that the difference potential $V(\mathbf{r}) - V_{ref}(\mathbf{r})$ slowly varies, in a similar fashion to how the intermolecular PES is assumed to be slowly varying in the original RPC scheme. For the rRPC method the computationally expensive full PES $V(\mathbf{r})$ is calculated on just $n' < n$ beads and the less expensive reference PES is evaluated on the full compliment of beads. This has been shown to be effective with simulations of liquid water and the protonated water dimer (both PESs described by DFT), allowing for PIMD simulations for a fraction of the cost of the standard approach.

The rRPC methodology relies in the assumption that a reference potential can be made available for the system of interest, this reference also has to be inexpensive to evaluate and gives a reasonable level of agreement to the properties of the system. In previous studies, DFTB and a force matched empirical PES have been used as a reference with much success. However the necessity of an available reference has its drawbacks such as added complexity in code management as there are two PESs required for evaluation at different points, also there is no guarantee that the reference potential will be good enough to model more complex chemical reactions. While this rRPC method generalises the standard RPC approach, it is still desirable to examine new methods that circumvent the necessity of a reference potential.

3.3 Application of RPI with liquid water

3.3.1 Simulation details

Our modelling of liquid water uses the q-TIP4P/F model[21] introduced in Chapter 2. In all simulations 32 ring polymer beads were used as this is more than enough to achieve full convergence of quantum properties of the system. A varying number of reference beads were used for the RPI implementation and the RPC method to which it is compared. A system size of 125 water molecules was used at a temperature of $T = 298$ K and density of $\rho = 0.997$ g cm^{-3}. The system was equilibrated for 50 ps using an Andersen thermostat[113], then static thermal averages were calculated in a further NVT simulation for 50 ps. PBCs were implemented and a cutoff of 9 Å was used for the LJ term in the potential energy. All properties of interest such as averaged potential energies, kinetic energies and Radial Distribution Functions (RDFs) were averaged over five independent calculations to allow for estimation of the errors associated with each method.

3.3.2 Time independent properties

The basis of the comparison of the RPI method and the RPC method lies in that they are both methods that rely on a smaller number of reference beads to determine the overall forces and properties of a system, therefore saving time. However as discussed earlier, RPC relies on the assumption that the frequencies of the system can be split into 'high' and 'low', with the RPC method only being applied to the low frequency forces. This is somewhat different to the RPI method as the RPI method makes no prior assumptions about the PES. This means that a direct comparison of results is not particularly appropriate, as RPC still uses a full compliment of beads for part of the PES evaluation. To allow for a fairer comparison, we use two different variants of the RPC method, the first method is the standard RPC method as described above, however the second variant is the RPC method whereby there is no full force evaluation for the high frequency forces i.e. the entire PES is calculated using a contracted ring polymer rather than just a single part, we call this the RPC(full) method. This brings the method closer to the RPI method, which is also calculated on the full PES instead of just one Section. Of course RPC should not be implemented in the RPC(full) format however it is a useful tool to highlight the fundamental differences in the two approaches. We also compare our method to the standard full PIMD where we simply run the simulation using different numbers of beads, to compare how the interpolation methods compare to the full PES evaluation on a smaller than optimal number of beads.

The convergence of the potential energy is shown in Fig 3.6. It shows the thermally averaged potential energy of the RPI method with respect to the number of KRR beads, where the number of KRR beads is representative of the number of full PES evaluations required at each time step. It is desirable that the RPI method converges as quickly as possible to the correct result, namely the result of the full PIMD simulation ($n = 32$). The results in Fig 3.6 clearly show that the RPI method converges quickly to the full 32 bead PIMD result as the number of KRR reference beads is increased. All RPI simulations used 32 ring-polymer beads, it is only the number of KRR beads that is altered for each run.

It can be seen that once the number of KRR beads reaches ~ 13, the 32 bead PIMD result is obtained. This means that RPI can obtain the full 32 bead result by evaluating fewer PES and force evaluations, giving an overall improvement by a factor of approximately 2.5. This is much better than a standard PIMD simulation where it can be seen that even if one uses $n = 24$

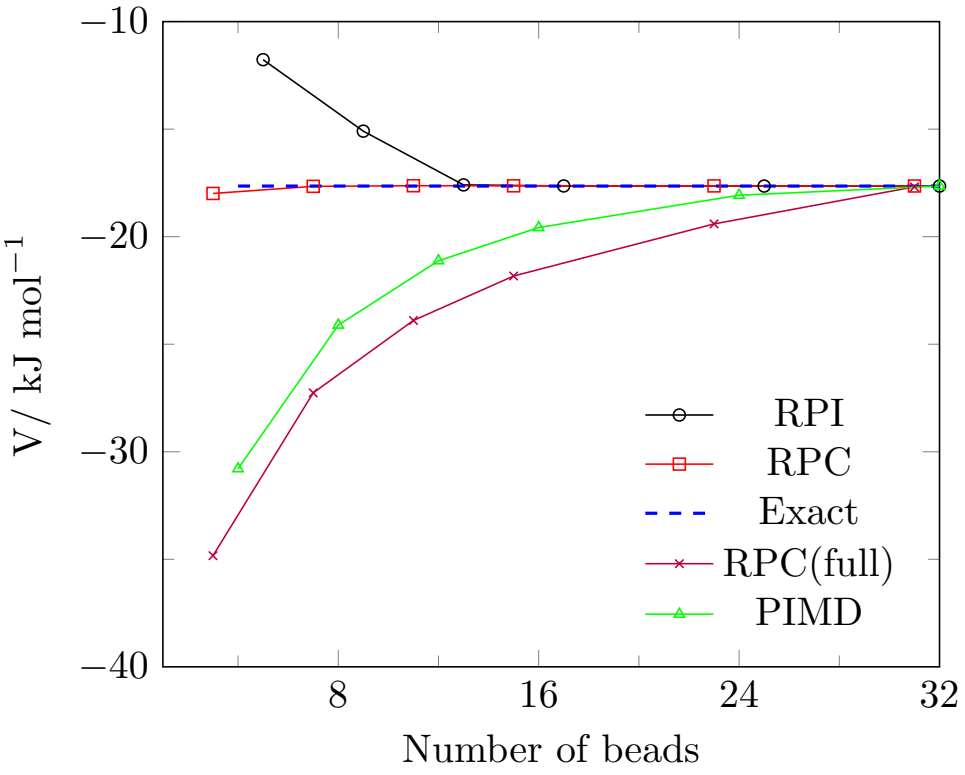

Figure 3.6: Convergence of the PI average of the potential energy of liquid water using multiple simulation methods. Error bars not shown as they are small and negligible compared to the scale of the results. This applies for all results in this Section.

beads, there is still a significant error in the average PES value. As expected, the standard RPC method rapidly converges to the correct answer, requiring approximately 7 beads for the evaluation of the intermolecular terms (the intramolecular term is still calculated on the full compliment of beads).

The RPC(full) method does not perform well by comparison, performing even worse than the standard PIMD method, which was to be expected. This is because this variant uses a contracted ring-polymer to approximate the full PES, whereas RPI uses an interpolation method that, due to the correlation between beads, is capable of approximating the full ring polymer PES with only a few reference points.

The same trend is evident in Fig 3.7, which shows the convergence of the average quantum kinetic energy of the system using the same set of methods. Just like the potential energy, the RPC method converges quickly using $n = 7$ ring polymer beads for the intermolecular term and $n = 32$ for the intramolecular term, whereas the RPC(full) method converges slower than all other methods used. For the RPI method, we find that the exact value

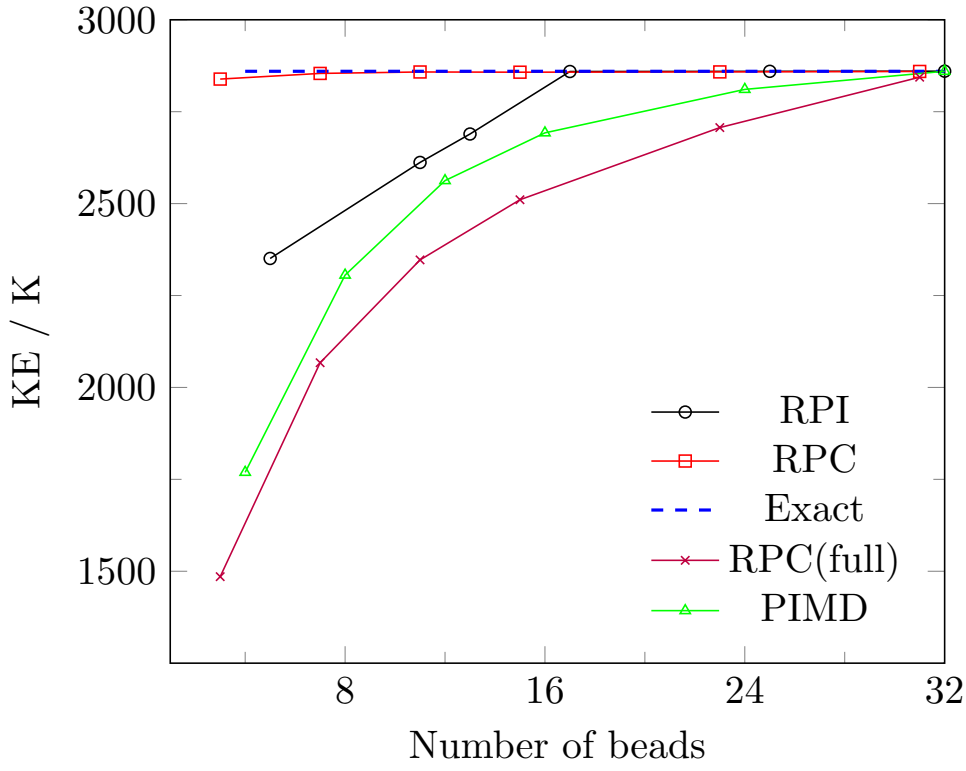

Figure 3.7: Convergence of the PI average of the kinetic energy of liquid water using a virial[156] estimator for multiple simulation methods.

is reached using $n' \geq 17$ ring polymer beads, which is not as good as the potential energy case. However this still gives a result that requires only half the number of beads and therefore force and PES evaluations to obtain the exact PIMD result. The result of both Figs 3.6 and 3.7 demonstrate that the RPI method can give a fully converged result using only 50% of the number of force and PES evaluations that would be required if one were performing standard PIMD.

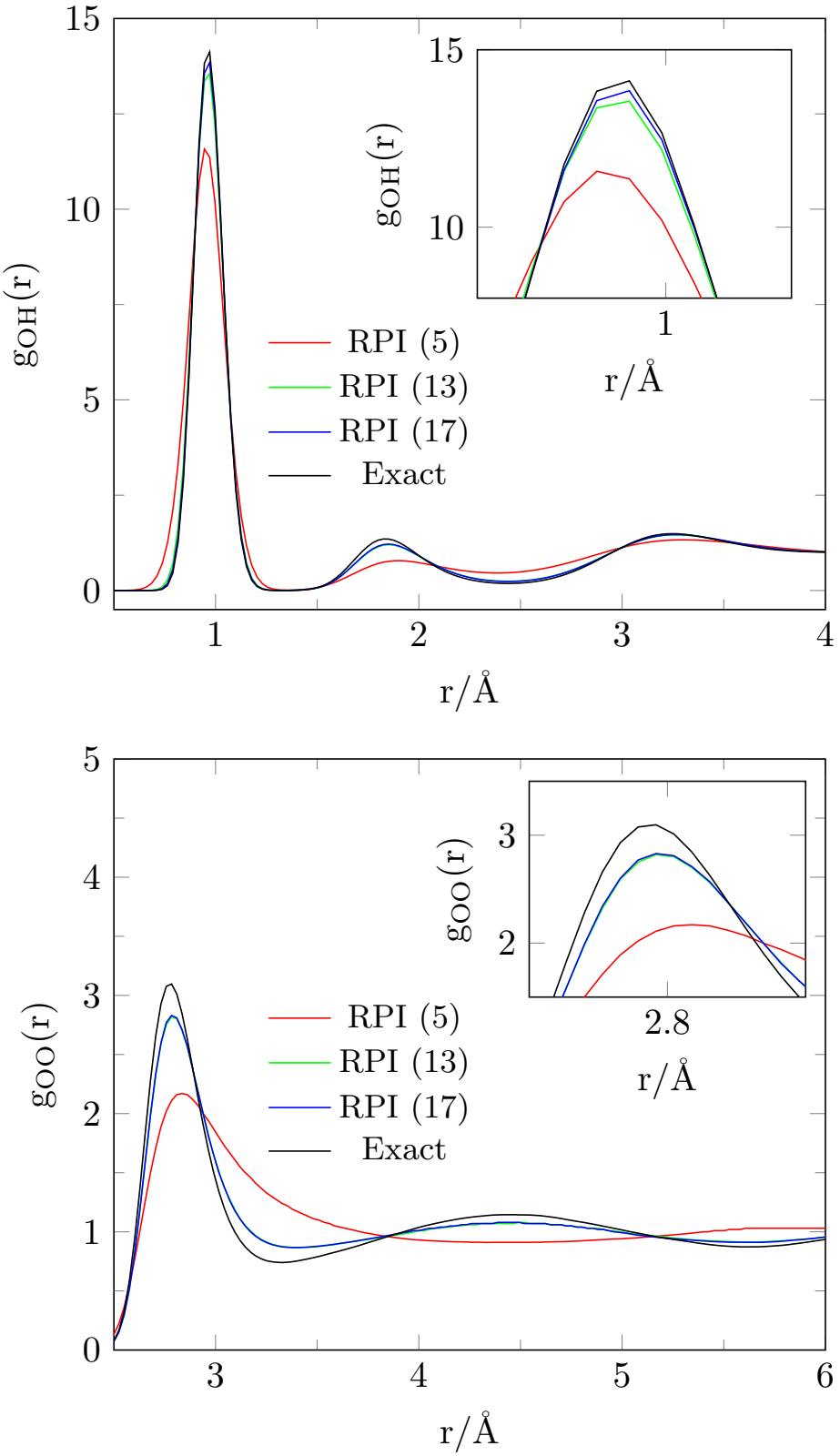

Figure 3.8: Effect of the number of RPI reference beads on the O-O and O-H RDF's of liquid water at 298 K. The inset depicts the intramolecular peak around 1 Å

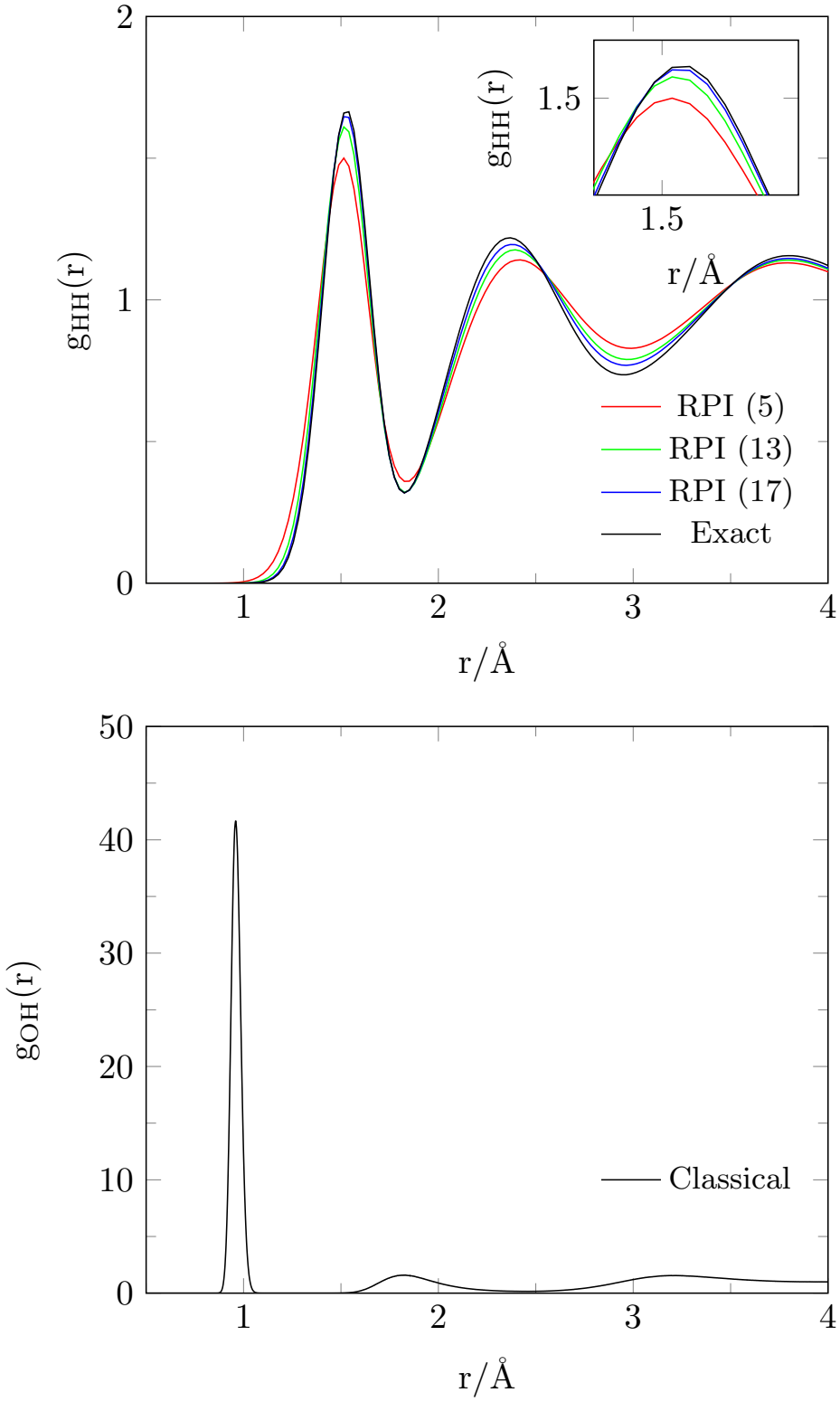

Figure 3.9: Effect of the number of RPI reference beads on the H-H RDF of liquid water at 298 K. The inset depicts the intramolecular peak around 1 Å. The classical O-H RDF is also shown.

Showing the convergence of these two averaged properties is a good demonstration of the RPI method and shows that it can reliably converge on the correct PIMD result at a lower computational cost. However to further show the capabilities of this method, an assessment of a larger scale overall structural property is performed. This is in the form of the O-H, O-O and H-H RDFs in Figs 3.8 and 3.9

Of the three RDFs, the O-H distance is strongly affected by NQEs, therefore and errors in the treatment of these in this RDF should be clear. The RDF for the O-H RDF and the H-H RDF are effectively converged using only $n' = 13$ reference beads, whereas the O-O RDF is less converged but not unreasonable and still heading towards the correct answer. In fact, in all three cases the broad features of the RDFs are captured by using as little as $n' = 5$ reference beads, this even applies to parts of the long range structure. Overall these three RDFs show that the atomic level structure calculated in RPI simulations is identical to that obtained from a full PIMD simulation. For comparison it should be noted that when performing an RDF using classical MD, the size of the first (intramolecular) peak in the RDF is higher than 40, whereas using a quantum method reduces this significantly. This shows that the RPI method is very successful at reproducing the quantum O-H RDF using a minimal number of reference beads and that results quickly converge on the quantum result even when there is such a large disparity between the magnitudes of the classical and quantum values.

3.3.3 Time dependent properties

The RPI method can also be used to calculate time dependent properties of a system. One example of this is the diffusion constant, which is calculated using the RPMD method to approximate the velocity time correlation function. This provides an insight as to how the RPI method fares when dealing with the evolution of a ring polymer in comparison to other methods. The results for this are shown in Fig 3.10. It can be seen that, just like the static properties of the system, the RPI method converges on the exact answer using a fewer number of beads than full PIMD. However unlike the static properties, it takes more beads to obtain convergence on the exact result. For RPI $\sim n = 24$ beads are required to obtain full convergence. Despite RPI giving the worst result for smaller number of beads, the method actually converges on the correct answer at a lower number of reference beads, with both RPC methods and PIMD converging after $\sim n = 28$ beads. It is not surprising that a time dependent property of the system takes longer to converge to

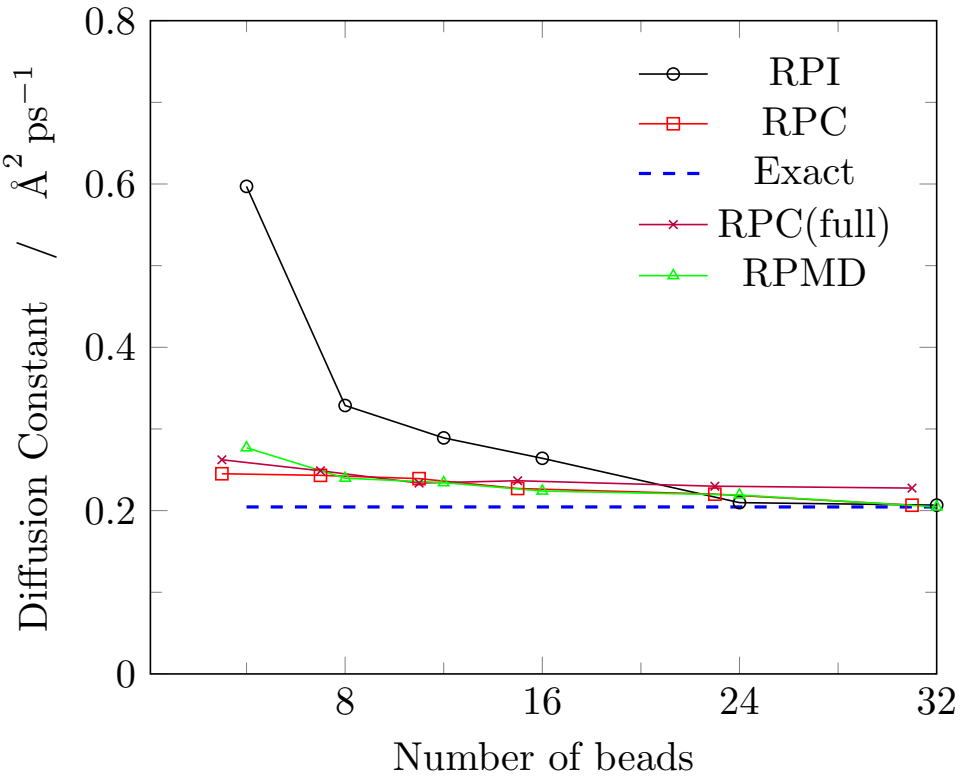

Figure 3.10: Convergence of the PI average of the diffusion coefficient of liquid water using multiple simulation methods

the full result than a time independent property. As this involves using the RPMD to approximate the correlation function, which is based upon approximated forces and therefore approximated evolution. However despite the initial slow convergence, RPI can still obtain a correct result while saving a smaller amount of computational time. Despite other methods obtaining a closer approximation at a low number of reference beads, the convergence is still slow and takes more reference beads than RPI.

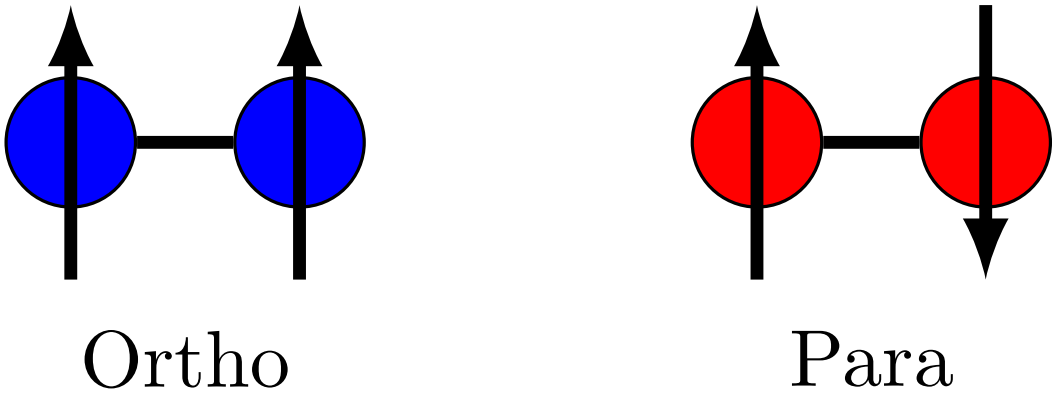

Figure 3.11: Illustration of the two different proton spin conformations of the H_2 molecule

3.4 Application of RPI to liquid para-hydrogen

A second test of the RPI method was performed for a system of liquid para-hydrogen. This is H_2 with the proton spins on each atom oppositely aligned, this is illustrated in Fig 3.11. The para form is chosen as it is more stable than the corresponding ortho from and because the para form is dominant at low temperatures, $> 99\%$ at temperatures lower than 25 K. Due to the small size of hydrogen and the low temperatures studied, NQEs play a significant role in the properties of the system. Therefore this system provides a more robust test of the RPI method with regards to effectively capturing the quantum effects present in systems.

3.4.1 Simulation details

The simulation of liquid para hydrogen was carried out in a similar fashion to liquid water. 50 ps was used for the equilibration and sampling using the canonical ensemble at 25 K. As in water, $n = 32$ ring polymer beads were used for the simulations with a varying number of reference beads for the RPI method. 32 beads is more than sufficient to converge PIMD properties fully. 108 molecules were used for the simulation. 50×2 ps trajectories were used for the sampling of dynamics properties. The distance cutoff for the potential energy was set as 7.9 Å. Five simulations were used to determine the averages for the time dependent and independent properties of the system. The RPI width parameters were optimised in the same way as described above, with parameters being changed when the error was higher that a tolerance value. The potential is comprised of a Silvera-Goldman pair potential.[157] There is no intramolecular term as the H-H molecule are treated as spheres with no

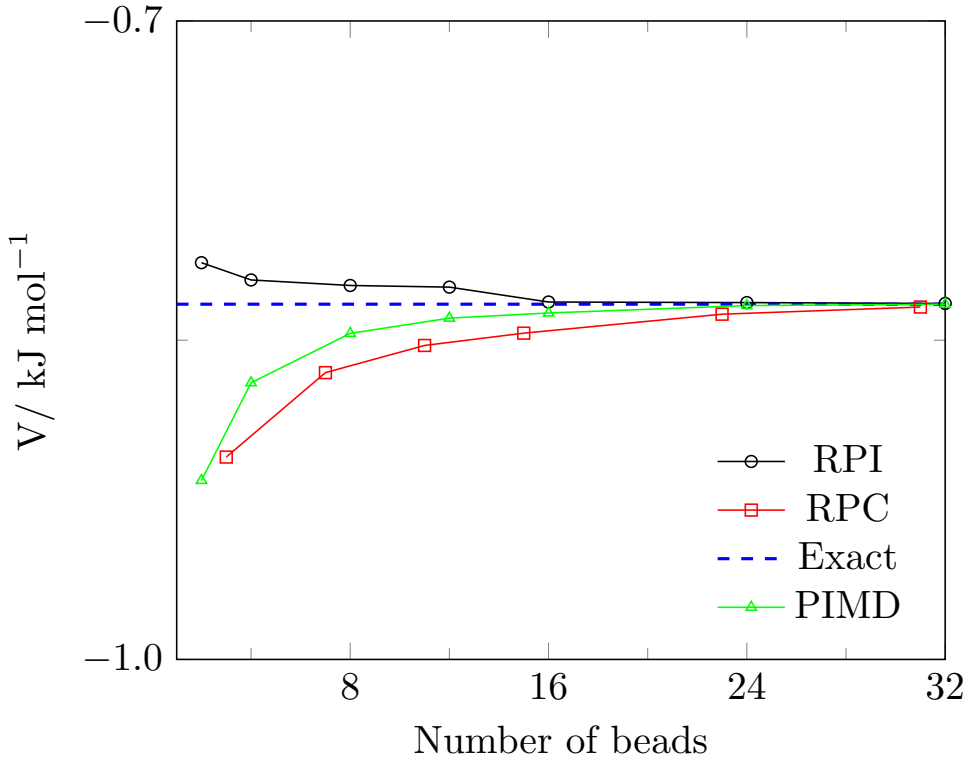

Figure 3.12: Convergence of the PI average of the potential energy of liquid para hydrogen using multiple simulation methods

internal interactions, only intermolecular interactions between them.

3.4.2 Time independent properties

As in the case of liquid water, the RPI method is compared to standard PIMD and RPC. However in the case of para hydrogen, the PES cannot be separated into high and low frequency contributions. This means that the contracted ring polymer must be used for the entire evaluation of the PES instead of using the full compliment of beads for part of the PES. As such, this system also serves as a good example of the advantages of the RPI method, as it can be applied just as easily without any modifications required. As a result of this, the RPC method implemented for the para hydrogen system is not how the method should be used and the direct comparison with RPI is used to illustrated the robustness of the RPI method, rather than criticise the RPC method for a shortcoming it was not designed to compensate for. The convergence of the potential energy for liquid para hydrogen is shown in Fig 3.12. It can be seen that the RPI method converges on the exact value using only $n' = 17$ reference beads, which is comparable to the amount required

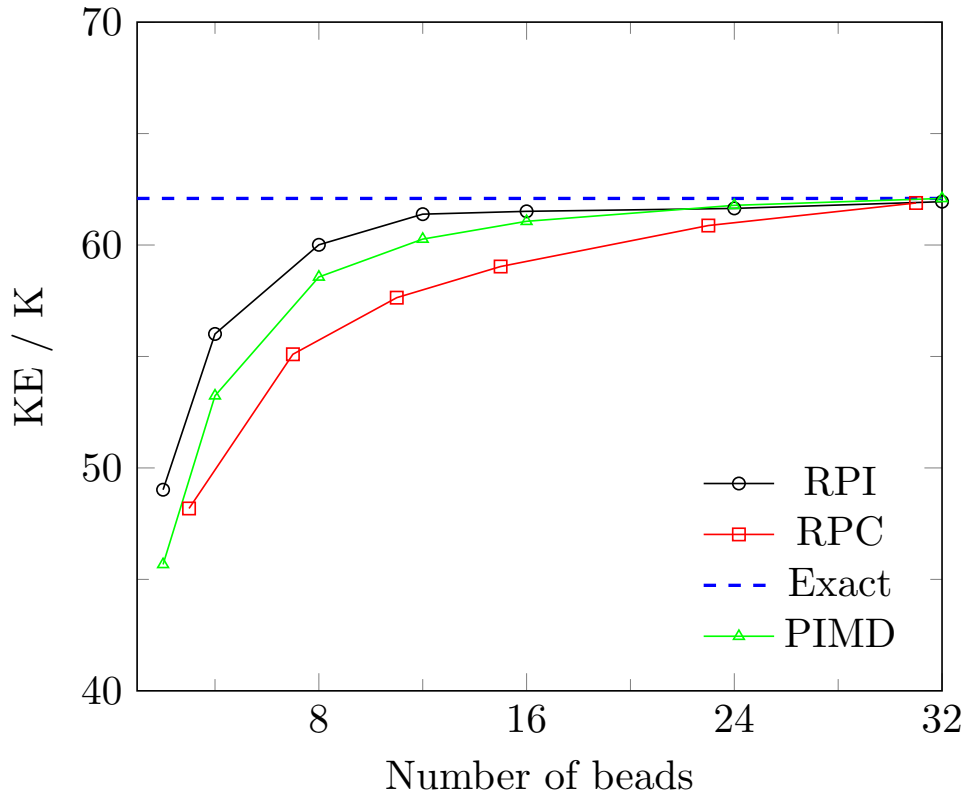

Figure 3.13: Convergence of the PI average of the kinetic energy of liquid para hydrogen using multiple simulation methods

for liquid water. The number of beads for RPI may be slightly higher for convergence of para hydrogen due to the larger role quantum effects play in the system. The RPI method converges faster than standard PIMD and much quicker than RPC, which doesn't converge at all until a full compliment of beads are used. This serves to highlight the deficiencies of the RPC method when applied to a system where the PES cannot be separated. It can also be noted for RPI that the unconverged reference bead numbers $n' < 17$ are still closer to the exact PIMD result than the other two methods, whereas for liquid water this was not obviously the case, further showing how the RPI method can account for systems where quantum effects are high and other methods suffer by comparison. The relative time saving for this property is similar to that of liquid water ($\sim$ 2.5x), however as para-hydrogen is a much smaller and easier to model system, the real world time saving for this system is not as important. It is encouraging to see for the RPI method that the relative time saving remains similar for both systems. The convergence of the kinetic energy is shown in Fig 3.13. This follows identical trends to the potential energy plot. The RPI method converges faster than the other two

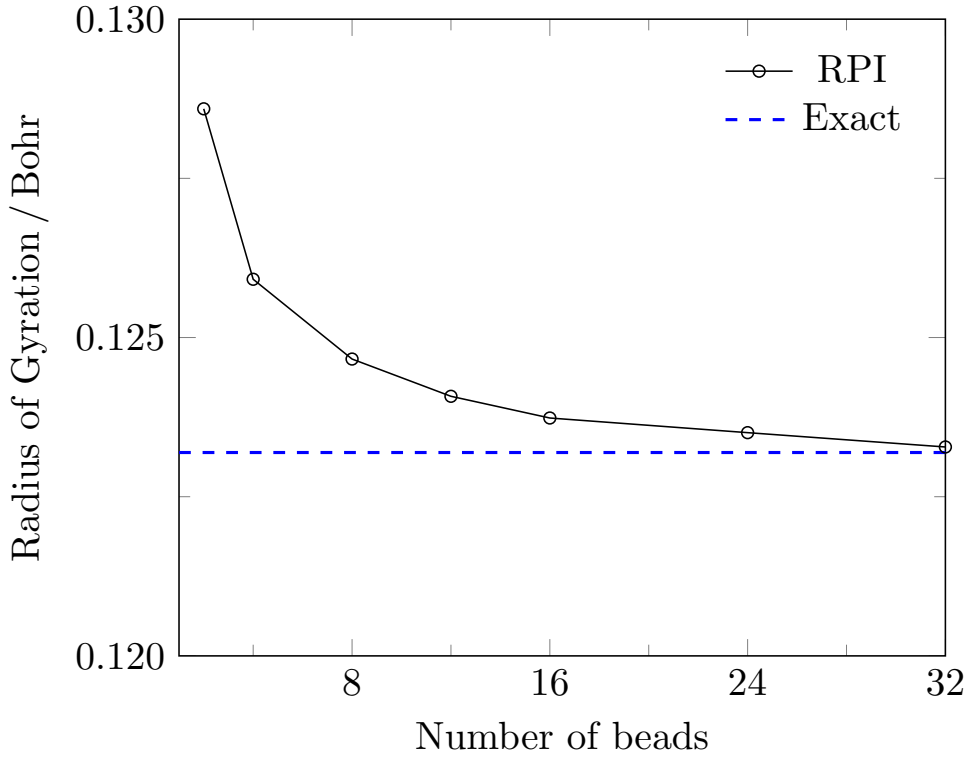

Figure 3.14: Convergence of the PI average of the radius of gyration of liquid para hydrogen using the RPI method

methods and gives a fully converged answer within error by using only $n' = 17$ reference beads. The PIMD method requires at least ten more than this and the RPC method once again requires a full compliment of beads in order to give a converged result. Once again this is nearly identical to the results obtained for liquid water and in fact the number of reference beads required to converge the kinetic energy is practically identical for both systems. Again it is worth emphasising that the RPI method converges faster and quicker than the PIMD method, showing that RPI should be preferred to simply reducing the number of PIMD beads used in the simulation.

A final example of a time independent property is the radius of gyration. Fig 3.14 shows how this property converges to the exact result using the RPI method. It is immediately obvious that based on the scale of the y axis, the RPI method converges rapidly on the correct result, using only $n' = 2$ reference beads a value is obtained that is $0.05 <$ away from the full PIMD result. This shows that the radius of gyration for this system is accurately captured using RPI at almost any number of reference beads and as such is not a source of error in the inclusion of quantum effects. Other methods are now shown for this as they are likely to be the same or worse, with almost

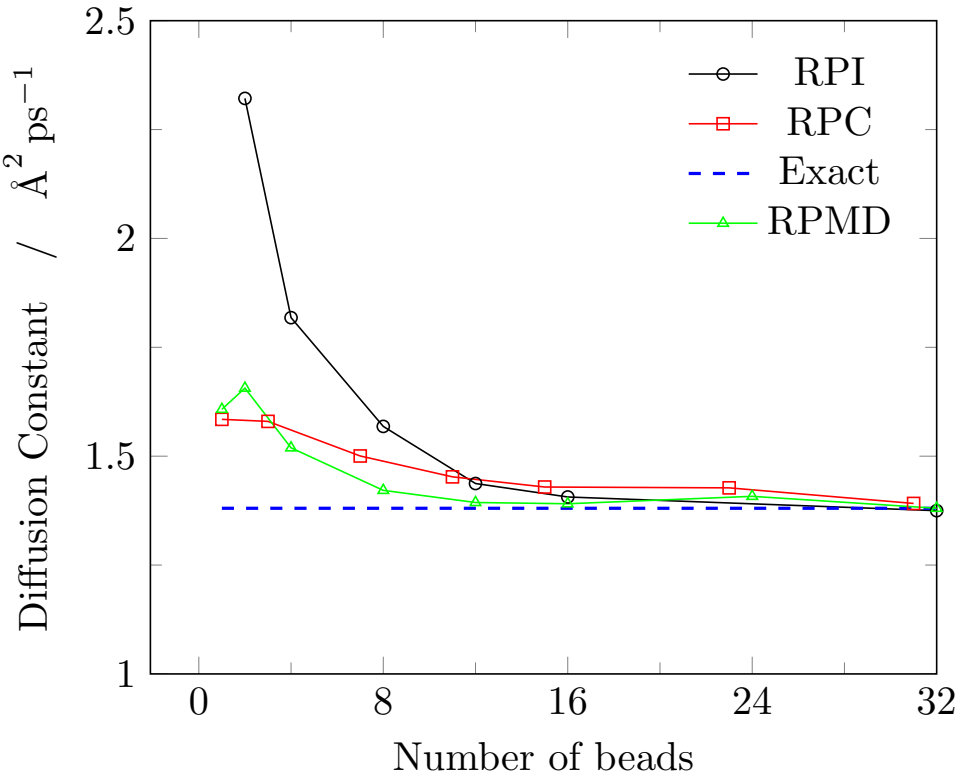

Figure 3.15: Convergence of the PI average of the diffusion constant of liquid para hydrogen using multiple simulation methods

no improvement possible over the RPI method. This is useful to calculate for para hydrogen because of the high degree of quantum effects present in the para hydrogen system. This means the ring polymer beads are fairly dispersed and the radius of gyration will fluctuate far more than in other atoms such as oxygen in water. Accurately capturing the radius of gyration is therefore important in accounting for the quantum effects in the system.

3.4.3 Time dependent properties

Time dependent properties can also be calculated for liquid para hydrogen in the same way as liquid water. The RPMD approximation to the correlation function is used to compute the diffusion coefficient.

The convergence of the diffusion constant is shown in Fig 3.15. The RPI method performs well here, giving the correct result using $n' = 17$ reference beads, whereas RPC requires a full compliment before it gives the correct answer. RPMD however performs well here, requiring a similar number of beads as RPI to give the full RPMD result. Unlike the time independent properties and similar to the liquid water system, the RPI method initially

converges slower than RPC and RPMD, then overtakes and achieves the full result quicker.

3.5 Conclusions

This Chapter has introduced a new method for accelerating PI simulation using KRR to interpolate the forces and energy on ring-polymer beads, thereby reducing the number of full force evaluations required and therefore reducing computational expense. The benefits of using this method are threefold. The number of beads required to converge full PIMD properties allows for half of the number of PES calculations to be performed. Furthermore RPI method does not make any prior assumptions about the PES, meaning it can be applied to any system of interest. Finally the method is simple to implement in terms of computer coding and required only slight modifications to existing PIMD code, there is no reason to believe why this method could not be implemented easily into existing commercial and well known MD packages.

In order to test the performance the RPI method as well as show that the advantages laid out above are valid, RPI was applied to two different systems, liquid water and liquid para hydrogen. As well as this, these two systems were used to test the standard PIMD method as well as two variants of the RPC method. The first being the RPC method whereby the contracted ring polymer is only applied to the low frequency forces of the system, with a full compliment of beads used for the high frequency forces. The second variant applies the contracted ring polymer to the entire PES, bringing it more in line with how the RPI method works.

In order to obtain maximum accuracy with the RPI method, the parameter controlling the Gaussian width during the interpolation was optimised on-the-fly during each simulation using a least squares error. During the run, a reoptimisation would occur when the error rose above a certain threshold, thereby ensuring that the optimal parameter value was used during the entire simulation, as this value had a tendency to change as the systems studied underwent equilibration. Only one parameter was used for all aspects of the interpolation in order to simplify the method, as optimising multiple parameters would be more of a computational expense than the minor increase in accuracy was worth.

Time independent and time dependent properties (using the RPMD approximation) were calculated for both systems. Encouragingly, in almost all cases, the RPI method achieved full convergence of PIMD properties using

approximately half the number of reference beads, as well as showing faster convergence than the methods used for comparison. While the standard RPC method was far superior when applied to liquid water, when applied to para hydrogen it was unable to produce accurate results due to the inability to split the PES like in liquid water. This highlights the versatility of the RPI method, as it does not suffer in accuracy when applied to the two systems tested. However for systems where such a separation of the PES is possible, alternative PIMD acceleration methods such as RPC may be more appropriate than the RPI method.

The overall conclusion from all properties discussed is that the RPI method accurately converges on the exact PIMD result using at most half the number for reference beads, leading to a factor of at least two in computational time saving. This is all without making any prior assumption about the PES and indeed RPI is perfectly capable of being applied to any complex PES, including those generated using *ab initio* electronic structure methods. The computational overhead of the RPI method outside of the PES evaluation is small, and therefore has no impact on speed. The implementation of the method is simple and requires only a small modification to any existing PIMD code. From this work, we find that the computational time of a typical RPI simulation with liquid water using $n' = 15$ reference beads and $n = 32$ beads in total, is only 20-25% more expensive than RPC in the case of empirical PESs, therefore if one can split the PES into 'high' and 'low' frequency components, RPC is perhaps more appropriate than RPI. However, if such a separation is not possible, then it can be argued that the RPI method is the easier route, especially when compared to *ab initio* RPC methods that require two PESs to be available. The RPI method could potentially be used in the context of a reference based potential scheme, providing a hybrid method that would accelerate the overall PIMD scheme and the evaluation of the reference potential on the ring polymer.[147,148]

Chapter 4

Quantum Effects in Free Energies of Water Phases

Under terrestrial conditions, hexagonal ice (I_h) is thermodynamically stable relative to cubic ice (I_c), although the origin of this difference is not well defined or understood. Pure I_c cannot be produced experimentally, therefore computational chemistry is used as a tool to investigate this. However the water potential models used for this in the past have mostly been with models that ignore the intramolecular flexibility of water molecules, accurately describe intermolecular hydrogen bonding or include the role of NQEs. This Chapter shows how the role of NQEs affects the stability of I_h relative to I_c and shows how they are the dominant factor behind this stabilisation. Stacking disordered phases are investigated along with the melting points of the two pure phases in order to investigate the role of quantum effects in the stability of these phases and how other properties are affected. Finally liquid water is investigated in order to see how quantum effects and anharmonicity play a role in the melting temperatures of I_c and I_h.

"Draco dormiens nunquam titillandus."

-J. K. Rowling

The contents of this Chapter have, in part, been submitted for publication.

4.1 Introduction

The nucleation and crystallisation of ice and general systems still remains a challenge to experimental and computational chemists in terms of obtaining accurate thermodynamics and kinetics. While there are many different configurations of ice that exist at various pressures and temperatures, under terrestrial conditions only one ice phase exists, this is hexagonal ice (I_h), which leads to the well known 6-fold symmetry in snowflakes. However both experimental and theoretical work has shown that this polymorph is only very slightly the most stable thermodynamically with another polymorph, cubic ice (I_c), predicted to be only ∼30-150 J mol^{-1} higher in free energy than I_h. This difference, while very small, means that I_h is more stable than I_c at temperatures and pressures accessible on Earth[158–160], meaning that pure I_c crystals are only rarely observed, with creation in a laboratory leading to conversion to I_h such that a pure crystal is practically impossible to obtain. As a result of this, the free energy difference between the two polymorphs of ice I remains an unsolved problem which challenges the understanding of the hydrogen bonding in water and ice.

The structures of I_h and I_c are shown in Fig 4.1. It shows the I_h comprising alternating layers of water molecules stacked in an *ABAB...* arrangement, with the hydrogen bonding structure determined by the Bernal-Fowler 'ice rules'[161], where there is no proton ordering and each oxygen atom participates in two short (covalent) O-H hydrogen bonds and two long (intermolecular) hydrogen bonds. The other polymorph (I_c) obeys the same ice rules however there is a different stacking arrangement. Instead of the double layer *ABAB* stacking, I_c follows an *ABCABC...* pattern as in cubic close packed systems. The stacking pattern in I_c is the same as diamond, with the oxygen atoms taking the positions of the carbon atoms. There also exists hybrid structures of I_h and I_c which are stacking disordered.[55] These stacking disordered structures can span the entire range between I_h and I_c, with some being very close These disordered ice structures have been strongly implicated in the nucleation of ice in the low temperature regions of the upper atmosphere.[162–164] These disordered structures are investigated further later on in the Chapter in addition to the pure I_h and I_c polymorphs.

From the known and theoretically computed physical properties, both the pure I_h and I_c polymorphs are found to be similar and behave in almost identical ways, despite the clear difference in their stacking patterns. The vibrational spectra are very similar, which highlights the similar hydrogen bonding environments generated by the proton disorder.[99–101] Other prop-

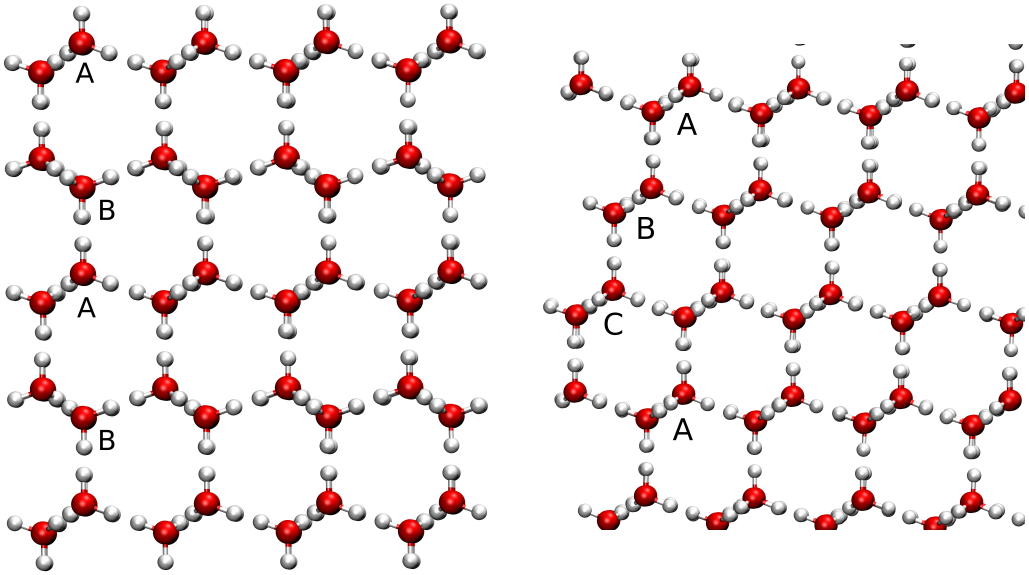

Figure 4.1: Illustration of the two Ice I polymorphs, I_h (left) and I_c (right). I_h displays an *ABAB...* stacking pattern whereas I_c displays an *ABCABC...* pattern.

erties are also near identical such as the density, thermal expansivity and configurational entropy.[102–104] The differences in the structures begin to show themselves upon investigation of the simulated RDFs, where it can be seen that the first nearest neighbour environment in each structure is effectively identical, however there are pronounced differences in the second neighbour shell and beyond.[99,100] The differences at longer range are a result of the different hexamer arrangements in the two polymorphs, with I_h exhibiting both variants (chair- and boat- type) of hexamer, with I_c only containing the chair-type hexamer.

Due to the inability to create pure I_c under laboratory conditions and the knowledge that experimental data on notionally I_c is actually stacking disordered with varying degrees of cubicity, one of the most useful tools to investigate pure I_c and I_h is computer simulation. Empirical water models have been employed in previous work whereby the water geometries have been fixed at an optimised reference geometry (e.g. the TIP4P and associated water models)[100,102,104,165,166] and then combined with normal mode analysis and standard expressions for partition functions (both classical and quantum). The results of these studies have suggested that the differing vibrational density of states in the librational region give rise to the I_h polymorph being lower

in energy than I_c. Other methods have also been used that go further than empirical models such as DFT to calculate the vibrational density of states and free energies (discussed in Chapter 1).[99,167,168] Relevant to the work presented in this Chapter is studies that have been carried out using the PBE functional to calculate the anharmonic and harmonic free energies for I_h and I_c. The results of this work are contrary to work done with empirical models, with the *ab initio* DFT PBE method suggesting that it is anharmonicity (particularly in the O-H stretching region of the spectrum) that is responsible for the free energy difference between the two polymorphs.[99] However in all cases studied, none have been able to provide a complete explanation for this energy difference. As an example, the use of simulations with the mW model entirely lack librational motion and O-H bonds, therefore it could be expected that the results would show the two polymorphs having identical stability. The free energies for the two polymorphs have been accurately calculated for this model[163], with the free energy difference between I_c and I_h being much smaller than the enthalpy released per mole when stacking disordered ice transforms to I_h in calorimetry experiments. However the mW model is consistent with calculations of the relative I_h/ I_c stability extracted from fitting a model of dislocation loop shrinkage dynamics to experiment[169,170], which suggests that there is either a problem with the defect dynamics model or with the actual calorimetry experiments. Models based on TIP4P and similar rigid water geometries neglect intramolecular flexibility, however previous studies have shown that these interactions can be very important in influencing the predicted physical properties in water and other systems where hydrogen bonding is prevalent.[21] As well as this, computed free energies based on harmonic analysis (or its vibrational self-consistent field (VSCF) extension to include anharmonicity) do not sample the fully coupled configurational fluctuations associated with thermal motion. This can clearly be seen in the the vibrational spectra in the O-H region, which have a tendency to show more defined peaks in harmonic (and self-consistent) analyses over the broader peaks seen in experimental studies and standard MD simulations. An extra thing to note is that DFT studies using VSCF predict a much larger than expected free energy difference of $\sim$ 630 J/mol^{-1}, when compared to experimental studies that show a much lower energy difference.[99]

Finally, NQEs[7,16–20] such as ZPE are usually treated using either quantum harmonic-oscillator partition function[100,104] or by the explicit calculation of vibrational eigenstates using a self-consistent field.[99,167,168] The NQEs on sampled configurational space and unit cell fluctuations are therefore generally ignored. In this work we show that when these NQEs are fully accounted

for, a new picture for the relative stability of I_h and I_c emerges. We also examine the free energy of liquid water over a temperature range, allowing the computation of the melting points for the two variants.

4.2 Free energy calculations

A general method to calculate the free energies of liquid and solid water phases is to calculate the difference between the system of interest and a reference system where the free energy is known by either a numerical or analytical method. Thermodynamic integration can be used to accomplish this.

This Section will focus on the methods used to calculate free energies for systems that fully account for quantum effects. This work uses the more recently developed scaled coordinate method, which provides stability improvements over the older Morales Singer method.[142]

4.2.1 Morales Singer method

The MS method begins with the quantum thermal partition function used for PIMD discussed in the theory Chapter.

$$Z_n = \frac{1}{(2\pi\hbar)^n} \int d\mathbf{p} \int d\mathbf{x}\, e^{-\beta_n H_n(\mathbf{p},\mathbf{x})}. \tag{4.1}$$

Here $H_n(\mathbf{p},\mathbf{x})$ is the classical Hamiltonian of an n-bead ring polymer with potential $V(x)$ acting on each bead.

$$H_n(\mathbf{p},\mathbf{x}) = \sum_{j=1}^{n} \left[\frac{p_j^2}{2m} + \frac{1}{2} m\omega_n^2 (x_j - x_{j-1})^2 + V(x_j) \right]. \tag{4.2}$$

In this Hamiltonian $\beta_n = \beta/n$, $\omega_n = 1/(\beta_n\hbar)$ and $\beta = 1/(k_b T)$. From this function an integration variable λ is introduced and the λ-dependent partition function can be defined as

$$Z_n^{\mathrm{MS}}(\lambda) = \frac{1}{(2\pi\hbar)^n} \int d\mathbf{p} \int d\mathbf{x}\, e^{-\beta_n H_n^{\mathrm{MS}}(\mathbf{p},\mathbf{x};\lambda)}, \tag{4.3}$$

with Hamiltonian

$$H_n^{\mathrm{MS}}(\mathbf{p},\mathbf{x};\lambda) = \sum_{j=1}^{n} \left[\frac{p_j^2}{2m} + \frac{1}{2} m w_n^2 (x_j - x_{j-1})^2 + \lambda V(x_j) + (1-\lambda) V(q_c) \right], \tag{4.4}$$

where

$$q_c = \frac{1}{n}\sum_{j=1}^{n} x_j. \tag{4.5}$$

From this is can be seen that when $\lambda = 1$, the full PI is performed and represents the quantum mechanical system with $Z_n^{\mathrm{MS}}(1) = Z_n$. Conversely, when $\lambda = 0$, the momentum is integrated out of the partition function, leaving the equation as

$$Z_n^{\mathrm{MS}}(0) = \frac{1}{(2\pi\hbar)^n}\left(\frac{2\pi m}{\beta_n}\right)^{n/2}\int d\mathbf{x} e^{-\beta V(q_c)} e^{-\beta_n \sum_{j=1}^{n}\frac{1}{2}m\omega_n^2(x_j - x_{j-1})^2}. \tag{4.6}$$

This can be written in terms of normal modes $\{\tilde{q}_k\}_0^{n-1}$ of the free ring polymer.

$$Z_n^{\mathrm{MS}}(0) = \frac{1}{(2\pi\hbar)^n}\left(\frac{2\pi m}{\beta_n}\right)^{n/2}\int d\tilde{x}_0 e^{-\beta V(q_c)}\prod_{k=1}^{n-1}\int d\tilde{x}_k e^{-\frac{1}{2}\beta_n m\omega_k^2\tilde{q}_k^2}. \tag{4.7}$$

Here, $q_c = \tilde{q}_0/\sqrt{n}$ and $\omega_k = 2\omega_n \sin(k\pi/n)$. This can be simplified by performing Gaussian integrals over $\tilde{q}_k$ for $k > 0$, remembering that $\omega_n = 1/(\beta_n\hbar)$ and $\beta_n = \beta/n$ and by making use of the identity $\prod_{k=1}^{n-1} 2\sin(k\pi/n) = n$.

$$Z_n^{\mathrm{MS}}(0) = \frac{1}{(2\pi\hbar)}\left(\frac{2\pi m}{\beta}\right)^{1/2}\int dq_c e^{-\beta V(q_c)}. \tag{4.8}$$

As this simplifies to the classical partition function, it is shown that when in the limit of $\lambda = 0$ for Eq.(4.6), this corresponds to the classical system with $Z_n^{\mathrm{MS}}(0) = Z_1$. From these limits, the free energy difference between the classical and quantum mechanical systems can be calculated. The λ-dependent free energy can be defined as

$$F(\lambda) = -\frac{1}{\beta}\ln[Z(\lambda)]. \tag{4.9}$$

The free energy of quantization can be calculated by thermodynamic integration as

$$\Delta F = F(1) - F(0) = \int_0^1 d\lambda F'(\lambda). \tag{4.10}$$

By looking at Eqs. (4.3, 4.4 and 4.9), we can see that for the MS method we have

$$F'_{\mathrm{MS}}(\lambda) = \left\langle \frac{1}{n}\sum_{j=1}^{n}\left[V(q_j) - V(q_c)\right] \right\rangle_{\lambda}^{\mathrm{MS}}, \tag{4.11}$$

where the angular bracket $\langle \dots \rangle_{\lambda}^{\mathrm{MS}}$ represents an ensemble average using the MS Hamiltonian with a specific value of λ,

$$\langle \dots \rangle_{\lambda}^{\mathrm{MS}} = \frac{1}{(2\pi\hbar)^n Z_n^{\mathrm{MS}}(\lambda)} \int d\mathbf{p} \int d\mathbf{q} e^{-\beta_n H_n^{\mathrm{MS}}(\mathbf{p},\mathbf{q};\lambda)}(\dots). \tag{4.12}$$

The average in Eq.(4.11) can be calculated using a PI method such as PIMC or PIMD to evaluate Eq.(4.12). However there is a drawback to the MS method which occurs as $\lambda \to 0$. In this case, the centroid position q_c is sampled from a classical Boltzmann distribution, while the bead displacements $q_j - q_c$ are sampled from a free ring polymer distribution. The result of this is that the estimator in Eq.(4.11) can fluctuate greatly. An example of this can be seen in the water molecule, at 298 K where the free ring polymer radius of gyration is $\simeq 0.2$Å.[52] This means that during the calculation of Eq.(4.11), sampling will include multiple water configurations where both O-H bonds have been compressed by 0.2Å or more. When using the q-TIP4P/F water potential[21], this compression leads to a change in energy of around 135 kJ mol^{-1} relative to the sampled equilibrium configuration. These extremely large changes in energy make it very difficult to evaluate Eq.(4.11) and in cases where $\lambda = 0$, it is possible that $F'_{\mathrm{MS}}(\lambda)$ can become infinite due to the PES containing singularities. In addition, the forces on the atoms can become very large as $\lambda \to 0$, preventing integration of the equations of motion. These issues help to explain why the MS method has only been applied to mildly quantum systems, where the radius of gyration is much smaller and these problems do not have as much influence. A new method was proposed by Habershon and Manolopoulos which aimed to solve these problems to allow the study of systems the are more quantum.[16]

4.2.2 Scaled coordinate method

The SC method claims to fix the problems of the MS method by replacing the Hamiltonian in Eq.(4.4) with the new SC Hamiltonian[16]:

$$H_n^{\mathrm{SC}}(\mathbf{p},\mathbf{q};\lambda) = \sum_{j=1}^{n}\left[\frac{p_j^2}{2m} + \frac{1}{2}m\omega_n^2(q_j - q_{j-1})^2 + V(\lambda q_j + [1-\lambda]q_c)\right]. \tag{4.13}$$

This is only a small change compared to the MS Hamiltonian however it has important repercussions. As shown above, $\lambda = 0$ corresponds to the classical system and $\lambda = 1$ corresponds to the quantum system. Thermodynamic integration can again be used to calculate the free energy of quantization, by defining,

$$u_j^\lambda = \lambda q_j + [1 - \lambda] q_c, \tag{4.14}$$

the integrand of the thermodynamic integration becomes

$$F'_{\mathrm{SC}}(\lambda) \left\langle \frac{1}{n} \sum_{j=1}^{n} (q_j - q_c) \frac{\partial V(u_j^\lambda)}{\partial u_j^\lambda} \right\rangle_\lambda^{\mathrm{SC}}, \tag{4.15}$$

where the angular bracket $\langle \dots \rangle_\lambda^{\mathrm{SC}}$ represents an ensemble average involving the Hamiltonian in Eq.(4.13) and the corresponding partition function,

$$\langle \dots \rangle_\lambda^{\mathrm{SC}} = \frac{1}{(2\pi\hbar)^n Z_n^{\mathrm{SC}}(\lambda)} \int d\mathbf{p} \int d\mathbf{q} e^{-\beta_n H_n^{\mathrm{SC}}(\mathbf{p},\mathbf{q},;)} (\dots). \tag{4.16}$$

With this change to the Hamiltonian, the resulting method is very different from the MS method. Particularly the integrand in Eq.(4.15) resembles the centroid virial estimator for the kinetic energy.[156] When $\lambda = 1$ Eq.(4.15) gives exactly twice the quantum mechanical contribution to the kinetic energy. This estimator also works well as $\lambda \to 0$, where it can be shown that it gives $F'_{\mathrm{SC}}(\lambda) = 0$. From this it is expected that the SC method will give stable thermodynamic integration across the full range of λ values, solving the problems generated by the MS method. This is utilised in Chapter 4 where the quantum corrected free energies for hexagonal and cubic ice are calculated anharmonically and harmonically in order to determine the origin of the difference in stability between the two polymorphs.

4.2.3 Ice phases

The free energy difference between two systems is given by

$$\Delta A = \int_0^1 \left\langle \frac{\partial V_\lambda(\mathbf{r})}{\partial \lambda} \right\rangle_\lambda d\lambda, \tag{4.17}$$

where the angular brackets represent a canonical average at λ

$$\left\langle \frac{\partial V_\lambda(\mathbf{r})}{\partial \lambda} \right\rangle_\lambda = \frac{1}{2\pi\hbar)^f Z_\lambda} \int d^f\mathbf{p} \int d^f\mathbf{r} \left(\frac{\partial V_\lambda(\mathbf{r})}{\partial \lambda} \right) e^{-\beta\ H_\lambda(\mathbf{r},\mathbf{p})}. \tag{4.18}$$

The Hamiltonian is dependant on the value of λ via the potential energy with Z_λ being the corresponding partition function. This equation can be evaluated using the classical MD or quantum PIMD method, typically by performing simulations at several differing values of λ. A numerical integration can then be performed to give the free energy difference between the reference system and the system being investigated, leading to the free energy of the system of interest, as the reference is already known. In the application of this method there is one factor that must be considered, that the integration over λ must be reversible, in order for the free energy result to match up properly with the thermal equilibrium property.[54,94] This means that over the course of $\lambda = 0$ to $\lambda = 1$, there should be no first order phase transitions and the reference state should be in the same phase as the system under investigation.

The first step in the free energy calculation of ice phases is to determine a suitable reference system, a common choice for this is to use the Einstein crystal[54,92], where each molecule is attached to a fixed lattice site via a harmonic interaction with a single isotropic force constant. The free energy calculation for the Einstein crystal can be carried out analytically and therefore by using integration along a path that connects this crystal to the fully interacting solid, the free energy can be determined for the solid phase of interest. This crystal has been used as a reference state in previous work using rigid water models[92,93], where an adaptation has been made to add harmonic orientational interactions.[94] The choice of harmonic force constant is important for this model, as being too strong or too weak can lead to a large difference in the configurations of the systems visited in the two phases, which can complicate the thermodynamic integration. A method to select an appropriate force constant is to choose one that ensures a good overlap between the vibrational spectra of the crystal and the system being studied. This criteria enables the configurations visited by the two states as similar as possible due to the mean square displacement of a harmonic oscillator being inversely proportional to the strength of the force constant[54,92], this results in a smooth pathway for the integration. For rigid body water molecules it is quite simple to choose an appropriate constant, this is because the absence of high frequency intramolecular vibrations means that only intermolecular frequencies are present, which are generally lower than 1000 cm^{-1}. However by introducing a model that contains flexibility, two further vibrational contributions need to be taken into account, these are the bending mode at 1600 cm^{-1} and the stretching mode at 3600 cm^{-1}. These modes are more distinct that the librational motion, which gives rise to the idea that a different force constant should be used for each different vibrational mode. These intramolecular modes are strongly

anisotropic, an example being the amplitudes of the O-H stretching modes being largest along the O-H bonds, which is not something that would be obtained from an isotropic Einstein crystal. Therefore the reference state should have anisotropic interactions and a vibrational spectrum which closely matches the interacting solid. This can be achieved if the reference is selected to be a harmonic solid where the anisotropic force constants are derived from the Hessian matrix of the interacting system. The free energy of this Debye crystal state is close to the free energy of the fully interacting solid, allowing for a problem free thermodynamic integration. A harmonic expansion about the potential energy minimum is used to calculate the force constant for each vibrational mode, which also has the advantage of being parameter free. The Debye crystal has been used in the study of rigid body water models[171] and based on the advantages it can bring, it seems very appropriate in the use of a flexible water model and is therefore the choice we make for this work.

The thermodynamics integration of solid phases brings an additional issue that needs to be resolved, solids have a centre of mass that should be constrained for the course of the integration. This is necessary to prevent the thermodynamic integration from being divergent as $\lambda \to 1$ if the system moves to the point where it is no longer closely matched to the harmonic reference state. It is therefore imperative to add the right corrections that can account for the imposed constraint.

In the full calculation of the classical free energy of the ice phase, there are three components that combine to give the final answer

$$A^u_{ice} = A^c_{DC} + \Delta A_1 + \Delta A_2 \tag{4.19}$$

where A^c_{DC} is the energy of the constrained Debye crystal, ΔA_1 is the free energy difference between the constrained and unconstrained versions and ΔA_2 is the difference between the unconstrained ice and the Debye crystal. Each of these free energy contributions require separate calculations before combining to give the overall free energy.

4.2.3.1 Debye crystal free energy

The Debye crystal used as a reference model in this work is defined as a harmonic solid with a quartic expansion to the Hamiltonian.

$$H_{\mathrm{DC}}(\mathbf{r},\mathbf{p}) = \sum_{j=1}^{n} \frac{|\mathbf{p}_j|^2}{2m_j} + [V(\mathbf{r}_0) + \frac{1}{2}(\mathbf{r}-\mathbf{r}_0)^{\mathrm{T}}\mathbf{H}(\mathbf{r}-\mathbf{r}_0)]. \tag{4.20}$$

Here the potential energy $V(\mathbf{r}_0)$ represents the minimum-energy ice configuration with the position vector $\mathbf{r}_0$, $\mathbf{H}$ is the $3n \times 3n$ Hessian matrix with elements

$$H_{i\alpha,j\beta} = \frac{\partial^2 V(\mathbf{r})}{\partial r_{i\alpha} \partial r_{j\beta}} \tag{4.21}$$

As discussed earlier, this reference crystal moves in an anisotropic harmonic potential with force constants that are related to the potential energy of the system under investigation. As noted earlier, this ensures that the structures sampled between the two systems during the thermodynamic integration are similar, giving a numerically smooth pathway. The centre of mass is fixed and therefore the classical partition function for the reference crystal can be written as.[54,172]

$$Z_{\mathrm{DC}} = \frac{1}{(2\pi\hbar)^{3n-3}} \int d^{3n}\mathbf{p} \int d^{3n}\mathbf{r} e^{-\beta H_{\mathrm{DC}}(\mathbf{r},\mathbf{p})} \delta \left[\sum_{j=1}^{n} \mathbf{p}_j \right] \times \delta \left[\sum_{j=1}^{n} \frac{m_j}{M} (\mathbf{r}_j - \mathbf{r}_{0j}) \right], \tag{4.22}$$

where M is the total mass of the system with $\mathbf{r}_{0j}$ being the potential energy minimum of the atom of atom j. The centre of mass is enforced by the δ-functions and the momentum integral can be evaluated[54]

$$\int d^f\mathbf{p} e^{-\beta \sum_{j=1}^{n} \frac{|\mathbf{p}_j|^2}{2m_j}} \delta \left[\sum_{j=1}^{n} \mathbf{p}_j \right] = \left(\frac{\beta}{2\pi M} \right)^{3/2} \prod_{j=1}^{n} \left(\frac{2\pi m_j}{\beta} \right)^{3/2}. \tag{4.23}$$

The configurational contribution Z'_{DC} is evaluated by introducing the displacements $\epsilon = (\mathbf{r} - \mathbf{r}_0)$ and then moving into the new coordinates

$$\mathbf{q} = \mathbf{C}^{\mathrm{T}} \epsilon \tag{4.24}$$

where $\mathbf{C}$ is the $3n \times 3n$ matrix which allows the diagonalisation of the Hessian

$$\mathbf{C}^{\mathrm{T}} \mathbf{H} \mathbf{C} = \alpha \tag{4.25}$$

The matrix α is diagonal and holds the eigenvalues of the Hessian. With the transformation to new coordinates the constraint on the centre of mass also leads to a constraint on the three displacements representing possible translations of the centre of mass (q_1, q_2 and q_3), which can be spotted as they possess eigenvalues of zero. The configurational component of the Debye

crystal energy can now be computed.

$$\begin{aligned} Z'_{DC} &= \frac{1}{(2\pi\hbar)^{3n-3}} \int d^{3n}\mathbf{r} e^{-\beta[V(\mathbf{r}_0)+\frac{1}{2}(\mathbf{r}+\mathbf{r}_0)^{\mathrm{T}}\mathbf{H}(\mathbf{r}-\mathbf{r}_0)]} \delta\left[\sum_{j=1}^{n} \frac{m_j}{M}(\mathbf{r}_j - \mathbf{r}_{0j}\right] \\ &= \frac{e^{-\beta V(\mathbf{r}_0}}{(2\pi\hbar)^{3n-3}} \int d^{3n}\mathbf{q} e^{-\frac{\beta}{2}\sum_{j=1}^{3n}\alpha_j q_j^2} \delta(q_1)\delta(q_2)\delta(q_3) \\ &= \frac{e^{-\beta V(\mathbf{r}_0}}{(2\pi\hbar)^{3n-3}} \int d^{3n}\mathbf{q} e^{-\frac{\beta}{2}\sum_{j=1}^{3n}\alpha_j q_j^2} \\ &= e^{-\beta V(\mathbf{r}_0} \prod_{j=4}^{3n} \left(\frac{1}{2\pi\hbar^2\beta\alpha_j}\right)^{1/2} \end{aligned} \tag{4.26}$$

The free energy of the reference Debye crystal is therefore

$$A^{\mathrm{c}}_{\mathrm{DC}} = V(\mathbf{r}_0) - \frac{3}{2\beta}\ln\left(\frac{\beta}{2\pi M}\right) - \frac{3}{2\beta}\sum_{j=1}^{n}\ln\left(\frac{2\pi m_j}{\beta}\right) - \frac{1}{2\beta}\sum_{j=4}^{3n}\ln\left(\frac{1}{2\pi\hbar^2\beta\alpha_j}\right). \tag{4.27}$$

Due to the centre of mass constraint placed on the system the free energy obtained from this is not size extensive, however the term added because of this cancels with a corresponding term that is present in the free energy difference between the constrained and unconstrained systems.

4.2.3.2 Constrained and unconstrained ice

The free energy between the unconstrained and constrained ice systems can be shown by looking at the volume available to the centre of mass of each system and ensuring that the periodicity of the crystal is accounted for.[54,172]

$$\Delta A_1 = -\frac{1}{\beta}\ln\left(\frac{V}{N}\right) + \frac{3}{2\beta}\ln\left(\frac{\beta}{2\pi M}\right) + \frac{3}{\beta}\ln(2\pi\hbar) \tag{4.28}$$

The central term contains the mass of the system and cancels out the term in the equation mentioned earlier. The final term accounts for the fact that the two systems contain different numbers of degrees of freedom. This means that all terms containing the $(2\pi\hbar)$ cancel overall when the final free energy is calculated, which is in line with the classical treatment of the system.[54,172]

4.2.3.3 Difference between Debye crystal and ice

The difference between the Debye crystal and ice can be computed using thermodynamic integration. This provides a simple method where the λ dependent potential is

$$V_\lambda(\mathbf{r}) = \lambda[V_{es}(\mathbf{r}) + V_{dr}(\mathbf{r}) + V_{intra}(\mathbf{r})] + (1-\lambda)V_{\mathrm{DC}}(\mathbf{r}). \tag{4.29}$$

Here, V_{DC} is the potential energy of the Debye crystal, V_{dr} is the dispersion-repulsion energy and V_{LJ} is the interaction energy of LJ sites positioned on each water molecule at the centre of mass. As λ increases from 0 to 1 the centre of mass shifts from the molecular centre towards the oxygen atoms. The $\lambda V_{es}(\mathbf{r})$ term is responsible for switching on the partial charge interactions between water molecules. This leads to

$$\frac{\partial V_{\lambda(\mathbf{r})}}{\partial \lambda} = V_{es}(\mathbf{r}) + V_{dr}(\mathbf{r}) + V_{intra}(\mathbf{r}) - V_{\mathrm{DC}}(\mathbf{r}), \tag{4.30}$$

therefore the free energy difference between the fully interacting system and the Debye crystal is

$$\Delta A_2 = \int_0^1 \langle V_{es}(\mathbf{r}) + V_{dr}(\mathbf{r}) + V_{intra}(\mathbf{r}) - V_{\mathrm{DC}}(\mathbf{r})\rangle_\lambda d\lambda. \tag{4.31}$$

As the order parameter moves $0 \rightarrow 1$, the potential energy of the Debye crystal is gradually replaced by the potential energy of the fully interacting ice system. We can therefore say that the calculation of the free energy depends on two separate calculations. First the calculation of the Debye crystal free energy along with the correction for the centre of mass constraint and second, the calculation of the energy difference between the fully interacting system and the Debye crystal. It should be noted that both of these calculations are performed with an appropriate volume, which can be determined in a prior constant pressure simulation before the free energy is calculated.

4.2.4 Liquid Phases

While we have talked about using a solid reference state for the calculation of the free energy of ice, the same reference would not be appropriate for a liquid, where it makes more sense to use a reference state in the liquid phase. An ideal candidate for this is the LJ fluid, which has been examined over a large range of temperatures.[173] The only drawback to this is that water is a molecular fluid, so a consideration needs to be made for the intramolecular component of the free energy. With the assumption that the intermolecular interaction sites are at the centre of mass of the molecules, the partition function can be separated into different contributions based on the different motions of the system, which include the centre of mass motion and the ro-vibrational motion.

$$Z = Z_{\text{inter}} Z_{\text{intra}} = Z_{\text{inter}} (Z_{\text{mol}})^N \tag{4.32}$$

However the water model we use in this work (q-TIP4P/F) is not so simple as the intermolecular interactions are not fixed at the centre of mass, but instead spread over the three water molecules. The LJ interaction in this water model is on the oxygen atom of each individual molecule, with partial charges accounting for the intermolecular Coulomb interactions between hydrogen atoms and the M-sites, which take up a position a short distance from each oxygen atom.[21] Thermodynamic integration is used to deal with this issue by calculating the free energy difference between the fully interacting liquid system and the fixed centre of mass reference system. The centre of mass sites interact solely by LJ which allows the calculation of the Helmholtz free energy for this free energy computation.[173] The vibrational component to this free energy (ro-vibrational) can be evaluated using direct integration of the appropriate partition function. The free energy of liquid water at a fixed volume and temperature can be written as

$$A_{\text{liq}} = A_{\text{LJ}} + N A_{\text{mol}} + \Delta A_{\text{liq}} \tag{4.33}$$

A_{LJ} is the free energy for a system of N molecules interacting with only LJ sites at the centre of mass of each individual molecule. A_{mol} is the free energy of a single molecule of water that is rotating and vibrating freely about its centre of mass. ΔA_{liq} is the difference in free energy between the reference system and the full liquid. There is no translational motion in this equation, instead this is captured by the ideal gas contribution.

4.2.4.1 LJ reference system

The free energy of the LJ system can be written as

$$A_{\text{LJ}} = A^{\text{id}} + A^{\text{ex}}_{\text{LJ}}, \tag{4.34}$$

where the free energy of an ideal gas is represented by A^{id} and $A^{\text{ex}}_{\text{LJ}}$ is the excess free energy of the LJ system. We can now define the excess free energy for N molecules with molar mass m_{mol}, volume V and reciprocal temperature ($\beta = 1/k_B T$) as

$$A^{\text{id}} = -\frac{N}{\beta} \ln \left[\frac{V}{N} \left(\frac{m_{\text{mol}}}{2\pi\beta\hbar^2} \right)^{3/2} \right] - \frac{N}{\beta} + \frac{1}{2\beta} \ln(2\pi N) \tag{4.35}$$

where the indistiguishability of molecules in the gas phase is now accounted for. The excess free energy of the system is available in an analytical expression using parameters obtained from a simulation.

4.2.4.2 Ro-vibrational free energy of a water molecule

For a water molecule that has free rotational and vibrational motion, but no translational motion, the classical partition function can be written (using Jacobi coordinates) as

$$\begin{aligned} Z_{\text{mol}} &= \frac{1}{2(2\pi\hbar)^6}\int d\mathbf{P}\int d\mathbf{p}\int d\mathbf{R}\int d\mathbf{r} e^{-\beta[|\mathbf{P}|^2/2\mu_{\text{R}}+|\mathbf{p}^2/2\mu_r+V_{\text{intra}}(\mathbf{R},\mathbf{r})]} \\ &\equiv \frac{1}{2(2\pi\hbar)^6}\left(\frac{4\pi^2\mu_{\text{R}}\mu_{\text{r}}}{\beta^2}\right)^{3/2}\int d\mathbf{R}\int d\mathbf{r} e^{-\beta V_{\text{intra}}(\mathbf{R},\mathbf{r})}, \end{aligned} \tag{4.36}$$

where $\mathbf{R}$ is a vector from the oxygen to the centre of mass of each hydrogen atom, $\mathbf{r}$ is the vector between the hydrogen atoms, with reduced masses $\mu_{\text{R}} = 2m_{\text{O}}m_{\text{H}}/(m_{\text{O}}+2m_{\text{H}})$ and $\mu_{\text{r}} = m_{\text{H}}/2$. The factor of two in this equation arises from the fact that hydrogen atoms in a molecule of water are indistinguishable due to symmetry. The intramolecular component is independent of the Euler angles that define the molecules orientation, these integrals can therefore be evaluated directly

$$Z_{\text{mol}} = \frac{8\pi^2}{2(2\pi\hbar)^6}\left(\frac{4\pi^2\mu_{\text{R}}\mu_{\text{r}}}{\beta^2}\right)^{3/2}\times\int_0^\infty R^2dR\int_0^\infty r^2dr\int_0^n \sin\gamma d\gamma e^{-\beta V_{\text{intra}}(R,r,\gamma)} \tag{4.37}$$

where R and r are the lengths of $\mathbf{R}$ and $\mathbf{r}$, with γ representing the angle between them. The remaining integrals require quadrature to solve as they cannot be done analytically. However this is not a problem as the intramolecular energy can be found computationally very fast for empirical water models such as the q-TIP4P/F model used in this work. The classical ro-vibrational free energy for a simple molecule such as water is therefore easy to calculate.

4.2.4.3 Free energy difference between interacting and reference system

The final component that needs to be considered is the difference between the fully interacting system and the reference system. This can be done using the thermodynamic integration method by adding the λ term into the potential energy.

$$V_\lambda(\mathbf{r}) = \lambda V_{\mathrm{dr}}(\mathbf{r}) + (1-\lambda)V_{\mathrm{LJ}}(\mathbf{r}) + V_{\mathrm{intra}}(\mathbf{r}) \tag{4.38}$$

Here we introduce $V_{\mathrm{dr}}(\mathbf{r})$ as the dispersion repulsion energy of the fully interacting system with V_{LJ} being the interaction energy between the LJ sites at the center of mass of each water molecule. As $\lambda \to 1$ the interaction sites are shifted from the centre of mass to the oxygen atoms. The differentiation of this equation with respect to λ gives

$$\frac{\partial V_\lambda(\mathbf{r})}{\partial \lambda} = V_{\mathrm{es}}(\mathbf{r}) + V_{\mathrm{dr}}(\mathbf{r}) - V_{\mathrm{LJ}}(\mathbf{r}) \tag{4.39}$$

therefore the free energy difference can be evaluated as

$$\Delta A_{\mathrm{liq}} = \int_0^1 \langle V_{\mathrm{es}}(\mathbf{r}) + V_{\mathrm{dr}}(\mathbf{r}) - V_{\mathrm{LJ}}(\mathbf{r})\rangle_\lambda d\lambda \tag{4.40}$$

In this derivation it is only the intermolecular component that is different in terms of potential. The intramolecular component is identical in both the fully interacting and reference system. As before, the thermodynamic integration is performed under constant NVT conditions after the prior determination of the volume of the simulation box.

4.2.5 Quantum correction to the free energy

The methods discussed above are used to obtain classical free energies of liquid and solid water phases. However this does not involve any form of quantum effects, which could be of vital importance when investigating the stability of the systems in this work. Therefore a method is required that allows for the calculation of the free energy that accounts fully for NQEs. This is done by using the PIMD method discussed in earlier chapters. Specifically, thermodynamic integration is performed using the isothermal-isobaric ensemble along the order parameter λ, which connects the fully classical description of the system to the fully quantum PIMD system. The free energy calculated in this way is then added to the already known classical free energy in order to obtain the full quantum free energy. Therefore the total quantum free energy relies on the energy of the reference crystal, the classical thermodynamic integration components discussed above and a quantum correction calculated by thermodynamic integration.

$$A = A_{\mathrm{RS}} + A_{\mathrm{Cl}} + A_{\mathrm{QC}} \tag{4.41}$$

where A_{RS} is the free energy of the reference system, A_{Cl} is the classical correction and A_{QC} is the quantum correction. These classical and quantum simulations give the exact free energy of the liquid and ice structures for the q-TIP4P/F water model with all configurational sampling, anharmonicity and NQEs fully accounted for in this work.

4.2.6 Simulation Details

All simulations performed in this work used a system size of 432 water molecules for both ice polymorphs ($\mathrm{I_h}$ and $\mathrm{I_c}$), stacking faulted ice phases and liquid water. This system size was chosen as it ensures that it is large enough to enable averaging over a large number of proton orderings in a single simulation cell, the size also enabled the system size generated to be near cubic for both ice polymorphs. This relatively large system size also minimizes finite size effects and artificial differences from different cell morphologies. As in previous work presented here using the q-TIP4P/F water model[21], the LJ interactions were cut off at a distance of 9 Å, and the Ewald summation method was used to evaluate Coulomb interactions. The q-TIP4P/F water model is well suited for this work and it is parameterised such that many experimental observables such as RDFs, diffusion coefficients and infrared vibrational frequencies are reproduced when using the model in quantum simulations. Additionally this model also gives a good representation of properties that were not included in the original parameterisation, these include the melting point of $\mathrm{I_h}$ and the liquid density anomaly. One property that is highly relevant to this work is the idea that this model has competition between the inter- and intramolecular NQEs, which explains how the model is able to account for these quantum effects in properties such as diffusion coefficient and solvent exchange around ion shells.

The classical and quantum mechanical free energies of $\mathrm{I_h}$ and $\mathrm{I_c}$ stacking disordered phases and liquid water were calculated at six different temperatures (T = 200, 210, 220, 230, 240, 250 K). The initial densities (ρ) of both ice polymorphs was set as 0.93 g $\mathrm{cm^{-3}}$ and the initial simulation box lengths were 50.991 Å, 44.160 Å and 41.638 Å for $\mathrm{I_h}$ and 50.996 Å, 44.163 Å and 41.634 Å for $\mathrm{I_c}$. Oxygen atoms were arranged on standard $\mathrm{I_h}$ and $\mathrm{I_c}$ lattices, with hydrogen atoms placed according to the Bernal-Fowler ice rules using the Buch algorithm. A pressure of 1 bar using the Berendsen barostat was enforced and an Andersen thermostat used for temperature control. All simulations were performed three times, with each one beginning from a different initial proton disordered configuration, the results presented here are averages of

the independent runs. Liquid phase free energy calculations were performed in the same way as described above, however the density was set as 0.997 g cm^{-3}.

4.2.6.1 Classical free energy calculations

In all classical free energy calculations, an initial equilibration of the systems (I_h, I_c and liquid) was carried out using an isothermal-isobaric ensemble for 50 ps. The average box lengths were then averaged over a further 50 ps of time under the same conditions. The average box lengths from this were then used to calculate the free energy. This was done by determining the Debye crystal free energy as the reference state and then the evaluation of the thermodynamic integration from this reference system to the fully interacting q-TIP4P/F model. This can be done in the standard anharmonic way or harmonically, allowing for another basis for comparison. The Debye crystal reference free energy was computed after optimisation of the atomic coordinates at a fixed cell geometry using a conjugate gradient minimization method. The thermodynamic integration was performed numerically using 10 Gauss-Legendre integration points. For each point, the system was equilibrated for 20 ps and then the free energy derivative averaged over 50 ps.

4.2.6.2 Quantum free energy calculations

Quantum free energy calculations were performed by thermodynamic integration from the fully classical description to the fully quantum description. This correction is then added to the classical free energy to give the total quantum free energy of the system. This approach employs the PIMD method to numerically evaluate the free energy difference along a path that connects the classical and quantum descriptions of the same molecular system. Beginning with the classical ice structures, a 10 point Gauss-Legendre integration is used to calculate the classical to quantum free energy difference. At each of these points the system was equilibrated for 20 ps under the isothermal-isobaric ensemble, with the free energy derivative averaged over a further 50 ps of simulation time. In all these PIMD calculations, 32 ring polymer beads were used in the PI description of the system and the RPC method was used to accelerate these simulations.

4.2.6.3 Error estimates

The standard error in the mean of the three independent evaluations of each free energy component was used for the error estimate. The errors on the

final free energy were calculated by standard error propagation applied to the errors on the individual components.

As an example, the classical free energy A_{cl} depends on the summation of three parts,

$$A_{cl} = A_{DC} + \Delta A_1 + \Delta A_2 \tag{4.42}$$

the Debye crystal energy, A_{DC}, the free energy difference between constrained and unconstrained ice, ΔA_1, and the free energy difference between the Debye crystal and ice, ΔA_2 (calculated by thermodynamic integration). All of these values were averaged over 3 simulations to give the final result and therefore all have an error associated with them. The error in each term was defined as the standard error,

$$\sigma_{\bar{x}} = \frac{\sigma}{\sqrt{n}} \tag{4.43}$$

where n is the number of values and σ is the standard deviation,

$$\sigma = \sqrt{\frac{\sum_{i=1}^{i}(x_i - \bar{x})^2}{n}}. \tag{4.44}$$

Once we have calculated our standard error for each component, the error in the total energy can be evaluated by standard error propagation,

$$\sigma_{A_{cl}} = \sqrt{(\sigma_{A_{DC}})^2 + (\sigma_{\Delta A_1})^2 + (\sigma_{\Delta A_2})^2} \tag{4.45}$$

where $\sigma_{A_{cl}}$ is the error in the classical free energy.

4.3 Free energy results

4.3.1 I_h and I_c

The free energies for I_h and I_c were calculated over a range of temperatures between 200 K and 250 K in classical and quantum simulations using the standard anharmonic form of the the q-TIP4P/F model as well as a modified harmonic version. The results for all these variations are shown in Fig 4.2. In the standard anharmonic q-TIP4P/F model (Fig 4.2 (panel a)), there are a number of things of interest to note. In the case of the classical free energy difference, I_h is more stable than I_c by approximately 10 J mol^{-1} across all temperatures studied, the conclusion from this is that the q-TIP4P/F model finds that I_h is more stable than I_c although this free energy difference is smaller than the expected ≈30-150 J mol^{-1} range.[99,158–160] More importantly, the quantum-mechanical free energy difference between I_h and I_c is much larger than the classical result, indicating that the inclusion of NQEs gives rise to a greater stabilisation for I_h compared to I_c, with the stabilisation being up to 30 J mol^{-1}. This additional stability brings the calculated free energy difference much closer to the order of magnitude expected based on experimental estimations. This observation should be emphasized as while classical simulations are accurate in predicting I_h as more stable than I_c, the difference is very small and only slightly in favour of $I_h$whereas our simulations show for the first time that NQEs play a large role in the determination of the stability of the two ice polymorphs. Another thing to note is that the free energy differences between different proton configurations is of the order 5-10 J mol^{-1} for both I_h and I_c, with the stabilising effect of the NQEs being more significant than the differences due to different proton configurations. In order to answer the question of why NQEs provide this stabilisation, it is prudent to first consider the role of anharmonicity in the free energy values. Previous PI simulations of aqueous systems have shown that harmonic and anharmonic interaction models can give rise to very different behaviours in predicted physical properties, in particular when NQEs play an important role.[21,25,41,42] Recent simulations have also suggested that vibrational anharmonicity in the higher frequency O-H modes serves to stabilise I_h over I_c.[99] Investigating the role of the higher frequency O-H anharmonic stretch in our simulations is straight forward as the intramolecular potential energy term term in the q-TIP4P/F employs all terms up to fourth-order in the O-H bond distance, therefore we can derive a corresponding harmonic model by simply truncating this expansion at the quadratic term. The use of this harmonic

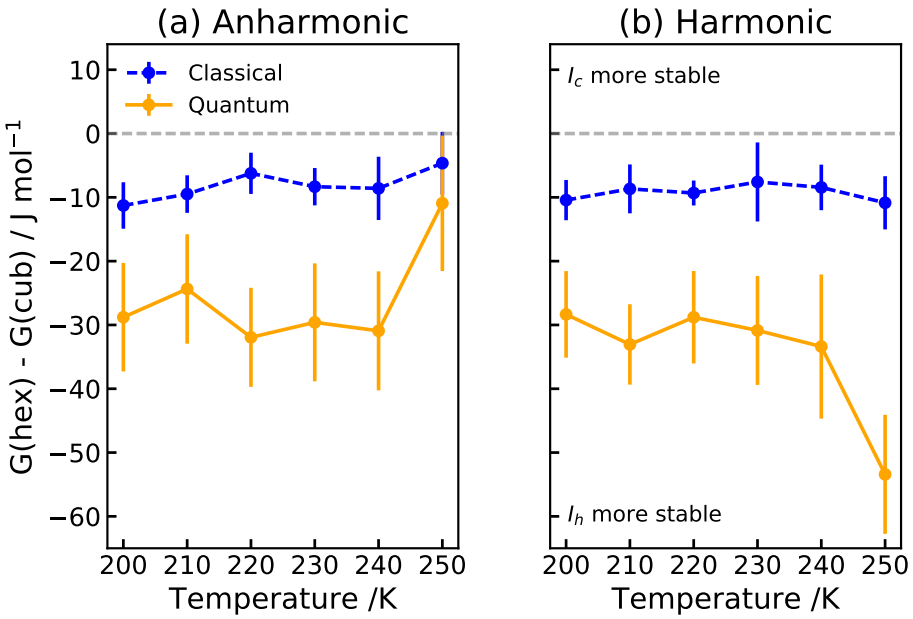

Figure 4.2: (a) Free energy difference between I_h and I_c calculated in classical and quantum mechanical simulations of anharmonic liquid water using the q-TIP4P/F model. (b) Free energy difference between I_h and I_c calculated in classical and quantum mechanical simulations of a harmonic variant of the q-TIP4P/F water model, where the intramolecular O-H stretching term is truncated at quadratic level. In both panels a negative free energy difference corresponds to I_h being more thermodynamically stable than I_c. The errors represent one standard error in the free energy values calculated for the three different proton-disordered configurations used in each calculation.

model gives the results in Fig 4.2 (panel b).

From these results it can be seen that the relative free energies of I_h and I_c are essentially unchanged relative to the fully anharmonic q-TIP4P/F model, which suggests that the O-H anharmonicity plays no significant role in our simulations. One key difference between this work and others that investigate the role of anharmonicity is the type of model used in the study. In this work we use an empirical forcefield whereas other work has employed DFT with a PBE exchange-correlation functional. It is well known that the PBE functional 'overbinds' molecules in hydrogen bonded systems[105], an example of this can be seen in the liquid water RDFs computed using PBE, where the result is strongly over-structured.[105,174] As well as this, the diffusion coefficient is predicted to be much smaller than expected. By contrast, the q-TIP4P/F model is well established and gives a good description of liquid water, with the density, diffusion coefficients and RDFs all behaving correctly and the quantum melting point of I_h being only 22 K lower than experiment. With specific regard to the vibrational contributions to the free energy, the PBE

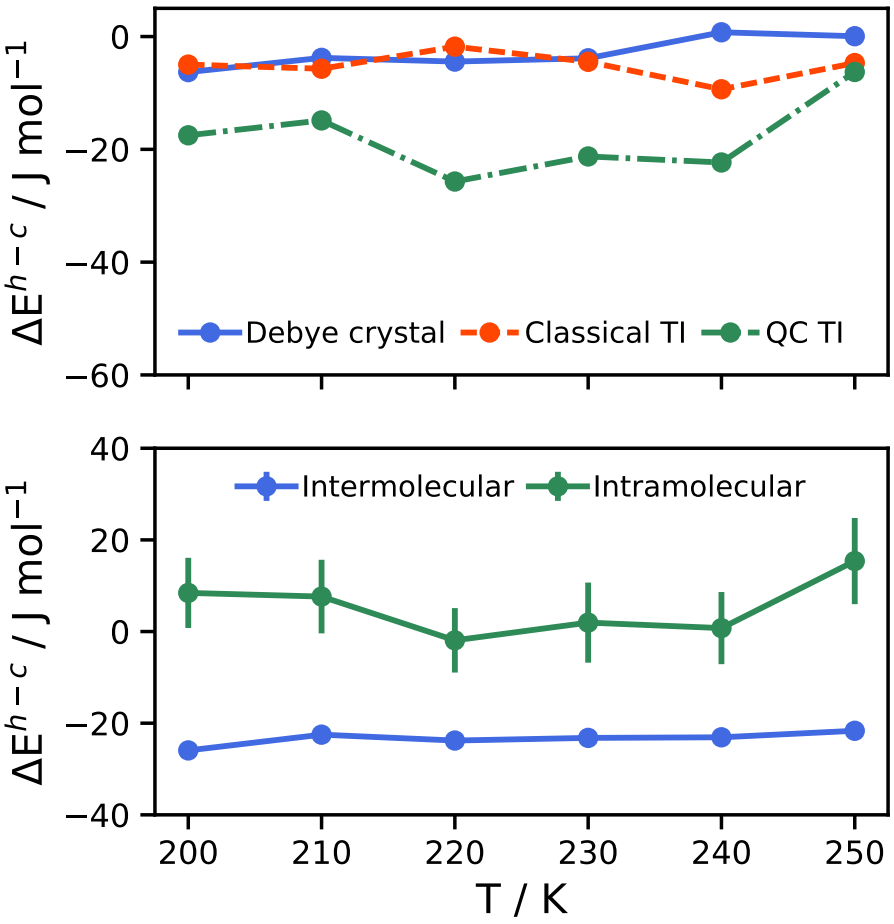

Figure 4.3: (Upper) Major contributions to the free energy difference between I_h and I_c. The Debye crystal and classical thermodynamic integration contributions are summed to calculate the classical free energy with the addition of the quantum-classical term leading to the quantum free energy. (Lower) The quantum to classical term can be further broken down into contributions from the inter- and intramolecular energy, the most important contribution is from changes in the intermolecular term.

functional is known to give a poor reproduction of vibrational frequencies in hydrogen bonded clusters. A comparison of this method with CCSD(T) benchmarks shows that the PBE frequencies have an error by 100 cm[1] on average.[175] One final point of contrast between these methods lies in that the potential used in this work gives the exact classical and quantum free energies as well as the explicit correlation between all molecules in the system and the correlation between the configuration of the system and the unit cell, whereas in the case of VSCF-type calculations used in conjunction with DFT calculations out of necessity, intermode coupling is captured in a mean field

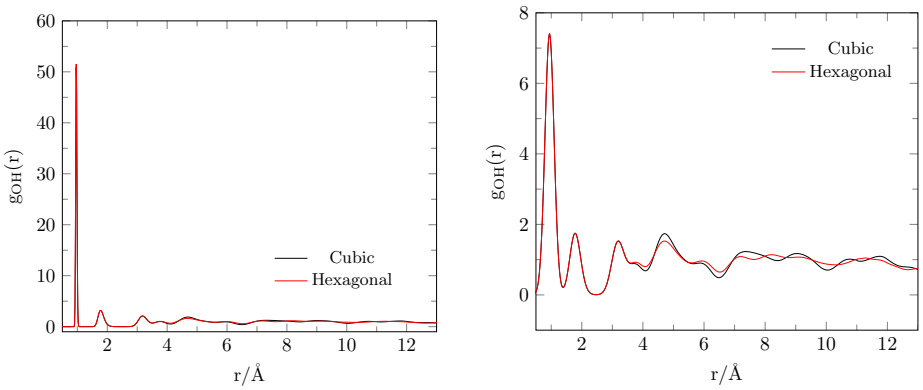

Figure 4.4: O-H RDFs for the classical and quantum I_h and I_c systems. In both cases the short range structure is almost identical for both. However differences begin to appear in the long range structure.

or perturbative treatment.[176]

Overall our simulations along with the discussion about anharmonicity and interactions models above suggest that there is another explanation for the stabilisation of I_h over I_c. Specifically the results obtained in this work predict that NQEs play an important role. To illustrate this, the free energy results obtained have been split into the independent contributions that make up the total free energy, these being the Debye crystal energy, the classical thermodynamic integration and the quantum mechanical correction to the free energy, these contributions are plotted in Fig 4.3 (Upper). It is clear from the individual contributions that moving from a classical to a quantum mechanical description of the system gives the most stabilisation for I_h over I_c. Giving a stabilisation of approximately 30 J mol^{-1} on top of the 10 J mol^{-1} from just the classical treatment. In addition to this, the quantum correction to the free energy can be split into components relating to the intermolecular and intramolecular components. These results are shown in Fig 4.3 (Lower) and clearly show that the stabilisation given by introducing NQEs comes from the intermolecular interaction terms. This suggests that these effects induce changes in the structure of the two polymorphs so that the intermolecular interactions in I_h are stabilised relative to I_c.

The role of these NQEs in modifying the intermolecular interactions in the two polymorphs can be understood and explained by considering the molecular geometries of the water molecules when changing from a classical to a quantum mechanical description. These details are shown in Fig 4.5 where we compare the difference between the classical and quantum treatments in terms of the O-H RDF, the bond angle and the molecular dipole distribution. With the full RDFs shown in Fig 4.4. The classical results show that there are

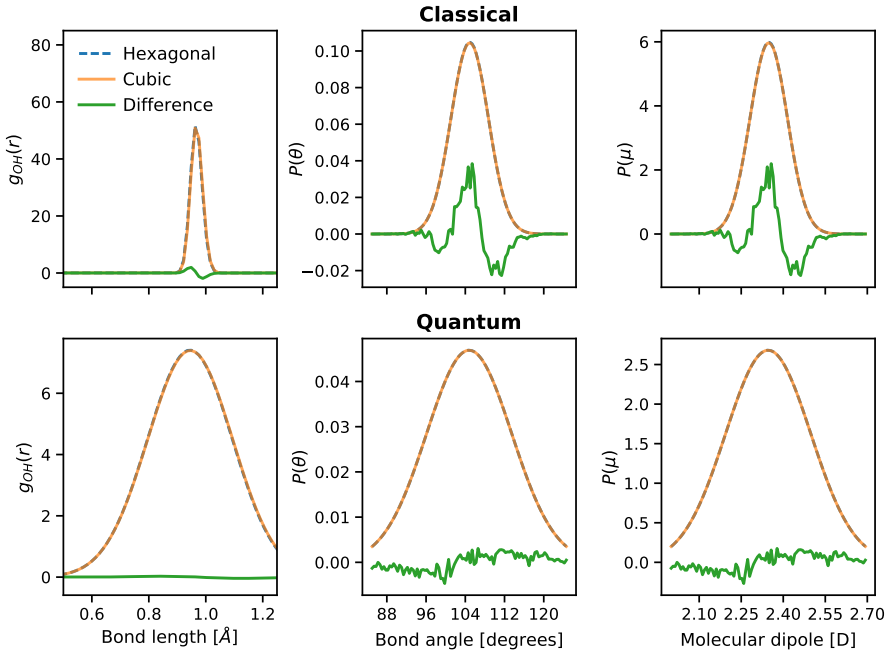

Figure 4.5: Calculated O-H RDFs (left), H-O-H bond angle distribution (center) and molecular dipole momentum distribution (right) determined in classical (top panels) and quantum (bottom panels) simulations. In each case, the distributions are shown for I_h and I_c. The difference between the two polymorphs is also illustrated. In the case of the bond angle and dipole distributions, the difference distribution is scaled by a factor of 100 for clarity

small differences in the geometry of the two polymorphs. In the intramolecular part of the O-H RDF, the difference between the two shows a shift to smaller O-H bond lengths in I_h, although we also find that the change in the average bond length is similar in size to the associated error bars in the simulation results. In the case of the bond angle distribution the classical results show that there is a small probability of adopting a bond angle close to $\approx 110^o$ and $\approx 100^o$ in I_c. However this is not even, with the bond angle of $\approx 110^o$ being much more strongly preferred. This is not a surprise as the structure of I_c is arranged so that the O-O-O bond angles prefer the ideal tetrahedral arrangement of 109.47^o as in a structure like diamond. This means that there is a tendency for the molecules in I_c to tend towards higher bond angles than seen in the I_h polymorph. This observation can also be seen in the molecular dipole moment, which is dependent on both the O-H bond length and the H-O-H bond angle. The molecular dipole distribution is identical in shape and symmetry to the bond angle distribution, which indicates that the changes in the bond angle are entirely responsible to changes in the molecular dipole. The overall trend of the dipoles therefore shows a tendency for the dipole to

shift to larger values in I_c than in I_h. As the dipole moment can be used as a guide for the strength of intermolecular interactions in water models like q-TIP4P/F used here, it can be concluded that the flexibility of this model gives rise to a slight strengthening of the instantaneous intermolecular interactions in I_c when compared to I_h. However based on the data in Fig 4.5, it should be noted that the overall stability of I_h is still greater than I_c due to the Debye crystal and classical thermodynamic integraton terms in purely classical simulations.

Examining the quantum mechanical results from Fig 4.5 shows distinct differences in the properties under investigation when compared to the classical results. The differences in all three properties are all effectively 'washed out' by the inclusion of NQEs. This occurs because of the effect that NQEs have on intermolecular hydrogen bonding, which are weakened when ZPE is included.[20–22] This inclusion outweighs the free energy gained when larger than usual bond angles are adopted in the I_c polymorph, the result being that this effect is simply not present in simulations that fully account for NQEs. Overall this leads to a slight destabilisation of I_c which leads to the overall result seen in Fig 4.5 where I_h is stabilised over I_c.

The impact on the intermolecular energies when NQEs are included can be visualised by examining how different dimers within the two ice structures interact, the results from this are shown in Fig 4.6. This shows the results of 5×10^6 dimer configurations taken from classical or quantum PIMD simulations. Where dimers were taken from PIMD simulations, the coordinates of a single ring-polymer bead were extracted. The intermolecular interaction energy was calculated for each dimer, with panels A and B showing the quantum-classical difference between the distributions in I_h and I_c respectively, plotted as a function of O-O distance and energy. For I_c, these results show that the change in the intermolecular interaction energy upon quantization is quite small, with the difference distribution being relatively featureless across the entire range of study. However when examining the results for I_h, there are clear features that suggest changes in the intermolecular interaction energy distribution in both short and long-range dimer pairs. As an example, the O-O distances up until 5Å show an increase in intermolecular interactions at low energy, meaning that the inclusion of NQEs slightly increases the intermolecular interactions between molecules in the first and second coordination shells. At first glance this seems counter-intuitive, as the inclusion of NQE are known to decrease the strength of hydrogen-bonds. However, in the two ice crystal structures, the near neighbour interactions are modulated by the longer range interactions which have an impact on the intermolecular inter-

action energy of a dimer pair. As an example, taking the case of a nearest neighbour hydrogen bonded dimer, the strength of interaction will be modified by other interactions with the next nearest neighbour water molecules. This added complexity is clearly evident in panel A of Fig 4.6, where it is seen that a pattern of changes in dimer interaction strengths is observed between $5 - 6$Å. This distance range corresponds to the second nearest neighbour water molecules and beyond. To understand where these changes come from, we can look back at the H-H RDFs shown earlier, for simplicity, the relevant parts are shown in Fig 4.6 panels C and D. As previous work has shown, the two ice polymorphs have different local hydrogen bonding environments characterised by the presence of 'chair' and 'boat' conformations, which can give rise to distinctive H-H RDFs beyond the first coordination shell. This can be seen in panels C and D of Fig 4.6, where the classical RDFs have some differences in structure which can be attributed to these two different conformations. However when NQEs are included, these features are largely 'washed out' in both structures. The result of this is that the dimer difference distributions in the upper panels are not related to a large individual change in structure, but instead are a consequence of small hydrogen bonding changes that propagate through the structure.

Overall these results suggest that quantum effects play a very important role in the difference between the two polymorphs, with I_h being more stable than I_c and thereby contributing to the observation that I_c is never observed under terrestrial conditions. While purely classical simulations suggest that I_c is stabilised by a preference for optimal tetrahedral bond angles giving rise to stronger intermolecular interactions, the inclusion of quantum effects removes this preference and destabilises I_c relative to I_h. Further examination showed that these differences also arise due to the subtle difference in hydrogen bonding when NQEs are included. This effect is only seen in simulations where it is possible to account fully for NQEs and is not seen in work which uses harmonic or quasi-harmonic calculations. This work supports the idea that quantum effects play a very important role in modifying molecular geometries and intermolecular interactions.

4.3.2 Stacking disordered ice

In addition to the study of pure I_h and I_c phases, there also exist a variety of stacking disordered phases that lie between I_h and I_c. These can be formed by vapour deposition in the Earth's atmosphere or in extraterrestrial environments over a wide temperature range up to the melting point. These stacking

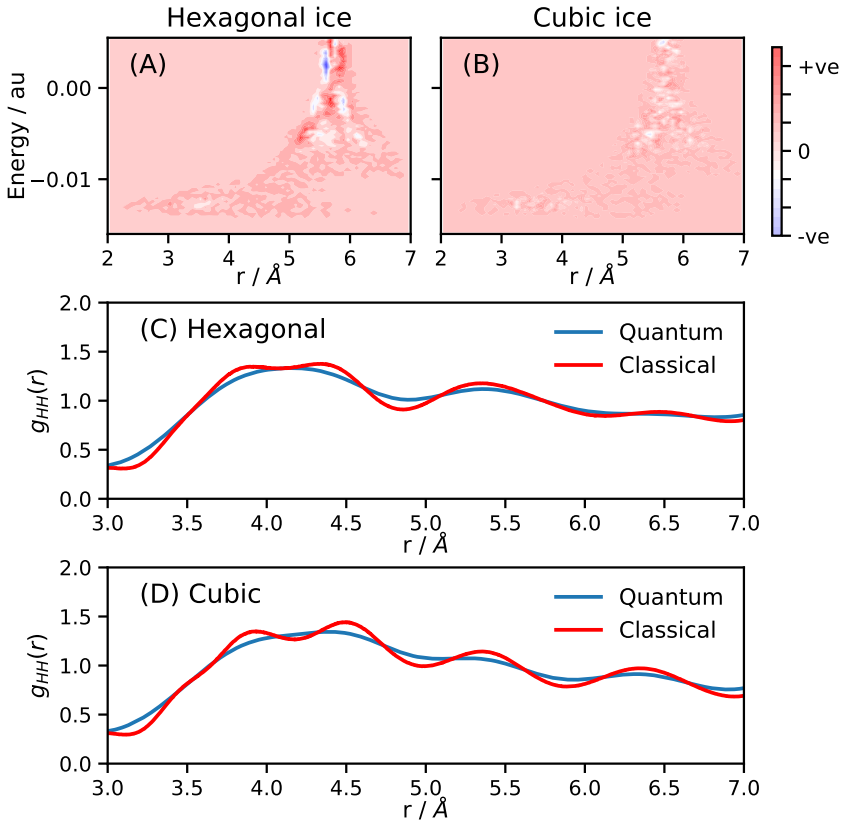

Figure 4.6: Quantum-Classical difference in dimer interaction energy distributions in I_h. (B) Quantum-Classical difference in dimer interaction energy distributions in I_c. (C) H-H RDFs from classical simulations of I_h and I_c. (D) H-H RDFs from quantum (PIMD) simulations of Ih and Ic.

disordered phases consist of I_h and I_c layers in varying degrees depending on the temperature and pressure of the system and all eventually transform into pure I_h. In this work we examine 5 different variations of stacking disordered ice to see how they compare to the two pure phases and how NQEs and anharmonicity play a role in the ordering of their free energies. These stacking disordered phases are defined by their stacking pattern, the five studied in this work are (ABABCB, ABACBC, ABCACB, ABCBAB and ABCBCB). These are shown in Fig 4.7 along with descriptors showing how the stacking pattern varies between hexagonal and cubic. There are varying degrees of cubicity in these phases with three of the phases being 1/3rd cubic ice and two others being 2/3rds cubic ice, with the cubic layers positioned differently. The simulations were carried out in a similar way to pure I_h and I_c, with classical free energies computed followed by the quantum correction to the free energy. Results for each stacking disordered phase were averaged over

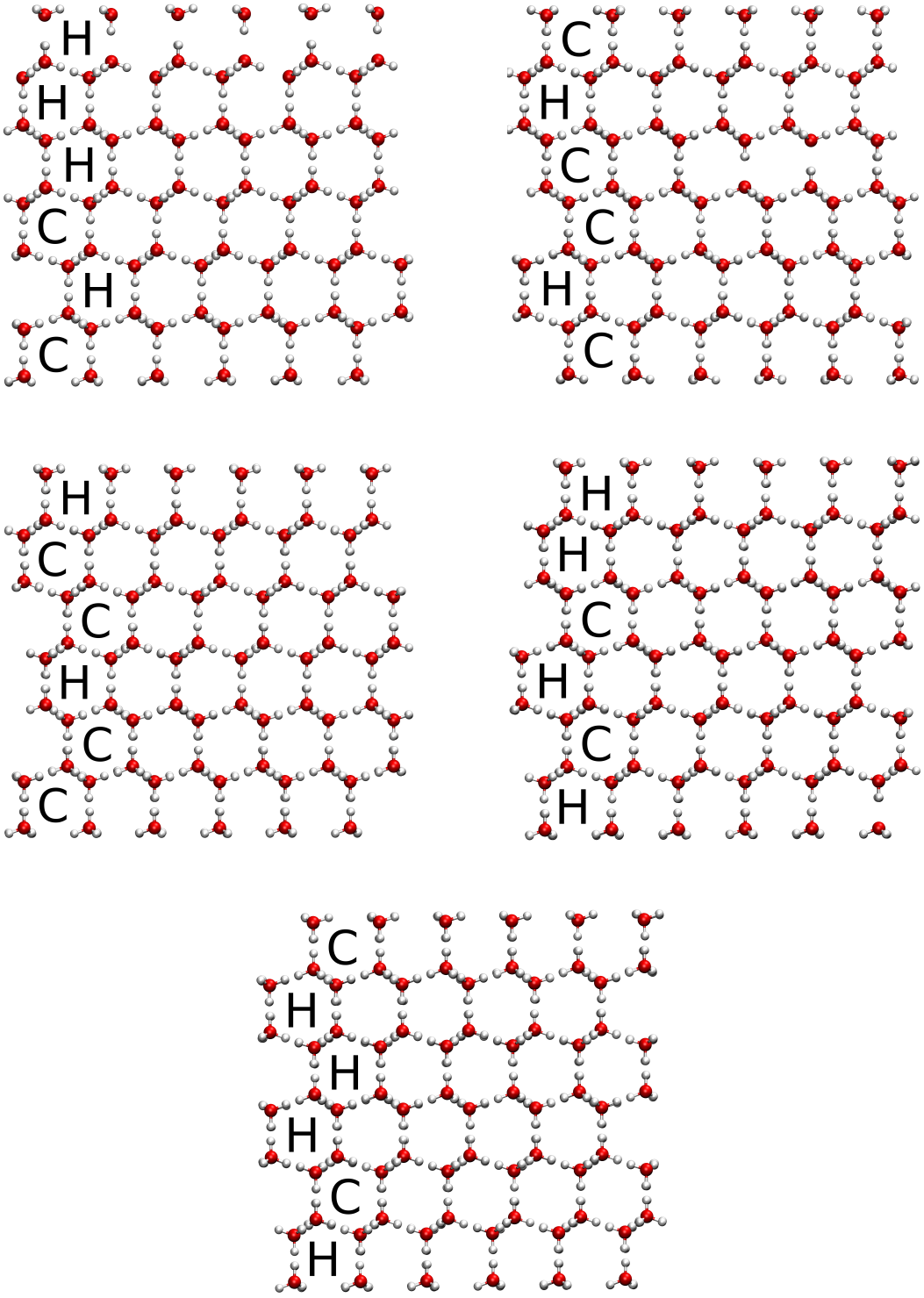

Figure 4.7: Illustration of the 5 stacking disordered structures being studied as a cross Section through the 432 molecule simulation box. These are (from top left to bottom right) ABABCB, ABACBC, ABCACB, ABCBAB, ABCBCB. Each structure has labelling for each type of layer present, H representing I_h and C representing I_c.

three separate simulations to improve accuracy.

These free energy results allow these phases to be compared to pure I_h

and I_c in order to discover what effect stacking faults have on the overall free energy with respect to the most stable I_h form. This allows an insight into how big a difference a small stacking fault has compared to a larger one, with additional comparison being how NQEs can affect this amount of stability provided by diminishing cubic phases. With these unit cells it is not possible to obtain a configuration that is for example 1/6 cubic ice as the creation of one solitary cubic ice layer is not possible without creating another at some point in the unit cell due to the stacking properties of the system. As well as the investigation of quantum effects, the systems were also investigated using an anharmonic and a harmonic q-TIP4P/F water potential. These results are shown in Figs 4.8 and 4.9.

The first thing of note in both sets of data is that the pure I_c phase is the least stable with respect to I_h, this is expected as stacking disordered ice contains some hexagonal stacking, giving it extra stabilisation relative to I_c. Another feature in both panels is that some of the stacking disordered phases seem to have a positive free energy difference, which would suggest that they are more stable than pure I_h however it should be noted that the error bars for these values, while not shown for the sake of clarity, have a range that extends into the negative free energy difference. Therefore it is most likely that the actual free energy difference for these points while close to that of I_h, is still less stable. In the classical data there is a clear ordering of stacking disordered ice as one moves from the I_c results up. The stacking disordered phases that contain the most I_c are next (ABACBC and ABCACB) followed by the three phases that contain the lesser amount of I_c (ABCBCB, ABABCB and ABCBAB). This confirms that the amount of I_c present in a stacking disordered phase directly affects its overall stability and phases with a small amount of I_c will be longer lived and more likely to form naturally before they transform into pure I_h. This is further supported by the results that show some of the phases are very close to the level of stability (within error bars) of I_h. When quantum effects are included, this picture become much less clear. We still observe the lowest stability in I_c however the stacking disordered phases overlap far more and clear ordering is more difficult to spot. Overall the stacking disordered phases do not alter the order from the classical panel but instead are more erratic with temperature changes and overlap and change ordering more frequently. The inclusion of NQEs also noticeably stabilises the I_h phase with respect to all the others. This can be understood in the same way as described above with the I_h and I_c polymorphs. The addition of NQEs 'washes out' the tetrahedral stability of the classical cubic ice and causes it to be destabilised. By extension this means that stacking disordered

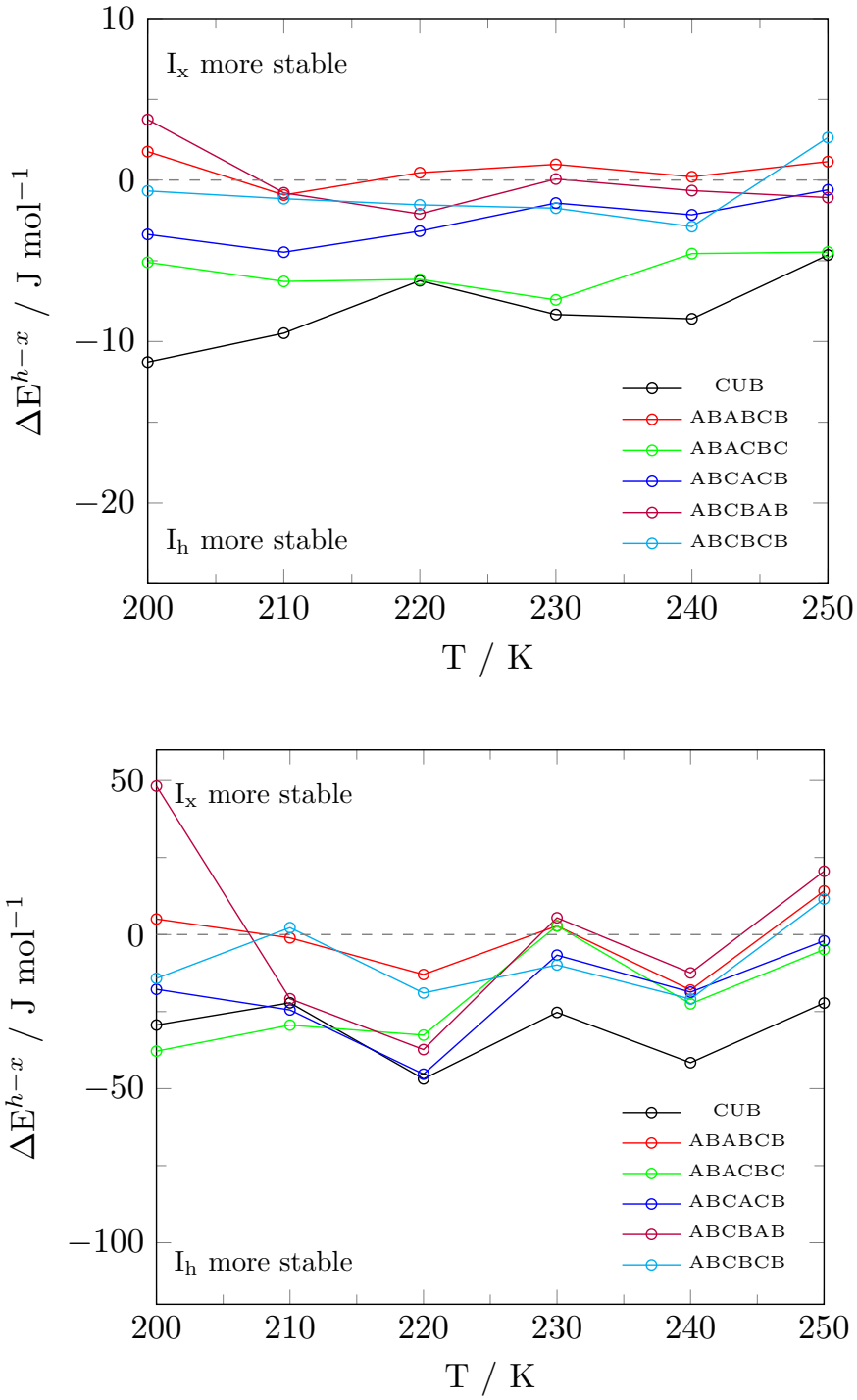

Figure 4.8: Free energy difference between I_h, I_c and the 5 stacking disordered variations, calculated using classical (top) and quantum (bottom) simulations of water using the *anharmonic* version of the q-TIP4P/F water potential. A negative free energy difference indicates that I_h is more stable and a positive free energy difference indicates the relevant ice phase is more stable. Error bars are not shown for clarity.

phases suffer the same 'washing out' of stability in the cubic parts of the stacking, leading to a state that is decreased in stability from the classical to quantum treatment. Even with this effect, some stacking disordered phases are still predicted to be very close to the same stability as I_h at almost every

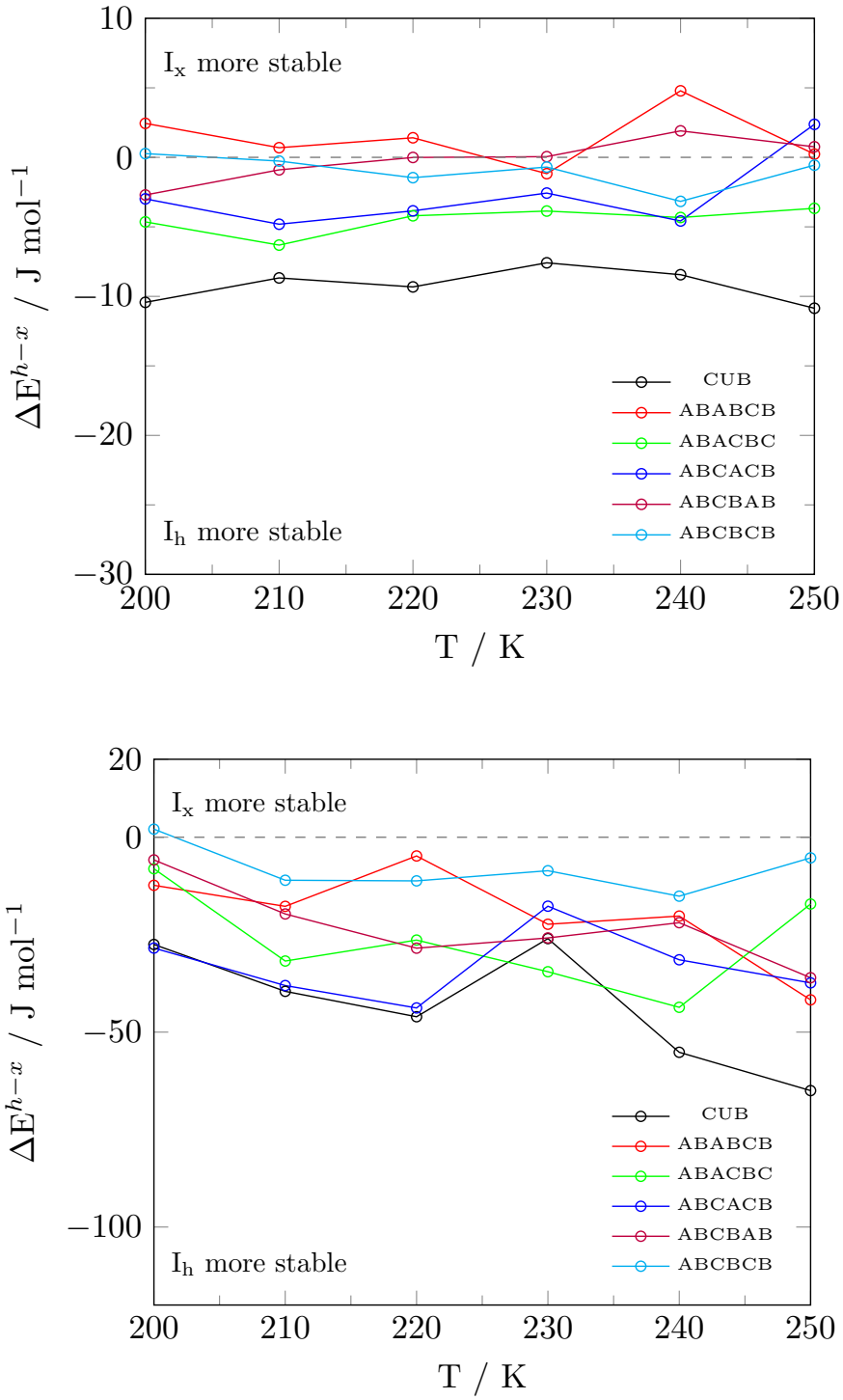

Figure 4.9: Free energy difference between I_h, I_c and the 5 stacking disordered variations, calculated using classical (top) and quantum (bottom) simulations of water using the *harmonic* version of the q-TIP4P/F water potential. A negative free energy difference indicates that I_h is more stable and a positive free energy difference indicates the relevant ice phase is more stable. Error bars are not shown for clarity.

temperature. Again these phases are the ones with the least amount of I_c present however it gives an explanation as to why some stacking faulted ice polymorphs are found under terrestrial condition, rather than it always being

pure I_h.

By comparing the classical anharmonic results with the harmonic results, it can be seen that there are not many differences between them. The ordering of ice phases is identical however the harmonic only results seem to be slightly more stable when compared to the I_c result. The main trends are still observed, with the disordered phases with the least amount of I_c present being more stable. When comparing the quantum anharmonic results to the harmonic version gives a similar but slightly different picture. The harmonic results are just as erratic as the anharmonic results however the ordering of phases is slightly different, with some swapping positions. Although it should be noted that just as above, the phases with the fewest amount of I_c is still more stable. The main difference in the two results comes as temperature is increased, in the anharmonic treatment the phases tend to become more stable relative to I_h as the temperature is increased, whereas in the harmonic results the opposite is true. This does have some overlap when error is considered however it is a small difference in the results arising from the lack of an anharmonic stretch in the water potential. It can be concluded similar to the results discussed earlier that anharmonicity does play a role in the free energy difference between the phases, however this difference is very small. The difference between the quantum and classical harmonic results is identical to the anharmonic results. The classical results being more stable with respect to I_h than the quantum results. This is again due to quantum effects 'washing out' the stability provided by the classical treatment. This is not changed due to the absence of anharmonicity.

Overall the results for stacking disordered ice phases show that the greater degree of I_c within the phase leads to greater destabilisation with respect to I_h, whereas the opposite is true when the amount of I_c is smaller. This can be explained by the same reasoning as to why I_h is more stable relative to I_c. The introduction of anharmonicity does not make a large difference and only affects the free energy results by a small amount compared to the inclusion of NQEs.

4.3.3 Liquid Water

Outside of ice phases, another phase that can be examined using free energy calculations is the liquid phase of water. This can be done using the same q-TIP4P/F potential used above and a similar methodology to calculate the classical free energy and the quantum to classical correction. The results of this can be used to determine the melting points of the ice phases using a

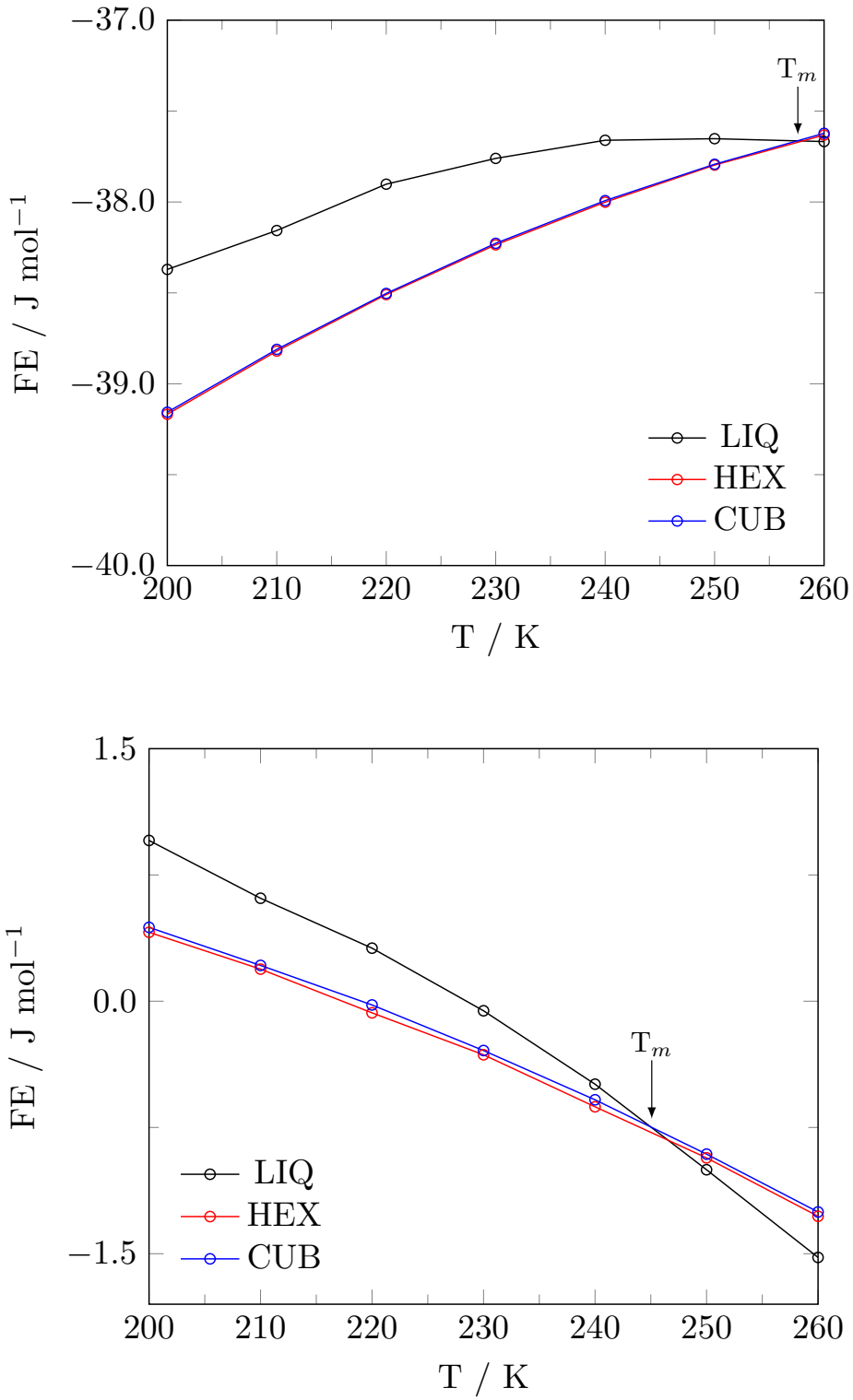

Figure 4.10: Free energy values for liquid water, I_h, and I_c in the classical treatment (upper panel) and overall free energy after quantum effects have been included (lower panel) using an *anharmonic* model. The point at which the ice phases cross the liquid energy values is the melting point (T_m).

classical and quantum treatment, with an anharmonic and harmonic version of the model.

441 water molecules were used in these calculations and the results were

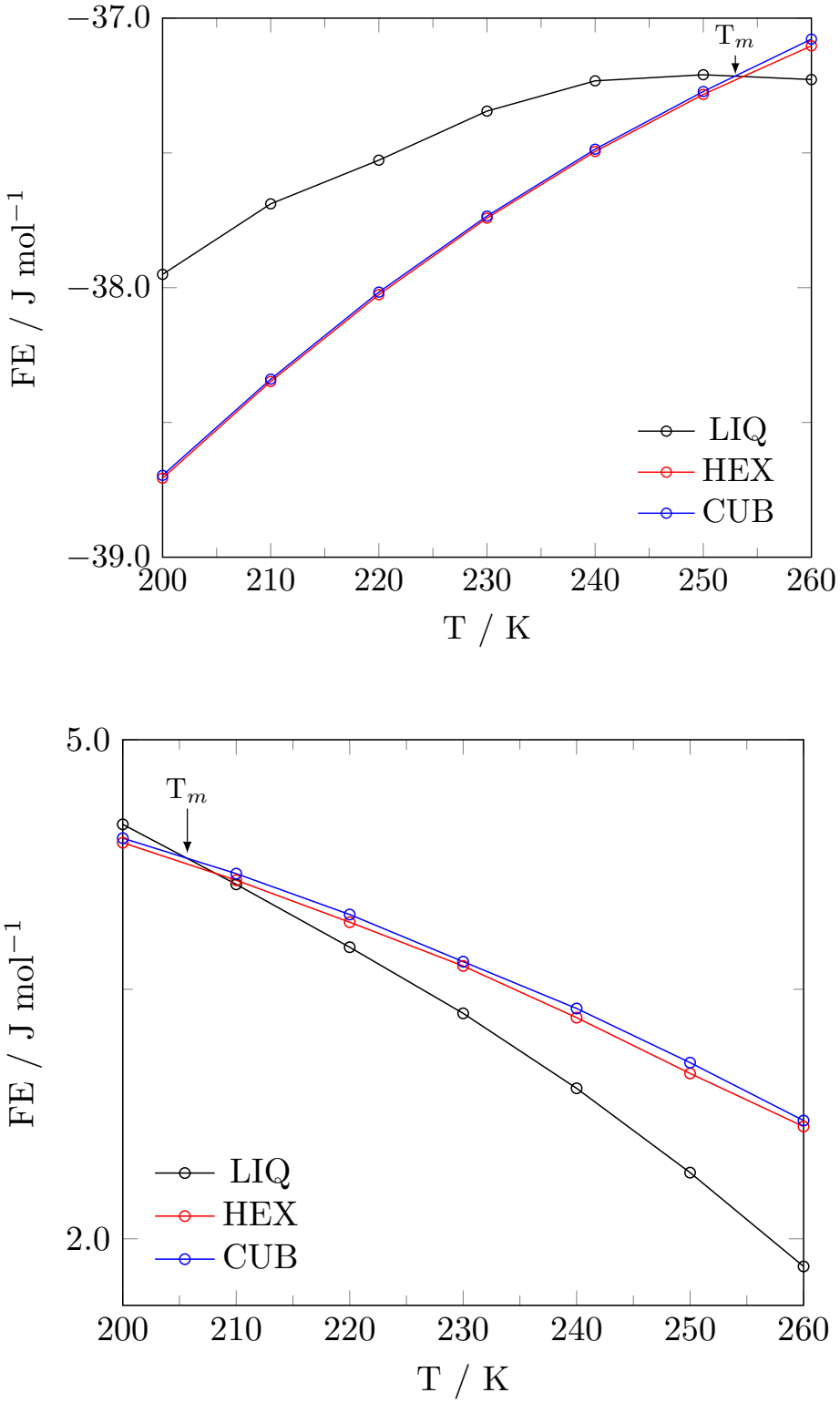

Figure 4.11: Free energy values for liquid water, I_h, and $I_c$in the classical treatment (upper panel) and overall free energy after quantum effects have been included (lower panel) using a *harmonic* model. The point at which the ice phases cross the liquid energy values is the melting point (T_m).

averaged over 3 separate simulations with different starting configurations. The same amount of equilibration was used here as in previous free energy calculations. The results for the free energy of liquid water compared to the

free energy of the two pure ice phases are shown in Figs 4.10 and 4.11, with melting points summarised in Table 4.1.

One of the first features that appears in both the anharmonic and harmonic sets of data, is that the gradient of the lines for the classical results is the opposite sign to the gradient of the quantum results. Since the derivative of the free energy with respect to temperature is the negative of the entropy, it would be expected that both gradients should be negative (suggesting positive entropy for the liquid and ice phases. However in the classical treatment this is not the case, where both solid and liquid phases have a positive gradient from 200 K - 250 K, before starting to decrease, suggesting that these phases have negative entropy within that temperature range. An explanation for this phenomenon is that while classical mechanics provides a good starting point for simulations of rigid body water models, it is not appropriate and is qualitatively inaccurate for water potentials that have flexibility and high frequency intramolecular vibrations. As proof of this, one can consider that the classical entropy of a harmonic oscillator with frequency ω is

$$S_{\mathrm{cl}} = k_B[1 - \ln(\beta\hbar\omega)], \tag{4.46}$$

which tends towards the accurate result for quantum mechanical entropy in the high temperature limit ($\beta\hbar\omega \to 0$)

$$S_{\mathrm{qm}} = k_B[(\beta\hbar\omega/2)\coth(\beta\hbar\omega/2) - \ln(2\sinh(\beta\hbar\omega/2))]. \tag{4.47}$$

As soon as $\beta\hbar\omega > e$, S_{cl} becomes negative and tends to minus infinity at absolute zero[43,177], where the harmonic oscillator reduces to a point of zero measure in the classical space. In liquid water at room temperature there are three intramolecular vibrational modes that make a negative contribution to the entropy, these are the H-O-H bending mode ($\beta\hbar\omega \simeq 8$) and the two O-H stretching vibrations ($\beta\hbar\omega \simeq 17$). While this gives a large negative contribution, the translational and librational modes give an overall positive entropy at temperatures above ≈ 250, which can be seen in both the anharmonic and harmonic results. Despite this incorrect behaviour of the entropy in solid and liquid phases, the classical results give a reasonable value for the melting point of the two ice phases ($\sim$ 257 K anharmonically and $\sim$ 253 K harmonically), which lie in good agreement with previous work on the subject. This is because the high frequency intramolecular modes responsible for the negative entropy contributions have similar frequencies in both solid and liquid phases, which cancel out when the melting point in calculated.

In both anharmonic and harmonic treatments the quantum melting points

Calculation Type	Melting Point / K
Classical Anharmonic	257
Classical Harmonic	253
Quantum Anharmonic	248
Quantum Harmonic	208

Table 4.1: Summary of the melting points obtained for the anharmonic and harmonic versions of the q-TIP4P/F model with classical and quantum simulations.

are lower than the corresponding classical values, $\sim$ 248 K and 9 K lower in the anharmonic treatment and $\sim$ 208 K and 32 K lower in the harmonic treatment. The quantum melting point being lower than the classical melting point is no surprise as the inclusion of NQEs means that ZPE is included. The quantum treatment of this is well known to affect the strength of hydrogen bonds and weaken them, meaning that the ice phases are easier to melt and therefore give a lower melting point when compared to the classical values. The difference between the anharmonic and harmonic treatments in terms of quantum melting point is very large, with the quantum harmonic melting point being 40 K lower than the anharmonic one. This is because the removal of anharmonicity in the asymmetric stretch in the q-TIP4P/F model means that the NQEs are made stronger, meaning that the hydrogen bonds are even weaker and therefore gives a lower melting point. A way of showing this is to look at the diffusion constants for each of these systems compared to the classical and to show a value for the degree of quantum effects in the system. The magnitude of this quantum effect (defined as $D_{\mathrm{qm}}/D_{\mathrm{cl}}$) shows that the anharmonic treatment gives an effect of 1.18, whereas the harmonic treatment gives 1.70. This large difference is the key reason why the harmonic treatment gives such a low quantum melting point, as the increase in quantum effects drastically weakens intermolecular bonds and subsequently the melting point.

One final thing to note is that in all cases, the melting point of $\mathrm{I_h}$ is higher than that of $\mathrm{I_c}$. This is to be expected as $\mathrm{I_h}$ has been shown to be slightly more stable in classical and quantum simulations using an anharmonic or harmonic model in a previous Section of this Chapter. Being more stable means stronger molecular interactions within the system that are slightly harder to break, giving rise to the slightly higher melting point.

4.4 Conclusions

This Chapter has centered on the free energy calculations for various phases of water. Classical free energies were determined using MD with a quantum to classical correction to the free energy obtained by using a PIMD approach (with a RPC used to accelerate these simulations). All results were averaged over three individual simulations to lower the overall error.

When comparing the free energy difference between the pure ice polymorphs I_h and I_c, it was found that the reason for the better stability in I_h is due to long range intermolecular interactions in the system. Moreover this arises almost entirely due to the inclusion of NQEs. In the classical treatment, I_c is more likely to adopt perfect tetrahedral bond angles, which increases the stability and brings it much closer to that of I_h. However when NQEs are included, this stability is 'washed out' and the added stability is lost. This leads to the I_h polymorph being stabilised further when compared to I_c and brings it much closer to the energy difference observed in laboratory experiments.

Our results disagree with work done by Engel *et al*, who came to the conclusion that anharmonicity is responsible for the free energy difference and not NQEs. However as discussed earlier, the PBE DFT functional is known to over-bind hydrogen bonds in water and as such, calling into question this conclusion. A very recent paper by Ceriotti *et al*, uses a DFT approach and crucially come to the same conclusions as presented in this work that NQEs stabilise I_h relative to I_c.

Five stacking disordered varieties of ice between I_h and I_c were also investigated in the same way as the pure phases. As expected, the greater amount of I_c present in the phase, the less stable it is compared to the pure I_h phase, with the opposite true when a lower amount of I_c present. It was found that anharmonicity made a small but negligible difference in the free energy compared to the difference made when NQEs are included. Some of these phases were seen to be very close to the stability of I_h, helping to explain why stacking disordered ice can be found in terrestrial conditions, but pure I_c is never found.

The melting points of the two pure ice phases I_c and I_h were investigated by computing the free energy values for liquid water. This was done using classical and quantum treatments using an anharmonic and harmonic model. It was shown that I_h consistently had a higher melting point than the I_c phase, which is borne out by the data showing that I_h has stronger intermolecular interactions than the I_c phase. The inclusion of NQEs in the simulations results in the correct gradient of free energy, whereas classical treatment sug-

gested that the system possessed negative entropy, suggesting that classical treatment is not sufficient when using a flexible water model. It was also found that the degree of NQEs increases drastically when using a harmonic model due to the absence of the anharmonic stretching modes. This added amount of quantum effects lowers the melting point by 40 K compared to the anharmonic version of the model.

Overall the free energies of two pure ice phases (I_h and I_c) were investigated along with five stacking disordered varieties to determine how NQEs played a role in the stability of the systems. Simulations were carried out using quantum and classical treatments along with an anharmonic and harmonic variant of the q-TIP4P/F water potential. The I_h phase was found to be consistently more stable than I_c due to the difference in the intermolecular interactions and was directly attributed to the inclusion of NQEs. Harmonicity was not found to play a significant role however this did make a difference in the quantum melting point, where the unbalancing of the quantum effects led to a large decrease in the melting point of the ice phases.

Chapter 5

Aqueous Droplets

This Chapter focusses on the analysis of water cluster surfaces and how the addition of NQEs affects their structural and dynamic properties. A coarse grained method is used to quantify the surface allowing a roughness parameter to be calculated, with other properties supporting the findings. Three approaches are used to quantify the water cluster surface, a coarse grained spherical approach, a grid based method and an MC method. All of these analysis methods are in agreement on the nature of the surface roughness when moving from a classical to a quantum-mechanical description of the water clusters.

" If you can keep your head when all about you
Are losing theirs and blaming it on you,
If you can meet with Triumph and Disaster
And treat those two impostors just the same;
If you can make one heap of all your winnings
And risk it on one turn of pitch-and-toss,
And lose, and start again at your beginnings
And never breathe a word about your loss;
If you can talk with crowds and keep your virtue,
Or walk with Kings—nor lose the common touch,
Yours is the Earth and everything that's in it,
And—which is more—you'll be a Man, my son!"

-Rudyard Kipling

5.1 Introduction

Water interfaces are of interest in many disciplines such as biology and atmospheric science. These interfaces on water clusters are of interest due to the importance of water in terrestrial phenomena, as well as the role it plays in extra terrestrial physics and chemistry in the interstellar regions of space. A lot of this research has focused on the water-vapour interface and small ice crystals. In these studies, the properties of water clusters such as the roughness of the surface and orientation of water molecules at the surface are of increased interest as other properties of the system are dependent on these.

The roughness of the surface of liquid water has been determined by x-ray spectroscopy and was first carried out on pure water by Braslau *et al*, their experimental value was later reproduced by using the theoretical capillary wave theory method. Water clusters and their surface properties have been the subject of a number of studies as water clusters can play a role in chemical reactions, making surface properties an area of particular interest.[88,178–182] An example of one of these reactions can be seen in the formation of sulphuric acid in the upper atmosphere, which has been shown to be catalysed by water clusters.[183] This reaction directly leads to the formation of acid rain, which can have devastating environmental consequences. There are other photochemical reactions that water clusters can play a role in such as reactions with nitrogen oxides.[184] Due to the important role these reactions can play, it is clear that more computational study is needed to better understand the mechanisms involved in these reactions, especially when the inclusion of NQE could be a crucial component. The development of improved algorithms and increase in computational power have lead to the increased amount of investigation of the role NQEs play in a variety of systems, two systems studied in detail in this work are bulk liquid and the surface properties of liquid water.

A method was developed by Willard et al[185] to identify the surface of a liquid by coarse-graining the particles in order to obtain a a density field, with the surface of the liquid being the isodensity field at half the bulk density. The positions of the particles can then be determined by a computational method such as MD. These results show that the surface of liquid water manifests as a wavy sheet, exerting thermal fluctuations in accordance with capillary wave theory. This provides a simple and computationally cheap method of determining surface properties. In their work it was successfully applied to liquid water and on assembling pairs of melittin dimers with an interface between the dimers and a solvent.[185]

The procedure runs into the problem of not being able to explicitly in-

clude NQEs when using purely classical MD. In this work a PI approach is used along with the coarse grained procedure to allow for a fully quantum analysis of the surfaces of aqueous nanodroplets, such as those which have been implicated in atmospheric chemical reactions.

In this Chapter we study the surface properties of water clusters over a range of sizes from 50 to 1000 molecules. Both classical and quantum methods are used to highlight the difference in the surface of the cluster when NQE are included. As a final investigation, the diffusion of a negatively charged ion across the surface of a water cluster is presented as a preliminary example of how atmospherically catalysed reactions could be studied using these methods.

As a point of comparison in this work we also use two other methods to support the coarse grained approach of calculating the roughness of liquid surfaces. A purely grid based search method and an MC method, both of these are discussed more in the next Section.

5.2 Calculating the surface

In order to be able to calculate any surface properties of a system, there needs to be a reliable method of defining the interface between the bulk and the surface, and the surface and its surroundings. As well as this, there exists the issue of molecular configurations changing with time and therefore the surface potentially changing, meaning that any method used must be able to account for this by redefining the surface over multiple timesteps. In this work we use three methods to define the surface and some of its general properties. The first is a coarse graining approach developed by Willard et al, the second is a grid based approach, and the third is a MC approach.

5.2.1 Coarse grained surface

The procedure developed by Willard et al[185] and can be applied at any point in time, allowing for its use in time dependent property calculations. This idea behind this method begins with the density field at a point in space-time $\mathbf{r}$,t,

$$\rho(\mathbf{r}, t) = \sum_i \delta(\mathbf{r} - \mathbf{r}_i(t)) \tag{5.1}$$

where $\mathbf{r}_i(t)$ is the position of the ith particle at time t with a summation over all particles in the system. Coarse graining can then be applied using a

convolution using normalized Gaussian functions.

$$\Phi(\mathbf{r};\epsilon) = (2\pi\epsilon^2)^{-d/2} exp(-r^2/2\epsilon^2) \tag{5.2}$$

where r is the magnitude of $\mathbf{r}$ and ϵ is the length of the coarse graining with dimensionality d. Applied to the density field $\rho(\mathbf{r},t)$ obtain the coarse grained density field

$$\bar{\rho}(\mathbf{r},t) = \sum_i \phi(|\mathbf{r} - \mathbf{r}_i(t)|;\epsilon) \tag{5.3}$$

The choice of the coarse graining length depends of the system being investigated. For a system of liquid water, we use a coarse graining length of $\epsilon = 2.4\mathring{A}$ because the bulk correlation of liquid water is roughly one molecular diameter. With the coarse graining length set, interfaces can be defined as the (d-1) dimensional manifold $\mathbf{r} = \mathbf{s}$ with

$$\bar{\rho}(\mathbf{s},t) = c \tag{5.4}$$

where c is a constant. Therefore these instantaneous interfaces are points in space where the vale of the coarse graining field is c. The coarse grained density changes over time as the molecular configuration changes. For any given configuration of a system, interpolation on a spatial grid can easily solve the surface. All that remains is the choice of constant that defines whether a molecule is on the surface, a good value for this is $c = 0.016\ \mathring{A}^{-3}$, which is half of the bulk density of liquid water.

5.2.2 Spherical surface

To allow for easier characterisation of cluster surfaces, it is convenient to work in spherical coordinates (r,θ,ϕ) where r is the distance from the cluster's centre of mass with θ and ϕ the angular displacements. The surface points can be characterised as vectors $\zeta_i(t) = (r_i, \theta_i, \phi_i)$ for which $\rho(\zeta_i(t), t) = c$. The manifold of these surface vectors at time t is $\mathbf{s}$(t), defined as,

$$\mathbf{s}(t) = (\zeta_1(t), \ldots, \zeta_i(t), \ldots, \zeta_N(t)). \tag{5.5}$$

In practice, the surface is investigated as the radial height as a function of the angles, which is effectively a projection of $\mathbf{s}$(t) onto the unit radial vector

$$\mathbf{s}(t) \cdot \hat{\mathbf{r}} \approx s(\theta, \phi, t). \tag{5.6}$$

The function $s(\theta, \phi, t)$ can be expanded in real spherical harmonic functions

$$Y_\ell^m = \begin{cases} \sqrt{\frac{(2\ell+1)(\ell+|m|)!}{2\pi(\ell+m)!}} P_\ell^{|m|}[\cos(\theta)]\sin(|m|\phi) & \text{for } m < 0 \\ \sqrt{\frac{2\ell+1}{4\pi}} P_\ell^0 & \text{for } m = 0 \\ \sqrt{\frac{(2\ell+1)(\ell+|m|)!}{2\pi(\ell+m)!}} P_\ell^{|m|}[\cos(\theta)]\cos(m\phi) & \text{for } m > 0 \end{cases}, \tag{5.7}$$

where $P_\ell^m[\cos(\theta)]$ are the associated Legendre polynomials. The expansion coefficients,

$$s(\theta, \phi, t) = \sum_{\ell=0}^{\infty} \sum_{m=-\ell}^{\ell} c_\ell^m(t) Y_\ell^m(\theta, \phi), \tag{5.8}$$

are real and can be determined by using the orthonormal nature of the spherical harmonics by projecting the according harmonic on $s(\theta, \phi, t)$. The coefficient c_0^0 has a linear relation to the average cluster radius, r_{av}. All other expansion coefficients are representative of the surface roughness, $\Delta s(\theta, \phi)$. Therefore we can state

$$s(\theta, \phi, t) = r_{\mathbf{av}} + \Delta s(\theta, \phi, t), \tag{5.9}$$

and $\Delta s(\theta, \phi, t)$ can be used to characterise the surface roughness and the variation of this with time. In particular, the roughness of a surface can be analysed by calculation of a roughness parameter,

$$R_a = \langle |\Delta s_i| \rangle_{\theta,\phi} = \frac{1}{4\pi} \int_{-1}^{1} d\cos\theta \int_0^{2\pi} d\phi |\Delta s(\theta, \phi)|, \tag{5.10}$$

where R_a is the mean absolute roughness. These values can give an idea about how the surface changes when transforming from a classical to a quantum method, as well as other alterations such as increased cluster size or changing the harmonicity of the water model.

5.2.3 Monte Carlo and grid based surfaces

In this Chapter we also briefly investigate two other methods for determining an instantaneous water surface, these are the MC method and the grid based method. These are general methods and offer a comparison to the method described above. Both methods implemented here still utilise a coarse graining method to determine the surface. The MC and the grid based method used here are similar and are shown in more detail in Fig 5.1.

The grid based system takes a number of points equidistant over a cubic grid that encompasses the entirety of the system and some of the surroundings.

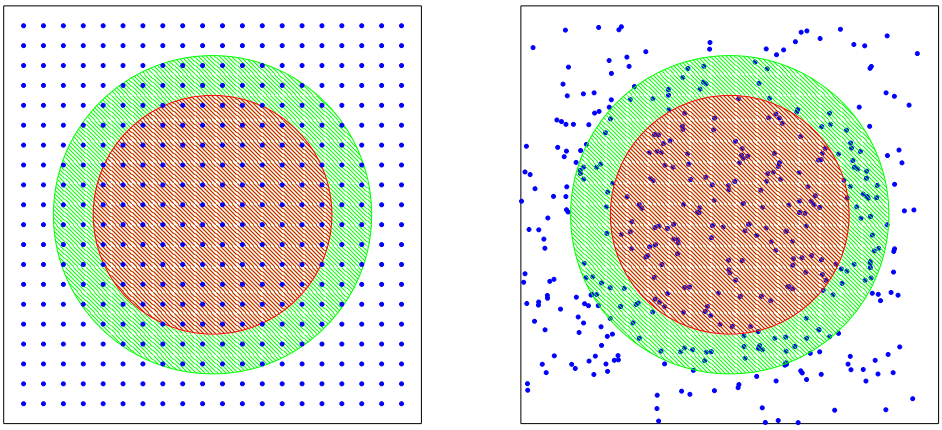

Figure 5.1: 2D illustration of the grid based method (left) and the MC method (right). Chosen points are represented with blue dots. The red circle represents the bulk of a system, the green circle represents the surface, with the white representing the surroundings. The ratio of points found at the surface to the bulk can provide information about the surface of the cluster under investigation.

Each point is determined to be either part of the cluster or the surroundings by calculating the density at that point. Once this is done the surface can be characterised by determining the number of points that are part of the structure but surrounded by a mix of other bulk points and points from the surroundings. From this knowledge about the overall surface can be obtained, such as the fraction of points that lie on the surface of the cluster which can give information about the roughness or smoothness of the surface. The MC method works by taking a number of random points within a defined cube that covers the surface and surroundings and determining if they are part of the surface of the cluster. For each point, if the calculated density is within a certain range (similar to the Willard et al method discussed above) then it is deemed to be part of the surface. This continues until the ratio of the surface to bulk points converges to a constant value. This ratio can be used in a similar fashion to the grid based results in order to determine the smoothness of the surface. As an example, a higher surface to bulk molecule ratio suggests that the surface is rough, whereas a lower ratio suggests a smooth surface with few defects, which can then be supported by looking at other simple to compute properties of the cluster, such as the size and RDFs.

5.2.4 Simulation details

The work done in this Chapter uses the q-TIP4P/F water model for cluster sizes of 50, 100, 250, 500, 750 and 1000 water molecules. Before surface properties were calculated, each system was equilibrated for 50 ps, with surface properties then being calculated over 50 ps (with a time-step of 0.5 fs), both stages used an NVT ensemble. During the surface analysis the surface properties were calculated every 10 timesteps (5 fs). The clusters were investigated at a temperature of 150 K (to avoid separation of the cluster) without any PBCs. All results were produced using an average over 10 individual calculations. For all methods used, classical MD and fully quantum PIMD methods are used for all system sizes, with results being compared. 32 ring-polymer beads are used in the PIMD method as this is more than enough to converge the properties of the water cluster as discussed in previous chapters. The rotational motion of the water clusters are cancelled after each timestep by zeroing the momentum contributing to it. This stops the water cluster gathering too much rotational momentum which could have an impact on the surface and stability of the cluster.

5.3 Surface property results

5.3.1 Coarse grained surface

For this work we present the results for surface parameters discussed above. The classical and quantum results for the surface roughness (R_a) are shown in Fig 5.2. There are a number of interesting things to note about these results. Overall it is found that the inclusion of NQEs lead to a decrease in the roughness of water cluster surfaces when water clusters are above 250 molecules in size. This decreased roughness is then consistently similar between the two methods for the remainder of cluster sizes under investigation. For cluster sizes under 250, the picture is less clear. It can be seen that smaller cluster sizes lead to a marked increase in the error associated with each measurement, this is likely due to the small number of molecules being used and how this would likely lead to more fluctuations in the shape of the cluster and the number of surface molecules changing because of this. As the number of molecules in the cluster increases, the roughness results quickly decrease for the quantum method and overtakes the classical results. From the size of the errors on the small clusters as well as the overlap it is difficult to conclude that the quantum roughness is higher than the classical at low

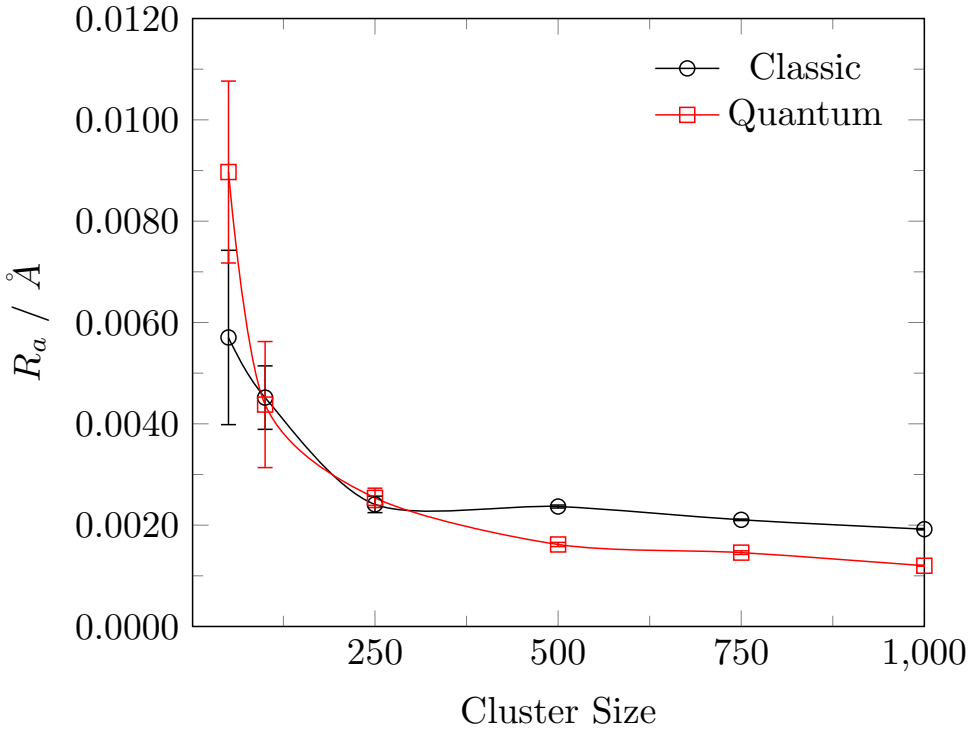

Figure 5.2: Results for the surface roughness of different sized water clusters using classical and quantum methods.

cluster sizes. It is better to conclude that small cluster sizes give rise to much more variation in cluster shapes and surfaces. It is clear that the inclusion of NQEs gives rise to a smoother surface as soon as clusters are increased to sizes where fluctuations within the system do not have a pronounced effect on the surface, further evidenced by the much smaller error bars that are almost entirely negligible.

The results show that the inclusion of NQEs decrease the roughness of the surface of water clusters however it is not immediately clear how this occurs. In order to determine how the cluster changes when these effects are included the structure of the clusters need to be examined in more detail. Initially, it is worth considering that the inclusion of NQEs may have an effect on the overall size of the cluster, either expanding or contracting, which could lead to the change in surface roughness observed. The average radius of clusters was calculated using classic and quantum methods for each cluster size, these are shown in Fig. 5.3.

Overall it can be seen that for all cluster sizes the quantum cluster radius is slightly larger than that of the classical clusters. However this difference is very small and in every case the two computed values lie within the error of the

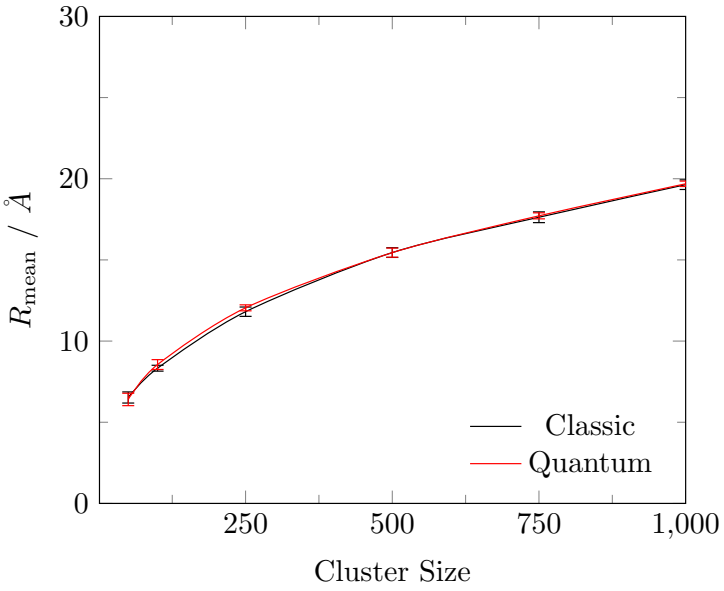

Figure 5.3: Mean cluster radius of different sized water clusters using classical and quantum methods.

other. So it cannot be concluded with true certainty that quantum clusters are larger than classical ones. From these results it is clear that the size of the clusters is hardly affected by the inclusion of NQEs and any expansion or contraction resulting from the inclusion is negligible.

As the clusters for the two methods are almost identical in size for all numbers of molecules present, the inclusion of NQEs must affect the structure and space filling of the cluster in order to affect the smoothness at the surface. In order to examine this in more detail, the RDFs for oxygen-oxygen, oxygen-hydrogen and hydrogen-hydrogen were calculated for a cluster of 50 molecules. These RDFs are shown in Figs 5.4 and 5.5.

For all three of the RDFs the short range structure for the classic and quantum simulations are both very similar, however when moving to further solvation shells the quantum RDFs are not as clearly defined, with more variation in the separation of the water molecules at higher distances. This is most clearly seen in the oxygen-oxygen RDF, which represents the distance between neighbouring molecules. While the short range and the first solvation shell are almost identical with the classical RDF, the second shell to the limits of the cluster show that the quantum simulation gives rise to more variance in the positions of water molecules. The classical by contrast still has a clearly defined peak at the second solvation shell and beyond. This leads to the conclusion that the inclusion of NQEs alters the structure of the water clusters near the surface without changing the size.

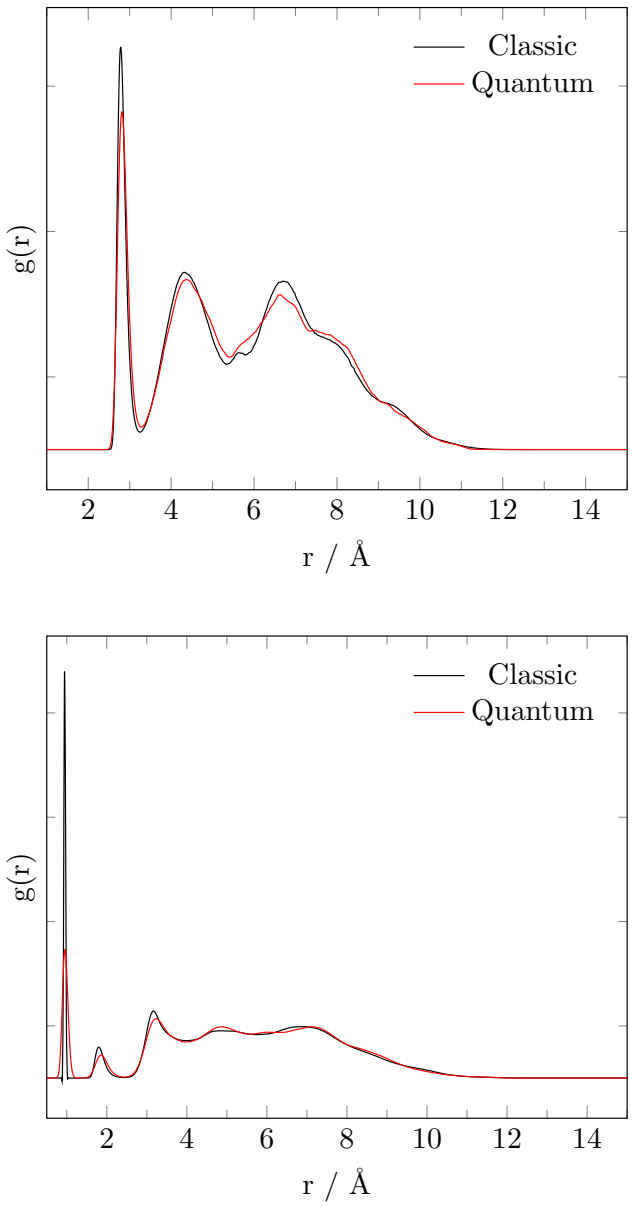

Figure 5.4: Oxygen-Oxygen (upper) and Oxygen-Hydrogen (lower) distances across a cluster of 50 water molecules from classical and quantum simulations.

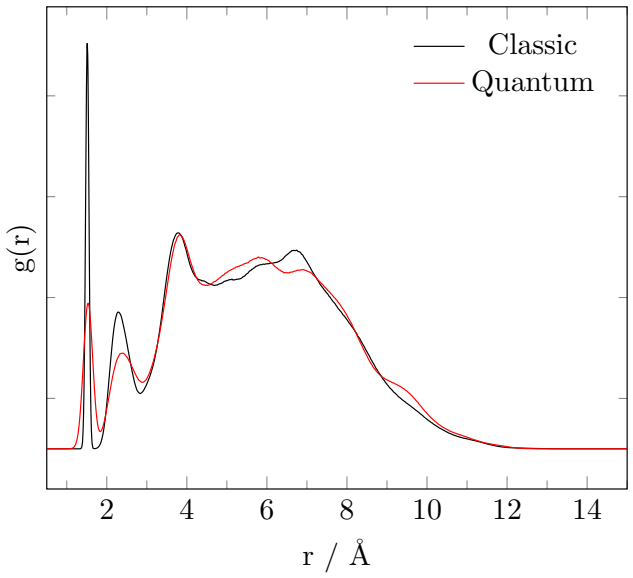

Figure 5.5: Hydrogen-Hydrogen distances across a cluster of 50 water molecules from classical and quantum simulations.

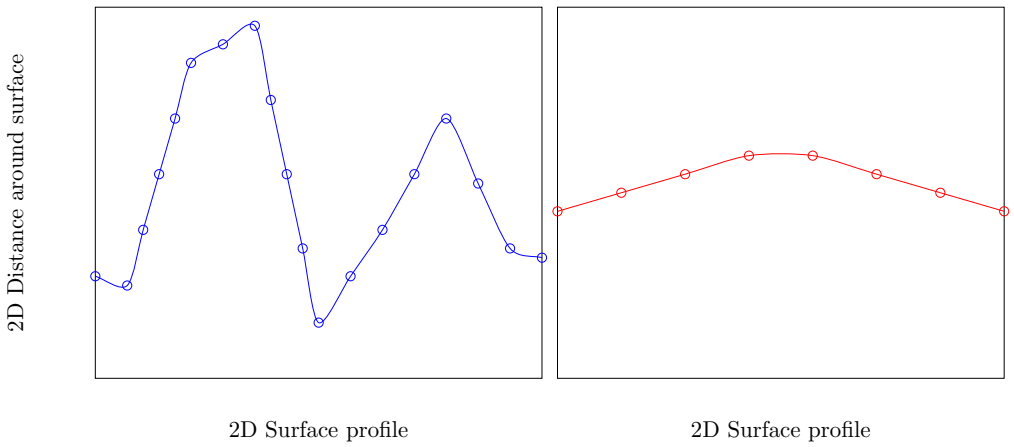

Figure 5.6: Hypothetical rough (left) and smooth (right) surfaces for a cluster. Due to the large amount of defects more molecules can sit on the surface of a rough cluster than a smooth one.

5.3.2 Grid and Monte Carlo surfaces

Using the grid and MC methods a number of water cluster sizes were investigated. For this work we investigate the ratio of the surface molecules to those in the bulk. By doing this we can gain an insight into the roughness of a surface, should the ratio of surface to bulk be high, it can be suggested that the surface is more rough and contains more defects. Should the ratio be lower by comparison, it can be concluded that the surface is more smooth as there would be fewer defects on the surface that give rise to increased numbers of surface molecules. This is illustrated in Fig 5.6, where it can be seen that a hypothetical rougher surface gives rise to more molecules on the surface than if the surface was smooth with few defects. The results for the grid based method are shown in Fig 5.7. It can be seen from these results that using the grid method leads to a lower percentage of molecules at the surface when including NQEs than in the case of a purely classical method, this is consistent with the results for surface roughness above. At low cluster sizes, the difference between the classical and quantum is much closer, with this value gradually increasing until it is clear that the quantum clusters have fewer surface molecules and are therefore smoother. This mimics what we see above, with the classic and quantum staying close to begin with, then clearly separating out, the main difference is that in this case, there is no large discrepancy between the values at very low cluster sizes, instead the two values start off similar and then diverge. For smaller clusters the error bars are significantly smaller than for the coarse grained surface analysis performed above, which is not surprising as the number of grid points are identically placed

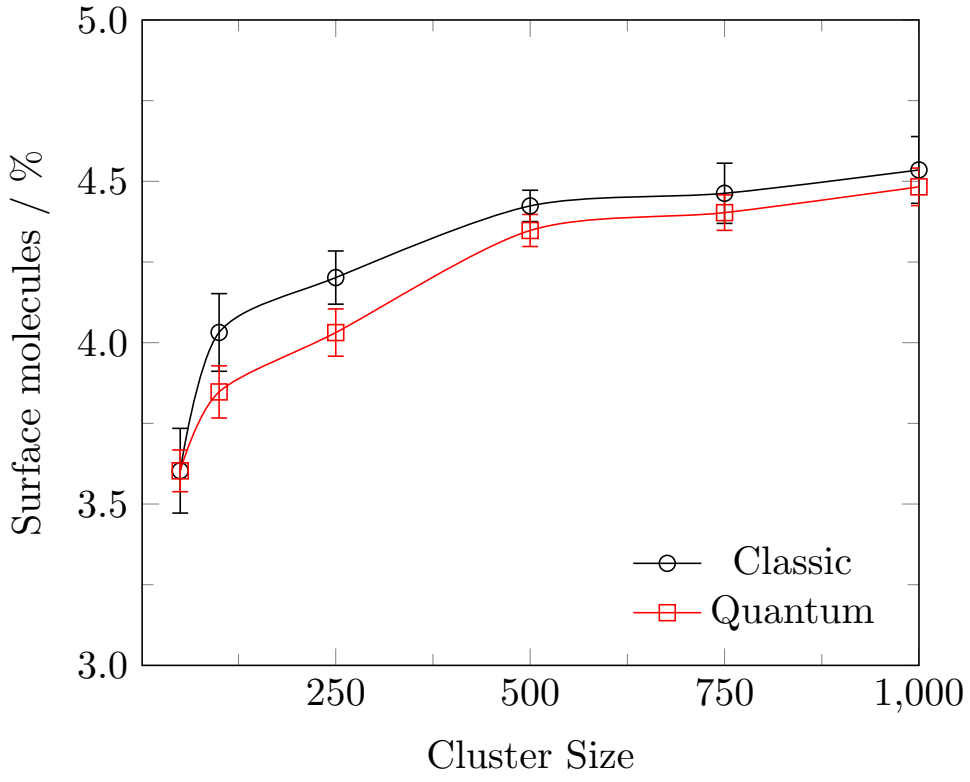

Figure 5.7: Results for the percentage of surface molecules in a water cluster using the classical and quantum grid methods.

at every time step and the overall percentage of surface molecules shouldn't change drastically from one simulation to the next. However a drawback of this method lies in that many of these grid points still lie clearly outside the cluster itself, as a certain distance from the surface needs to be included to make sure it is all accounted for. One other major issue with these results that cannot be ignored is that the percentage of surface molecules increases with cluster size, when it would be expected that larger clusters would see a higher percentage in the bulk and fewer on the surface. This means that as cluster size increases, the percentage of surface molecules should decrease, which is the complete opposite of what the results show. This may be because the number of grid points remains constant throughout however the clusters become significantly larger, which can have the effect of increasing the distance between grid points, giving a much looser 'mesh'. This could lead to the impression that the number of surface molecules are increasing when they aren't. More grid points could be used to overcome this however this becomes quite costly when attempting to produce a better quality 'mesh' of points. This is something the MC method seeks to improve upon.

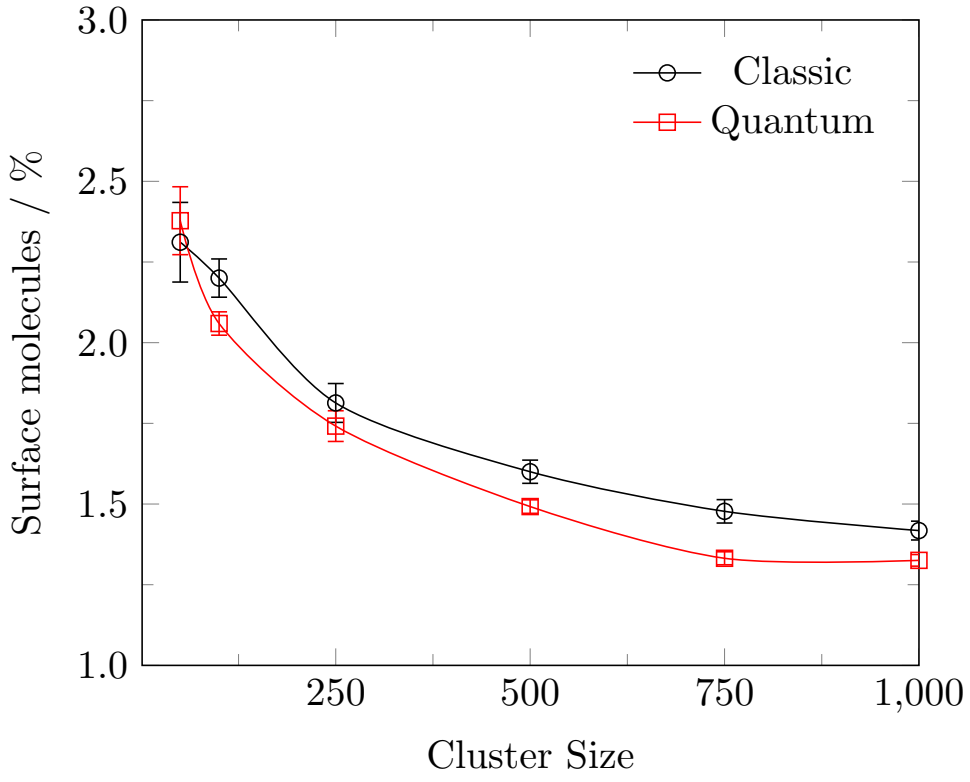

Figure 5.8: Results for the percentage of surface molecules in a water cluster using the classical and quantum MC methods.

The results for the MC grid method are shown in Fig 5.8. It is clear from these results that the expected trend in decreasing surface amounts with increasing cluster size is now visible. The results also agree with the other two methods in that the quantum results clearly shown that there is a smaller percentage of surface molecules at almost every point, with the only exceptions coming at very low cluster sizes where the surface can fluctuate more wildly. The overall percentages are lower using the MC method than the grid method, this is most likely due to the MC method providing better sampling of the cluster, without so many points wasting on exploring the vacant positions around the cluster, instead the MC method runs until well after the final percentage has converged to a value to ensure accuracy. These results show a similar trend to the original coarse grained spherical surface, where the surface becomes smoother with increasing cluster size. this is the expected trend as there should be a fewer percentage of water molecules at the surface as the size of the cluster increases, as the majority should be in the bulk. These results are supported by the analysis carried out above, as it has been shown that the water clusters do not change in size and therefore

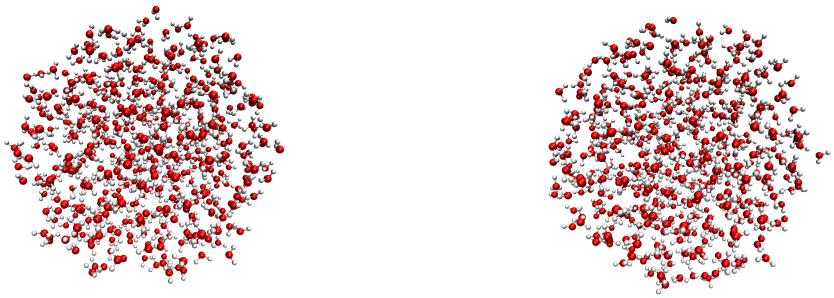

Figure 5.9: Images taken of a classical cluster (left) and a quantum cluster (right) from a simulation of 500 water molecules

the change in surface molecule percentage is affected only by the change in space filling and positioning of the water molecules caused by the inclusion of NQEs.

5.3.3 Other Properties

To show a more illustrative description of the difference in surface roughness, a cluster generated by a classical simulation and one generated by a quantum simulation are shown in Fig. 5.9. It can be seen that in the classical cluster there are more O-H bonds dangling out from the surface with molecules oriented in a more jagged fashion than in the quantum cluster, where there are fewer bonds extending out from the surface, leading to a more spherical cluster with a smoother surface. These images confirm what is observed in the RDFs, where the classical cluster adopts more idealised water molecule positions leading to an increase in molecules extending out from the surface and increasing the roughness. Whereas in the quantum cluster the molecules at the surface are not as likely to adopt idealised positions and instead are more diffuse, leading to fewer molecules extending from the surface and decreasing the roughness of the surface.

Another avenue of investigation was the calculation of the ring-polymer radius of gyration of the hydrogen atoms in the cluster as well as the self diffusion coefficient. The rate of diffusion can give an insight as to how quickly molecules are moving throughout the cluster. The results for both of these properties are shown in Fig. 5.10. The radius of gyration for hydrogen atoms can be seen to slowly decrease as cluster size increases, however this is not

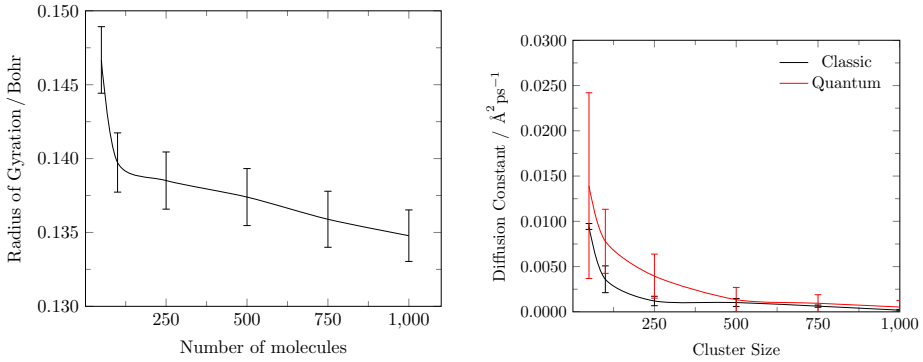

Figure 5.10: Radius of gyration (left) and self diffusion coefficient (right) of classic and quantum water clusters.

by a large amount and does not have an impact on the cluster. This is likely due to there being more free 'OH' bonds at the surface of small clusters and then progressively less as the cluster size increases and more molecules are in the bulk. The results for the self diffusion coefficient show that the water molecules in the quantum clusters diffuse faster than the molecules in the classical clusters. This supports the observations in other results presented here as it has already been shown that quantum clusters move more from the idealised positions which leads to a smoother surface overall, these diffusion coefficients confirm this to be the case, showing a clear tendency for a greater amount of diffusion in the quantum clusters. Both sets of coefficients are much lower than the known value for self diffusion in water, but this is simply due to the significantly lower temperature at which these simulations are carried out, as well as the relatively small number of molecules involved. The error in the diffusion is consistent with the error seen in other properties, with the lower sized clusters producing a much larger error than larger clusters and while there is some minor overlap of errors in the data, the quantum diffusion is higher throughout.

A final component to this investigation was examining how an additional charged species interacts with the water cluster and its surface. For this study a negative ion was chosen with the same mass and LJ parameters as an oxygen atom, and the diffusion constant measured in both classical and quantum simulations. In future studies, other species can be used that correspond better to the types of atom or molecule that may use or interact with water droplets in the course of a reaction. As this study is measuring the diffusion of a single ion only, 500 trajectories were averaged to form the autocorrelation function. The results of this investigation are shown in Fig. 5.11.

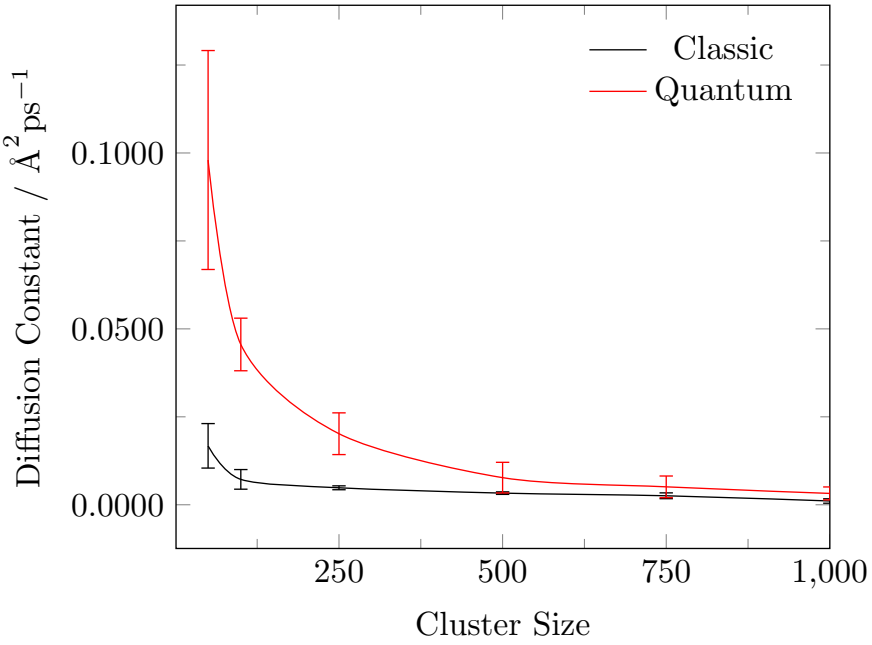

Figure 5.11: Classical and quantum diffusion coefficients for a negative ion interacting with various sizes of water cluster

The results for the ion diffusion are similar to those obtained with the self diffusion coefficient of the water cluster. When NQEs are included the rate of ion diffusion is greater than when using a classical method. Once again there are large error bars when small clusters are examined, however unlike in the case of self diffusion, these bars do not overlap between the two methods until a cluster size of 750 molecules. The overall quantum effect in some of the smaller clusters is between five and ten times, which is huge when compared to the size of quantum effects seen in work discussed earlier. This may be because the low temperatures being used have a freezing effect on the classical clusters, which also has the effect of slowing down diffusion in larger clusters and making it tend towards zero. This freezing effect is not as strong when quantum effects are included and lead to a much larger diffusion constant, although this does begin tending to zero when looking at the largest cluster sizes studied here. These results again highlight the importance of including NQEs in simulations of water clusters and when other species are present. These results are only preliminary and give a brief insight into how NQEs play a role in the interaction of particles with a water cluster. There is a large scope for continuation of this work, by modelling how other elements interact with the cluster and ultimately seeing how NQEs play a role in the simulation of chemical reactions that may happen on the surface of a water cluster.

5.4 Conclusions

In this Chapter the difference between classical and quantum surfaces of water clusters were investigated for a variety of cluster sizes up to 1000 water molecules. The surface was initially examined using a coarse graining approach and allowed for the calculation of a roughness parameter for the surface. It was found that when NQEs were included, the surface of the water cluster became smoother. This was supported by other properties such as the size of the cluster not changing and the RDFs containing different molecule positioning at the surface. As a secondary method of investigation, grid and MC methods were used to calculate a ratio of surface molecules to those in the bulk. The results of these studies showed that there were a lower number of molecules on the surface in quantum simulations than the corresponding classical simulation. These results were consistent with the surface roughness parameter that was calculated showing that quantum simulations give a smoother surface than classical simulations. In addition to this, the self diffusion coefficient of a water cluster along with the radius of gyration were examined, showing a tendency for faster diffusion when using a quantum method. This same result was also found when investigating how a negatively charged ion diffused when placed near the surface

Chapter 6

Conclusions and Further Work

This Chapter summarises the methods and results reported in this work and the conclusions that can be drawn from them. In addition to this a small Section is dedicated to highlighting potential future avenues of investigation.

"It may be that the gulfs will wash us down:
It may be we shall touch the Happy Isles,
And see the great Achilles, whom we knew.
Tho' much is taken, much abides; and tho'
We are not now the strength which in old days
Moved earth and heaven, that which we are, we are;
One equal temper of heroic hearts,
Made weak by time and fate, but strong in will
To strive, to seek, to find, and not to yield"

-Alfred, Lord Tennyson

6.1 Summary and conclusions

The use of the PIMD and RPMD methods allows the recovery of static and dynamic quantum properties respectively of any system of interest. These methods are able to be carried out using classical evolution of a ring-polymer that is made up of multiple replicas of the system and are simple to implement. The drawback of this approach is the increased computational cost of these methods relative to standard classical MD, which is related to the number of ring-polymer beads used to define the system. The cost scales linearly with the number of beads as each bead only interacts with it's corresponding images in other beads. Efforts have been made in recent years to accelerate these methods with the RPC and r-RPC methods proving successful. However these methods cannot be applied without some conditions being met. In the case of RPC the PES must be able to be separated into high and low frequency components and therefore the method cannot be used when this is not possible. The r-RPC method requires a cheaply available reference potential that gives a good approximation to the PES. Therefore there exist systems where it is not possible to use either method to speed up PIMD and RPMD simulations.

To address this, the work presented here introduced a new method for accelerating PIMD simulations, RPI. This method does not have any prerequisite conditions and can therefore be applied to any system of interest. The RPI relies on the assumption that there is a correlation between the forces on ring-polymer beads that can be exploited in order to reduce the total number of force evaluations at each time-step of a simulation. For the RPI method this is done by selecting a small number of ring-polymer beads, computing the full PIMD forces on them, then approximating the forces on the other beads using the KRR interpolation method. This interpolation is much faster than a force evaluation and therefore can lead to significant computational time saving. Another advantage to this method is that it only uses one parameter to control the Gaussian width for the interpolation, which can be optimised on-the-fly at almost no additional cost.

In this work we applied the RPI method to systems of liquid water and para-hydrogen. These were chosen as they are systems of interest in computational chemistry and NQEs play an important role in their properties. For both systems, the RPI method proved successful in recovering the full PIMD result using a smaller number of ring-polymer beads for a number of static properties including potential energy, kinetic energy and RDFs, as well as recovering dynamic results such as diffusion coefficient obtained using RPMD.

These properties were generally recovered completely using between 12 and 16 beads, meaning that RPI simulations are at least twice as fast as full PIMD and RPMD simulations.

When compared to the RPC method the RPI does not converge as quickly and ultimately is slower when applied to the system of liquid water. However this is due to the RPC method splitting the PES into high and low frequency components, with the high frequency part calculated using the full PIMD number of beads and the low frequency part calculated using the RPC method. When the RPC method is used on both the high and low frequency components, the convergence becomes worse than that of standard PIMD. This highlights the main drawback of the RPC method, as it's application is limited to a PES where this separation is possible. Therefore it can be concluded that while RPC is the clearly superior choice when investigating liquid water, it's limitations mean that the RPI method is superior in systems where RPC is not available to use. The RPI method was shown to be superior to the RPC in the static properties of the para-hydrogen system, where such a separation of the PES is not as straightforward.

Overall the RPI method provides a route for carrying out PIMD and RPMD simulations at a fraction of the computational cost. The main advantage of this method is that it requires no underlying assumptions about the PES and can be applied universally to any chemical system of interest, in particular this method can be used for systems that are more complex such that standard PIMD and other PI accelerating methods are not feasible.

In addition to the development of an accelerated path integral method, this work also focussed on the investigation of solid aqueous phases, in particular the study of the free energy difference between I_h and I_c, the free energy ordering of stacking disordered ice phases and the free energy liquid water. The motivation for this study lies in the question of why I_h is more stable than I_c as there is only a very small difference between the two polymorphs and both have very similar properties. In addition, the stacking disordered phases have not been the study of an in depth investigation as to how the free energy values are placed between I_h and I_c. Finally the free energy of liquid water can give an insight to the melting points of the ice polymorphs in both anharmonic and harmonic models as well as classical and quantum simulations.

Both classical and quantum methods were used alongside an anharmonic and harmonic water potential in order to allow for a complete investigation. The classical free energy of these phases was calculated using the Debye crystal free energy, and terms corresponding to the energy difference between

constrained and unconstrained ice, and the energy difference between the Debye crystal and unconstrained ice, with the latter being calculated using a thermodynamic integration method. In order to compute the quantum free energy of a system, a correction term was calculated using thermodynamic integration that represented the free energy difference between the classical and the quantum system, which could then be added to the classical free energy in order to give a quantum free energy. The harmonic water potential used was a modified version of the q-TIP4P/F model where the anharmonic O-H stretch term was removed.

The anharmonic and harmonic quantum and classical free energy results for the I_h and I_c polymorphs were computed using MD and PIMD over a range of temperatures. From the initial results it could be seen that harmonicity was not a factor in the stability of I_h over I_c however when moving from a classical to a quantum treatment, I_h becomes more stable relative to I_c. In order to determine how the NQEs play a role in this added stability, the contributions to the free energy were examined, where it confirmed that the quantum correction to the free energy provided the stabilisation rather than the other components. From this, the components of the quantum correction could be separated into intra- and intermolecular contributions to determine which is responsible for the stabilisation of I_h. From this it was concluded that the intermolecular component to the quantum free energy was responsible for I_h being more stable than I_c. To investigate this, the average bond lengths, bond angles and molecular dipoles were measured within the ice systems using the classical and quantum methods. From this it could be seen that classically the I_c polymorph has a tendency to adopt a perfect tetrahedral bond angle, lowering its free energy. However, once NQEs are included, this tendency is no longer present and is effectively washed out, leading to the I_c being destabilised relative to the I_h polymorph.

The investigation of stacking disordered ice phases between I_h and I_c showed that the free energy stability was related to the number of cubic layers, with stability being very similar to that of I_h until more than half of the phase was cubic, where the free energy increased to be closer to that of I_c. The quantum treatment of these phases showed the same trends as for the pure phases, with all stacking disordered phases containing I_c increasing in energy relative to I_h. Finally the investigation of liquid water showed that the inclusion of NQEs decreases the melting point of the ice phases due to ZPE, and a significant decrease in melting point when the quantum system was treated harmonically. This is due to the removal of anharmonicity effectively increasing the strength of NQEs, causing a much lower than expected melting

point.

Overall this investigation has shown that NQEs are directly responsible for the increase in stability of I_h compared to that of I_c due to the intermolecular properties of the system. This work has further highlighted the necessity for the inclusion of NQEs in molecular simulations of systems where they could be expected to play a significant role.

A final investigation carried out in this work is the analysis of NQEs on the surface properties of water clusters. This was carried out using a coarse grained approach and the computation of a surface roughness parameter. This was supplemented with two other methods, a grid based and an MC approach. All methods supported the conclusion that the inclusion of NQEs resulted in a smoother cluster surface, which has the potential to make a difference when using these clusters in applications that involve interfaces with another species or chemical reactions. This smoother surface arises from a change in the space filling arrangement within the cluster itself and does not come from an increase or decrease in cluster size. The space filling and orientation of water molecules is more rigid in classical simulations whereas in quantum simulations the molecules towards the surface were more prone to moving slightly from expected positions, evidenced by lower and broader peaks observed in the oxygen-oxygen RDF.

These findings were further justified when examining the self diffusion coefficient of the water cluster, where it was found that diffusion happened faster in the quantum simulation, further suggesting a greater tendency to move from the idealised positions. Finally, a short preliminary investigation was carried out into how a negatively charged ion interacted with the water cluster and its surface. The results showed that the ion diffused over the surface faster when in a quantum simulation than the corresponding classical simulation.

6.2 Future work

Following the successful implementation of the RPI scheme and the demonstration of its time saving capabilities, it can now be applied to any system of interest where nuclear quantum effects are important, but full PIMD simulations are not possible due to cost and other accelerating schemes are impractical or not able to be used. However the application of this method in future work is universal to all systems. Future work on the method itself should be focussed on optimising the existing implementation and developing

a program that can be implemented easily by other researchers who wish to use the method. It may also be possible to hybridise the RPI method so as to enable its use in an *ab initio* setting

The successful determination of the cause of the free energy difference between I_h and I_c has highlighted the importance of the inclusion of NQEs in molecular simulations. However despite the suitability of the water model chosen for this study, future work should be focussed on replicating these results using quantum simulations of other suitable water models to further validate the conclusions reached in this work.

There is more work to be done in the analysis of water clusters such as the diffusion of specific chemical species over the surface of classical and quantum water clusters. The work presented her is only in its infancy however has already showed that NQE play a role in affecting the interaction of the ion with the surface of a water cluster. Future work can focus on modelling specific elements on the surface of a water cluster and this could ultimately lead to the investigation of chemical reactions that happen on water surfaces.

Bibliography

[1] G. A. Cisneros, K. T. Wikfeldt, L. Ojamäe, J. Lu, Y. Xu, H. Torabifard, A. P. Bartók, G. Csányi, V. Molinero and F. Paesani, *Chem. Rev.*, 2016, **116**, 7501.

[2] R. Bukowski, K. Szalewicz, G. C. Groenenboom and A. van der Avoird, *Science.*, 2007, **315**, 1249.

[3] W. Cencek, K. Szalewicz, C. Leforestier, R. van Harrevelt and A. van der Avoird, *Phys. Chem. Chem. Phys.*, 2008, **10**, 4716.

[4] C. Vega and J. L. F. Abascal, *Phys. Chem. Chem. Phys.*, 2011, **13**, 19663.

[5] T. E. Markland and M. Ceriotti, *Nat. Rev. Chem.*, 2018, **2**, 0109.

[6] M. Ceriotti and T. Markland, *J. Chem. Phys.*, 2013, **138**, 014112.

[7] S. Habershon, D. E. Manolopoulos, T. E. Markland and T. F. Miller, *Annu. Rev. Phys. Chem.*, 2013, **64**, 387–413.

[8] M. Ceriotti, M. Parrinello, T. E. Markland and D. E. Manolopoulos, *J. Chem. Phys.*, 2010, **133**, 124104.

[9] G. S. Fanourgakis, T. E. Markland and D. E. Manolopoulos, *J. Chem. Phys.*, 2009, **131**, 094102.

[10] T. E. Markland and D. E. Manolopoulos, *J. Chem. Phys.*, 2008, **129**, 024105.

[11] T. E. Markland and D. E. Manolopoulos, *Chem. Phys. Letters*, 2008, **464**, 256 – 261.

[12] M. Ceriotti and D. E. Manolopoulos, *Phys. Rev. Lett.*, 2012, **109**, 100604.

[13] M. Ceriotti, D. E. Manolopoulos and M. Parrinello, *J. Chem. Phys.*, 2011, **134**, 084104.

[14] A. Perez and M. E. Tuckerman, *J. Chem. Phys.*, 2011, **135**, 064104.

[15] S. J. Buxton and S. Habershon, *J. Chem. Phys.*, 2017, **147**, 224107.

[16] S. Habershon and D. E. Manolopoulos, *J. Chem. Phys.*, 2011, **135**, 224111.

[17] S. Habershon and D. E. Manolopoulos, *J. Chem. Phys.*, 2009, **131**, 244518.

[18] R. P. Feynman and A. R. Hibbs, *Quantum mechanics and path integrals*, McGraw-Hill, New York, 1965.

[19] M. Parrinello and A. Rahman, *J. Chem. Phys.*, 1984, **80**, 860 – 867.

[20] A. Wallqvist and B. Berne, *Chem. Phys. Lett.*, 1985, **117**, 214 – 219.

[21] S. Habershon, T. E. Markland and D. E. Manolopoulos, *J. Chem. Phys.*, 2009, **131**, 024501.

[22] R. A. Kuharski and P. J. Rossky, *J. Chem. Phys.*, 1985, **82**, 5164–5177.

[23] L. H. de la Pena and P. G. Kusalik, *J. Chem. Phys.*, 2004, **121**, 5992–6002.

[24] L. H. de la Pena and P. G. Kusalik, *J. Chem. Phys.*, 2006, **125**, 054512.

[25] S. Habershon, G. S. Fanourgakis and D. E. Manolopoulos, *J. Chem. Phys.*, 2008, **129**, 074501.

[26] T. F. M. III and D. E. Manolopoulos, *J. Chem. Phys.*, 2005, **123**, 154504.

[27] B. Chen, I. Ivanov, M. L. Klein and M. Parrinello, *Phys. Rev. Lett.*, 2003, **91**, 215503.

[28] V. Molinero and E. B. Moore, *J. Chem. Phys. B.*, 2009, **113**, 4008–4016.

[29] W. L. Jorgensen, J. Chandrasekhar, J. D. Madura, R. W. Impey and M. L. Klein, *J. Chem. Phys.*, 1983, **79**, 926–935.

[30] W. L. Jorgensen and J. D. Madura, *Mol. Phys.*, 1985, **56**, 1381–1392.

[31] M. W. Mahoney and W. L. Jorgensen, *J. Chem. Phys.*, 2000, **112**, 8910–8922.

[32] H. Nada and J. P. J. M. van der Eerden, *J. Chem. Phys.*, 2003, **118**, 7401–7413.

[33] H. J. C. Berendsen, J. P. M. Postma, W. F. van Gunsteren, A. DiNola and J. R. Haak, *J. Chem. Phys.*, 1984, **81**, 3684–3690.

[34] F. Paesani, W. Zhang, D. A. Case, T. E. Cheatham, III and G. A. Voth, *J. Chem. Phys.*, 2006, **125**, 184507.

[35] S. W. Rick, S. J. Stuart and B. J. Berne, *J. Chem. Phys.*, 1994, **101**, 6141.

[36] S. W. Rick, *J. Chem. Phys.*, 2001, **114**, 2276–2283.

[37] S. K. Reddy, S. C. Straight, P. Bajaj, C. H. Pham, M. Riera, D. R. Moberg, M. A. Morales, C. Knight, A. W. Götz and F. Paesani, *J. Chem. Phys.*, 2016, **145**, 194504.

[38] J. L. F. Abascal and C. Vega, *J. Chem. Phys.*, 2005, **123**, 234505.

[39] R. H. McKenzie, *Chem. Phys. Lett.*, 2012, **535**, 196–200.

[40] R. H. McKenzie, C. Bekker, B. Athokpam and S. G. Ramesh, *J. Chem. Phys.*, 2014, **140**, 174508.

[41] T. E. Markland and B. J. Berne, *Proc. Nat. Acad. Sci. USA*, 2012, **109**, 7988.

[42] X.-Z. Li, B. Walker and A. Michaelides, *Proc. Nat. Acad. Sci. USA*, 2011, **108**, 6369 – 6373.

[43] S. Habershon and D. E. Manolopoulos, *Phys. Chem. Chem. Phys.*, 2011, **13**, 19714.

[44] I. R. Craig and D. E. Manolopoulos, *J. Chem. Phys.*, 2004, **121**, 3368–3373.

[45] I. R. Craig and D. E. Manolopoulos, *J. Chem. Phys.*, 2005, **122**, 084106.

[46] I. R. Craig and D. E. Manolopoulos, *J. Chem. Phys.*, 2005, **123**, 034102.

[47] T. F. Miller and D. E. Manolopoulos, *J. Chem. Phys.*, 2005, **122**, 184503.

[48] B. J. Braams and D. E. Manolopoulos, *J. Chem. Phys.*, 2006, **125**, 124105.

[49] A. R. Menzeleev and T. F. Miller, *J. Chem. Phys.*, 2010, **132**, 034106.

[50] N. Boekelheide, R. Salomón-Ferrer and T. F. Miller III, *Proc. Nat. Acad. Sci. USA*, 2011, **108**, 16159–16163.

[51] S. Habershon, B. J. Braams and D. E. Manolopoulos, *J. Chem. Phys.*, 2007, **127**, 174108.

[52] T. E. Markland, S. Habershon and D. E. Manolopoulos, *J. Chem. Phys.*, 2008, **128**, 194506.

[53] X. C. Huang, S. Habershon and J. M. Bowman, *Chem. Phys. Letters*, 2008, **450**, 253.

[54] D. Frenkel and B. Smit, *Understanding molecular simulation: From algorithms to applications*, Academic Press, San Diego, USA, 2002.

[55] T. L. Malkin, B. J. Murray, C. G. Salzmann, V. Molinero, S. J. Pickering and T. F. Whale, *Phys. Chem. Chem. Phys.*, 2015, **17**, 60–76.

[56] R. P. Feynman, *Progress in Low Temperature Physics, vol 1.*, North Holland Publishing Co., Amsterdam, 1955.

[57] J. J. Max and C. Chapados, *J. Chem. Phys.*, 2009, **131**, 184505.

[58] C. McBride, J. L. Aragones, E. G. Noya and C. Vega, *Phys. Chem. Chem. Phys*, 2012, **14**, 15199–15205.

[59] ed. D. A. Palmer, R. Fernández and A. H. Harvey, *Aqueous systems at elevated temperatures and pressures: Physical chemistry in water, steam and hydrothermal solutions*, Elsevier/Academic Press, 2004.

[60] C. Alhambra, J. Gao, J. C. Corchado, J. Villà and D. G. Truhlar, *J. Am. Chem. Soc.*, 1999, **121**, 2253–2258.

[61] D. G. Truhlar, J. Gao, C. Alhambra, M. Garcia-Viloca, J. Corchado, M. L. Sánchez and J. Villà, *Acc. Chem. Res.*, 2002, **35**, 341–349.

[62] M. H. M. Olsson, P. E. M. Siegbahn and A. Warshel, *J. Am. Chem. Soc.*, 2004, **126**, 2820–2828.

[63] V. Serway, *College Physics. 2 (eighth ed.)*, Belmont: Brooks/Cole, 2008.

[64] J. Lobaugh and G. A. Voth, *J. Chem. Phys.*, 1997, **106**, 2400–2410.

[65] J. A. Poulson, G. Nyman and P. J. Rossky, *Proc. Natl. Acad. Sci. USA*, 2005, **102**, 6709.

[66] B. Guillot and Y. Guissani, *J. Chem. Phys.*, 1998, **108**, 10162.

[67] J. L. Barrat and I. R. McDonald, *Mol. Phys.*, 1990, **70**, 535.

[68] A. Wallqvist and O. Teleman, *Mol. Phys.*, 1991, **74**, 515.

[69] D. E. Smith and A. D. J. Haymet, *J. Chem. Phys.*, 1992, **96**, 8450.

[70] T. J. H. Hele, M. J. Willatt, A. Muolo and S. C. Althorpe, *J Chem Phys*, 2015, **142**, 191101.

[71] E. Geva, Q. Shi and G. A. Voth, *J. Chem. Phys.*, 2001, **115**, 9209–9222.

[72] G. A. Voth, *Adv. Chem. Phys.*, 2007, **93**, 135–218.

[73] S. Jang and G. A. Voth, *J. Chem. Phys.*, 1999, **111**, 2371–2384.

[74] J. Cao and G. A. Voth, *J. Chem. Phys.*, 1994, **100**, 5106–5117.

[75] F. Paesani and G. A. Voth, *J. Chem. Phys.*, 2010, **132**, 014105.

[76] D. Eisenberg and W. Kauzmann, *The structure and properties of water*, Oxford University Press, Oxford, UK, 2005.

[77] P. W. Bridgman, *Proc. Am. Acad. Arts Sci.*, 1912, **47**, 441.

[78] C. W. F. T. Pistorius, E. Rapoport and J. B. Clark, *J. Chem. Phys*, 1967, **48**, 5509.

[79] C. Lobban, J. L. Finney and W. F. Kuhs, *Nature*, 1998, **391**, 268.

[80] G. P. Johari, *J. Chem. Phys*, 2003, **118**, 242.

[81] C. G. Salzmann, P. G. Radaelli, A. Hallbrucker, E. Mayer and J. L. Finney, *Science*, 2006, **311**, 1758.

[82] O. Mishima and H. E. Stanley, *Nature*, 1998, **396**, 329.

[83] R. Torre, P. Bartolini and R. Righini, *Nature*, 2004, **428**, 296.

[84] G. P. Johari and O. Andersson, *J. Chem. Phys.*, 2004, **120**, 6207.

[85] K. de Souza Torres and O. C. Winter, *The When and Where of Water in the History of the Universe*, Academic Press, 2018.

[86] E. R. Batista, S. S. Xantheas and H. Jonsson, *J. Chem. Phys.*, 1993, **109**, 4546.

[87] A. V. Gubskaya and P. G. Kusalik, *J. Chem. Phys.*, 2002, **117**, 5290.

[88] F. Paesani and G. A. Voth, *J. Phys. Chem. B*, 2009, **113**, 5702.

[89] C. Vega, M. M. Conde, C. McBride, J. L. F. Abascal, E. G. Noya, R. Ramirez and L. M. Sese, *J. Chem. Phys.*, 2010, **132**, 046101.

[90] L. H. de la Pena, M. S. G. Razul and P. G. Kusalik, *J. Chem. Phys.*, 2005, **131**, 144506.

[91] E. G. Noya, C. Vega and L. M. Sese, *J. Chem. Phys.*, 2009, **131**, 124518.

[92] L. A. Báez and P. Clancy, *Mol. Phys.*, 1995, **86**, 385.

[93] E. Sanz, C. Vega, J. L. F. Abascal and L. G. MacDowell, *Phys. Rev. Lett.*, 2004, **92**, 255701.

[94] C. Vega, E. Sanz, J. L. F. Abascal and E. G. Noya, *J. Phys. Condens. Matter.*, 2008, **20**, 153101.

[95] H. J. C. Berendsen, J. R. Grigera and T. P. Staatsma, *J. Phys. Chem.*, 1987, **91**, 6269 – 6271.

[96] J. L. F. Abascal and C. Vega, *Phys. Chem. Chem. Phys.*, 2007, **9**, 2775.

[97] J. L. F. Abascal, C. Vega and E. Sanz, *Phys. Chem. Chem. Phys.*, 2008, **11**, 556.

[98] E. Whalley, *J. Chem. Phys.*, 1984, **81**, 4087.

[99] E. A. Engel, B. Monserrat and R. J. Needs, *Phys. Rev. X*, 2015, **5**, 021033.

[100] H. Tanaka and I. Okabe, *Chem. Phys. Lett.*, 1996, **259**, 593 – 598.

[101] E. Whalley, *Can. J. Chem.*, 1977, **55**, 3429–3441.

[102] C. Vega, C. Mcbride, E. Sanz and J. L. F. Abascal, *Phys. Chem. Chem. Phys.*, 2005, **7**, 1450–1456.

[103] C. P. Herrero and R. Ramírez, *J. Chem. Phys.*, 2014, **140**, 234502.

[104] H. Tanaka, *J. Chem. Phys.*, 1998, **108**, 4887–4893.

[105] M. J. Gillan, D. Alfé and A. Michaelides, *J. Chem. Phys.*, 2016, **144**, 130901.

[106] M. P. Allen, in *Computational soft matter: From synthetic polymers to proteins*, ed. H. G. Norbert Attig, Kurt Binder and K. Kremer, John von Neumann Institute for Computing, Jülich, 2004, vol. 23, ch. Introduction to Molecular Dynamics Simulation.

[107] A. R. Leach, *Molecular Modelling: Principles and Applications*, Pearson, 2001.

[108] M. P. Allen and D. J. Tildesley, *Computer Simulation of Liquids*, Oxford University Press, Oxford, 2005.

[109] D. C. Rapport, *The Art of Molecular Dynamics Simulation*, Cambridge, 1995.

[110] J. E. Lennard-Jones, *Proc. R. Soc. Lond. A.*, 1924, **106**, 463–477.

[111] L. Verlet, *Phys. Rev.*, 1967, **159**, 98–103.

[112] W. C. Swope, H. C. Andersen, P. H. Berens and K. R. Wilson, *J. Chem. Phys.*, 1982, **76**, 648.

[113] H. C. Andersen, *The Journal of chemical physics*, 1980, **72**, 2384–2393.

[114] G. Bussi, D. Donadio and M. Parrinello, *J. Chem. Phys.*, 2007, **126**, 014101.

[115] G. Bussi and M. Parrinello, *Comput. Phys. Commun.*, 2008, **179**, 26–29.

[116] M. E. Tuckerman, *Statistical Mechanics: Theory and molecular simulation*, Oxford University Press, 2012.

[117] L. S. Schulman, *Techniques and Applications of Path Integration*, Dover Publications, 2005.

[118] J. A. Barker, *J. Chem. Phys.*, 1979, **70**, 2914.

[119] R. D. Coalson, *J. Chem. Phys.*, 1986, **85**, 926.

[120] D. Chandler, *Introduction to Modern Statistical Mechanics*, Oxford University Press, Oxford, UK, 1987.

[121] M. Parrinello and A. Rahman, *The Journal of chemical physics*, 1984, **80**, 860–867.

[122] B. J. Braams and D. E. Manolopoulos, *The Journal of chemical physics*, 2006, **125**, 124105.

[123] R. W. Hall and B. J. Berne, *J. Chem. Phys.*, 1984, **81**, 3641.

[124] D. A. McQuarrie, *Statistical Mechanics*, University Science, Sausalito, CA, USA, 2000.

[125] I. R. Craig and D. E. Manolopoulos, *Chem. Phys.*, 2006, **322**, 236 – 246.

[126] D. Chandler and P. G. Wolynes, *J. Chem. Phys.*, 1981, **74**, 4078.

[127] R. Collepardo-Guevara, Y. V. Suleimanov and D. E. Manolopoulos, *J. Chem. Phys.*, 2009, **128**, 174713.

[128] J. O. Richardson and S. C. Althorpe, *J. Chem. Phys.*, 2009, **131**, 214106.

[129] Y. V. Suleimanov, R. Collepardo-Guevara and D. E. Manolopoulos, *J. Chem. Phys.*, 2011, **134**, 044131.

[130] P. Bolhuis, D. Chandler, C. Dellago and P. Geissler, *Annu. Rev. Phys. Chem.*, 2002, **53**, 291–318.

[131] N. Ananth and T. F. Miller, *Mol. Phys.*, 2012, **110**, 1009.

[132] M. P. Meyer, D. R. Tomchick and J. P. Klinman, *Proc. Natl. Acad. Sci. USA*, 2008, **105**, 1146.

[133] Z. D. Nagel, C. W. Meadows, M. Dong, B. J. Bahnson and J. P. Klinman, *Biochemistry*, 2012, **51**, 4147.

[134] S. Habershon, G. S. Fanourgakis and D. E. Manolopoulos, *The Journal of chemical physics*, 2008, **129**, 074501.

[135] M. Ceriotti, M. Parrinello, T. E. Markland and D. E. Manolopoulos, *J. Chem. Phys.*, 2010, **133**, 124104.

[136] M. Shiga and A. Nakayama, *Chem. Phys. Letters*, 2008, **451**, 175 – 181.

[137] T. D. Hone, P. J. Rossky and G. A. Voth, *J. Chem. Phys.*, 2006, **124**, 154103.

[138] D. Marx and J. Hutter, *Ab initio molecular dynamics: Basic theory and advanced methods*, Cambridge University Press, 2009.

[139] A. M. Reilly, S. Habershon, C. A. Morrison and D. W. H. Rankin, *J. Chem. Phys.*, 2010, **132**, 134511.

[140] A. M. Reilly, S. Habershon, C. A. Morrison and D. W. H. Rankin, *J. Chem. Phys.*, 2010, **132**, 094502.

[141] R. Ramírez, C. P. Herrero, A. Antonelli and E. R. Hernández, *J. Chem. Phys.*, 2008, **129**, 064110.

[142] J. Morales and K. Singer, *Mol. Phys.*, 1991, **73**, 873.

[143] R. P. Steele, J. Zwickl, P. Shushkov and J. C. Tully, *J. Chem. Phys.*, 2011, **134**, 074112.

[144] J. R. Schmidt and J. C. Tully, *J. Chem. Phys.*, 2007, **127**, 094103.

[145] S. Habershon, *Phys. Chem. Chem. Phys.*, 2014, **16**, 9154–9160.

[146] T. Spura, C. John, S. Habershon and T. D. Kühne, *Mol. Phys.*, 2015, **113**, 808–822.

[147] O. Marsalek and T. E. Markland, *J. Chem. Phys.*, 2016, **144**, 054112.

[148] C. John, T. Spura, S. Habershon and T. D. Kühne, *Phys. Rev. E*, 2016, **93**, 043305.

[149] K. Vu, J. C. Snyder, L. Li, M. Rupp, B. F. Chen, T. Khelif, K.-R. Müller and K. Burke, *International Journal of Quantum Chemistry*, 2015, **115**, 1115–1128.

[150] T. Hastie, R. Tibshirani and J. Friedman, *The Elements of Statistical Learning: Data Mining, Inference, and Prediction,*, Springer, Address, 2009.

[151] C. E. Rasmussen and C. K. Williams, *Gaussian Processes for Machine Learning*, The MIT Press, Cambridge, Massachusetts, 2006.

[152] G. Krilov and B. J. Berne, *J. Chem. Phys.*, 1999, **111**, 9147–9156.

[153] E. Anderson, Z. Bai, C. Bischof, S. Blackford, J. Demmel, J. Dongarra, J. Du Croz, A. Greenbaum, S. Hammarling, A. McKenney and D. Sorensen, *LAPACK Users' Guide*, Society for Industrial and Applied Mathematics, Philadelphia, PA, 3rd edn., 1999.

[154] A. P. Bartók, M. C. Payne, R. Kondor and G. Csányi, *Phys. Rev. Lett.*, 2010, **104**, 136403.

[155] A. P. Bartók, M. J. Gillan, F. R. Manby and G. Csányi, *Phys. Rev. B*, 2013, **88**, 054104.

[156] M. F. Herman, E. J. Bruskin and B. J. Berne, *J. Chem. Phys.*, 1982, **76**, 5150–5155.

[157] I. F. Silvera and V. V. Goldman, *J. Chem. Phys.*, 1978, **69**, 4209.

[158] K. Thurmer and S. Nie, *Proc. Natl. Acad. Sci. USA*, 2013, **110**, 11757–11762.

[159] Y. P. Handa, D. D. Klug and E. Whalley, *J. Chem. Phys.*, 1986, **84**, 7009–7010.

[160] D. D. K. Y. P. Handa and E. Whalley, *Can. J. Chem.*, 1988, **66**, 919 – 924.

[161] J. D. Bernal and R. H. Fowler, *J. Chem. Phys.*, 1933, **1**, 515.

[162] T. L. Malkin, B. J. Murray, A. V. Brukhno, J. Anwar and C. G. Salzmann, *Proc. Natl. Acad. Sci. USA*, 2012, **109**, 1041–1045.

[163] D. Quigley, *J. Chem. Phys.*, 2014, **141**, 121101.

[164] L. Lupi, A. Hudait, B. Peters, M. Grünwald, R. G. Mullen, A. H. Nguyen and V. Molinero, *Nature*, 2017, **551**, 218.

[165] J. L. F. Abascal and C. Vega, *J. Chem. Phys.*, 2005, **123**, 234505.

[166] J. L. F. Abascal, E. Sanz, R. G. Fernandez and C. Vega, *J. Chem. Phys.*, 2005, **122**, 234511.

[167] Z. Raza, D. Alfe, C. G. Salzmann, J. Klimes, A. Michaelides and B. Slater, *Phys. Chem. Chem. Phys.*, 2011, **13**, 19788–19795.

[168] B. Pamuk, P. B. Allen and M.-V. Fernández-Serra, *Phys. Rev. B*, 2015, **92**, 134105.

[169] A. Hudait, S. Qiu, L. Lupi and V. Molinero, *Phys. Chem. Chem. Phys.*, 2016, **18**, 9544–9553.

[170] T. Hondoh, T. Itoh, S. Amakai, K. Goto and A. Higashi, *J. Phys. Chem.*, 1983, **87**, 4040–4044.

[171] G. T. Gao, X. C. Zeng and H. Tanaka, *J. Chem. Phys.*, 2000, **112**, 8534.

[172] J. M. Polson and D. Frenkel, *J. Chem. Phys.*, 1999, **111**, 1501.

[173] J. K. Johnson, J. A. Zollweg and K. E. Gubbins, *Mol. Phys.*, 1993, **78**, 591.

[174] T. D. Kühne, M. Krack and M. Parrinello, *J. Chem. Theory Comput.*, 2009, **5**, 235–241.

[175] J. C. Howard, J. D. Enyard and G. S. Tschumper, *J. Chem. Phys.*, 2015, **143**, 214103.

[176] B. Monserrat, N. D. Drummond and R. J. Needs, *Phys. Rev. B*, 2013, **87**, 144302.

[177] J. L. Aragones, J. L. F. Abascal, E. G. Noya and C. Vega, *J. Chem. Phys.*, 2007, **127**, 154518.

[178] P. Ball, *Nature*, 2003, **423**, 25–26.

[179] P. Ball, *Chemical reviews*, 2008, **108**, 74–108.

[180] D. Chandler, *Nature*, 2005, **437**, 640–647.

[181] Y. Nagata, R. E. Pool, E. H. Backus and M. Bonn, *Physical review letters*, 2012, **109**, 226101.

[182] A. E. Ismail, G. S. Grest and M. J. Stevens, *The Journal of chemical physics*, 2006, **125**, 014702.

[183] E. Romero-Montalvo, J. M. Guevara-Vela, W. E. Vallejo Narváez, A. Costales, n. M. Pendás, M. Hernández-Rodríguez and T. Rocha-Rinza, *Chem. Commun.*, 2017, **53**, 3516–3519.

[184] V. Vaida, *The Journal of Chemical Physics*, 2011, **135**, 020901.

[185] A. P. Willard and D. Chandler, *The Journal of Physical Chemistry B*, 2010, **114**, 1954–1958.

"Be that word our sign of parting, bird or fiend!" I shrieked, upstarting,
"Get thee back into the tempest and the Night's Plutonian shore!
Leave no black plume as a token of that lie thy soul hath spoken!
Leave my loneliness unbroken! Quit the bust above my door!
Take thy beak from out my heart, and take thy form from off my door!"
Quoth the raven, "Nevermore."

And the raven, never flitting, still is sitting, still is sitting
On the pallid bust of Pallas just above my chamber door;
And his eyes have all the seeming of a demon that is dreaming,
And the lamp-light o'er him streaming throws his shadow on the floor;
And my soul from out that shadow that lies floating on the floor
Shall be lifted, nevermore!

-Edgar Allen Poe
